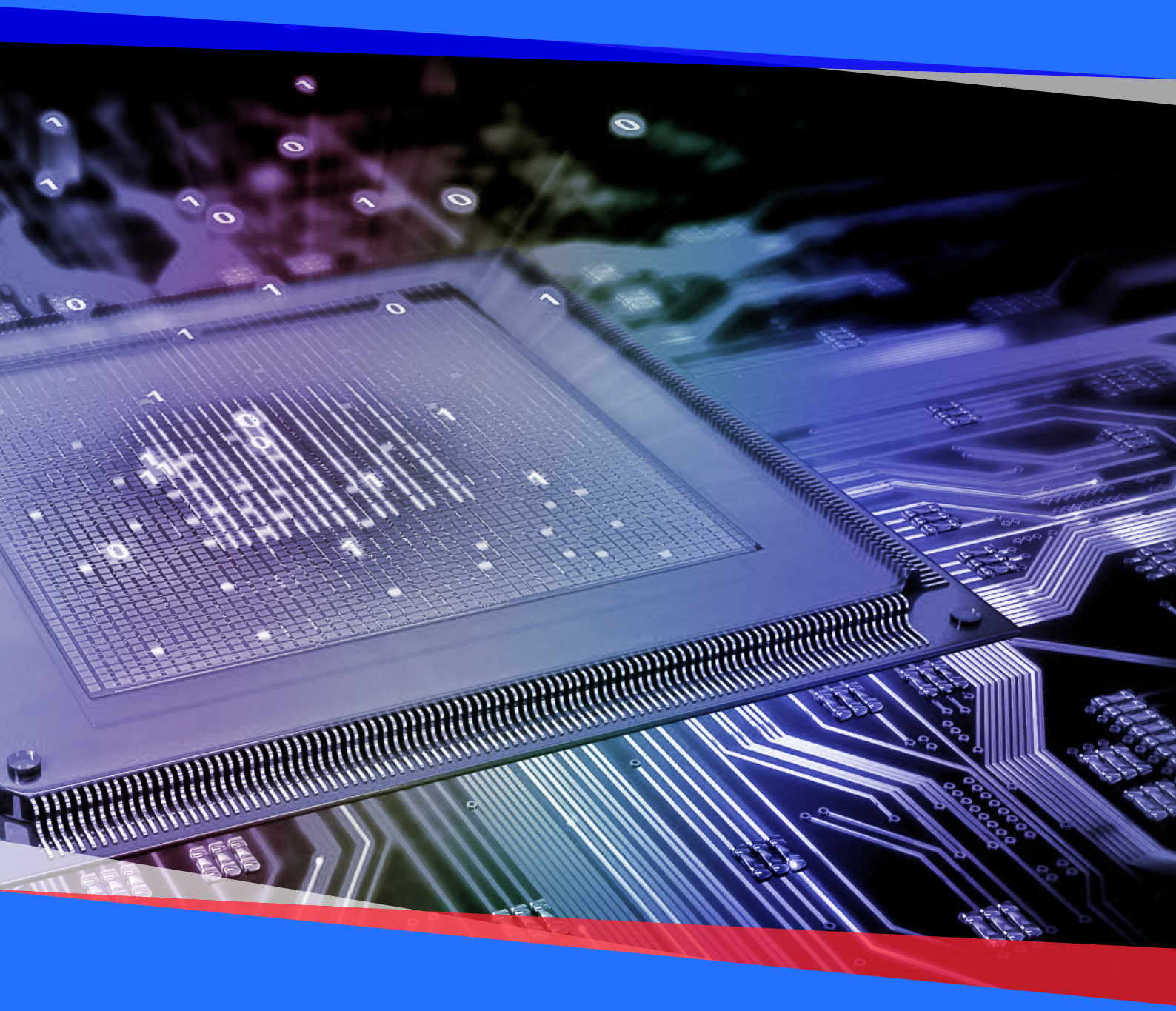

“Instrumentation Engineering, Electronics and Telecommunications – 2016”

Proceedings of the International Forum

November 23–25, 2016
Izhevsk, Russia

Министерство образования и науки Российской Федерации
Федеральное государственное бюджетное образовательное
учреждение высшего образования
«Ижевский государственный технический университет имени М. Т. Калашникова»

«ПРИБОРОСТРОЕНИЕ, ЭЛЕКТРОНИКА И ТЕЛЕКОММУНИКАЦИИ – 2016»

Сборник статей Международного форума

(Ижевск, Россия, 23–25 ноября 2016 г.)

Издательство ИжГТУ
имени М. Т. Калашникова
Ижевск
2017

УДК 681.2(06)

«Приборостроение, электроника и телекоммуникации – 2016» [Электронный ресурс] : сб. ст. Междунар. форума (Ижевск, Россия, 23–25 ноября 2016 г.). – Ижевск : Изд-во ИжГТУ имени М. Т. Калашникова, 2017. – 119 с. – 16,1 МБ.

ISBN 978-5-7526-0790-5 (Электронное издание)

Сборник содержит прошедшие рецензирование статьи на английском языке по широкому кругу вопросов в областях приборостроения, электроники, связи и смежных им, которые обсуждались на II Международном форуме «Instrumentation Engineering, Electronics and Telecommunications – 2016» («Приборостроение, электроника и телекоммуникации – 2016»), проводимом в рамках XII Международной научно-технической конференции «Приборостроение в XXI веке. Интеграция науки, образования и производства» (23–25 ноября 2016 года, Ижевск, Россия).

Материалы статей могут быть полезны ученым, специалистам, молодым исследователям, аспирантам и студентам.

УДК 681.2(06)

ISBN 978-5-7526-0790-5
(Электронное издание)

The Ministry of Education and Science of the Russian Federation
Kalashnikov Izhevsk State Technical University

“INSTRUMENTATION ENGINEERING, ELECTRONICS AND TELECOMMUNICATIONS – 2016”

Proceedings of the International forum

(Izhevsk, Russia, November 23–25, 2016)

Publishing House
of Kalashnikov ISTU
Izhevsk
2017

UDC 681.2(06)

"Instrumentation Engineering, Electronics and Telecommunications – 2016" : Proceedings of the International Forum (November 23–25, 2016, Izhevsk, Russia). – Izhevsk : Publishing House of Kalashnikov ISTU, 2017. – 119 p. – 16.1 MB.

ISBN 978-5-7526-0790-5 (Electronic Edition)

This volume contains peer-reviewed papers on wide range of problems in fields of instrumental engineering, electronics, telecommunications and related areas discussed during the II International Forum "Instrumentation Engineering, Electronics and Telecommunications – 2016" held within the framework of the XII International Scientific-Technical Conference "Instrumentation Engineering in the XXI Century. Integration of Science, Education and Production" (November 23–25, 2016, Izhevsk, Russia).

Proceedings could be useful for scientists, professionals, young researchers, students.

UDC 681.2(06)

ISBN 978-5-7526-0790-5
(Electronic Edition)

TABLE OF CONTENTS

Research of Acoustic Wave Generated by Heterogeneous Interface

K. E. Abbakumov, B. Ch. Ee

Saint Petersburg Electrotechnical University "LETI", Saint-Petersburg, Russia
E-mail: ee.boris.eut@gmail.com

Received: 28.11.2016

Abstract. We have examined cooperation of plane acoustic wave with cylindrical triggering at interface part where we see a flexible bonding with background medium. To make the flexible bonding at the interface we used stiffness module introduced into boundary conditions. We used scattering cross section to characterize a scattered field. So, we have found that there can be different resonance phenomena in accordance with the size of broken part.

Keywords: plane wave, contact stiffness module, graphite, metal, scattering cross section, finite element method

INTRODUCTION

Cylindrical defect model is popular while research works as to cooperation of real round and extensive defects with ultrasonic wave. This model considers absolutely rigid contact between triggering and background medium. But due to many polished section studies we see that triggering and background medium interface can include sections with partial adhesion fault or full adhesive bonding fault. Cooperating with the similar interface the ultrasonic wave makes a complex diffraction field in bonding with interruptions while transmission of displacement normal component and with sliding of adjoining surfaces while transmission of displacement tangential component [1]. In [2] we show the ability to take into account such interface with the help of interface conditions at linear yawing approach, if there are interruptions while transmission of displacement components and uninterrupted transmission of stress tensor component via stiffness tensor.

MODELING IN COMSOL

Imagine, a plane ultrasonic wave is incident on elastic cylindrical inclusion of a radius, where in the sector of φ dimensions there is adhesive bonding fault, with acoustic parameters ρ_1, c_{l1}, c_{t1} – density, compressional and shear velocity, located at solid isotropic matrix with the following parameters ρ_2, c_{l2}, c_{t2} (Fig. 1).

Let's examine a normal acoustic wave incident which is parallel to Y axis. As the wave is parallel to Y axis so there are not polarized waves in another plane. Cylindrical inclusion (do-

main 1) with diameter d interact with incident wave and generate scattered and transmitted waves. There is damaged adhesion in the sector (orange line) in the interface between domain 1 and domain 2, which is described as thin elastic layer with normal and tangent contact stiffness (KGN and KGT respectively). It's necessary to study the how contact stiffness affect on the scattered field. This task is solved with the finite element method implemented in the COMSOL software application. Geometrical properties of domain zones are shown in Table 1.

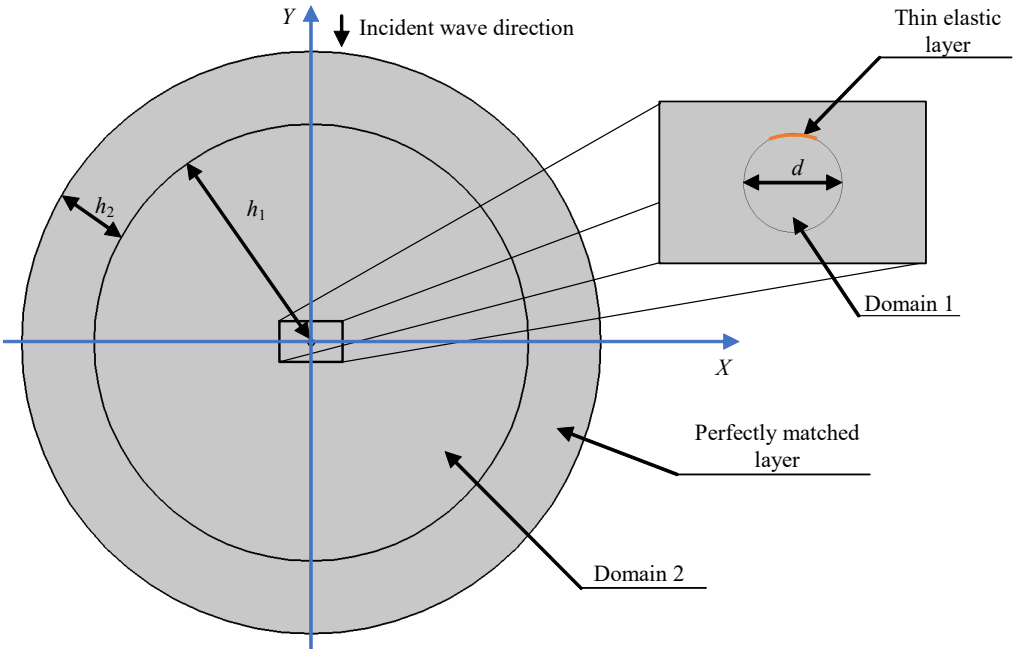

Figure 1. Cylindrical defect in semi-infinite cylindrical matrix

Table 1. Geometrical properties of domain zones

Domain	Size of domain, mm
Domain 1	$d = 1$
Domain 2	$h_1 = 6\lambda$
Perfectly matched layer	$h_2 = 2\lambda$

where $\lambda = 2\pi f / c_l$, π – mathematical constant, f – frequency.

The equation describing elastic wave propagation is shown with the wave equation:

$$\Delta u = \frac{1}{c^2}\frac{d^2}{dt^2}, \tag{1}$$

where Δ – Laplace operator; u – displacement; c^2 – phase velocity.

If propagation is harmonic, the equation (1) is changed into the Helmholtz equation:

$$\Delta u + k^2 u = 0,$$

where k – wave number.

If two solids are bonding following boundary conditions are to be taken place in the cylindrical coordinates:

– uninterrupted displacement components:

$$u_r^I = u_r^{II}, \tag{2}$$

$$u_\theta^I = u_\theta^{II}, \tag{3}$$

where u_θ^I, u_r^I, u_θ^{II}, u_r^{II} – components of displacement, upper index denotes domain 1 or 2, lower index denotes component of displacement in cylindrical coordinate;

– uninterrupted stress component:

$$\sigma_{rr}^I = \sigma_{rr}^{II}, \tag{4}$$

$$\sigma_{r\theta}^I = \sigma_{r\theta}^{II}, \tag{5}$$

where σ_{rr}^I, σ_{rr}^{II} – normal component of mechanical stress, upper index denotes domain 1 or 2, lower index denotes component of mechanical stress in cylindrical coordinate; $\sigma_{r\theta}^I$, $\sigma_{r\theta}^{II}$ – tangential component of mechanical stress.

As boundary conditions (2)–(5) in the sector of cylindrical triggering and background medium are changed into [2]:

$$\left.\begin{aligned} u_r^I + \frac{\sigma_{rr}^I}{KGN} &= u_r^{II} \\ u_\theta^I + \frac{\sigma_{r\theta}^I}{KGT} &= u_\theta^{II} \\ \sigma_{rr}^I &= \sigma_{rr}^{II} \\ \sigma_{r\theta}^I &= \sigma_{r\theta}^{II} \end{aligned}\right\}, \tag{6}$$

where *KGN*, *KGT* – normal and tangential components of contact stiffness.

Range of values of *KGN*, *KGT* at 10^{12}–10^{17} N/m^3 conforms with the path from free boundary condition to rigid contact [3]. In [4] it is shown the opportunity to make such flexible contact with thin elastic layer with certain values of components of stiffness.

Besides the wave equation and interface conditions we have to model semi-infinite medium. In COMSOL we show semi-infinite medium as a perfectly matched layer embanking the examined area. The perfectly matched layer takes up all the waves entering it and with large losses there is no reflection from the boundaries [5].

To numerical simulation let's choose a steel as a material for domain 2 and perfectly matched layer and a graphite for domain 1 with the following properties as shown in the Table 2 [6, 7].

Table 2. Elastic properties of a chosen materials

Material	**Young's modulus *E*, GPa**	**Shear modulus *G*, GPa**	**Density, ρ, kg/m^3**
steel	5920	3100	7800
graphite	25.5	97	2250

Scattering cross section *SCS* (7) is chosen as a property to be examined. *SCS* is a ratio of the energy flux in the scattered wave to the intensity in the incident wave through the propagation cross line [8]:

$$SCS = \frac{F_s}{I_{inc}}, \tag{7}$$

where $F = -\int \sigma_{ij} \frac{\partial u}{\partial t} n_i dS$; I_{inc} – incident wave intensity; n_i – normal to area S. Additionally, angular distribution of normalized amplitude of displacement in far field is investigated. Displacement amplitude normalized to maximum displacement amplitude at $KN = 10^{12}$ N/m^3.

RESULTS

In the Fig. 2–4 we show scattering cross section *SCS* versus defect wave size $k_l a$ relationship.

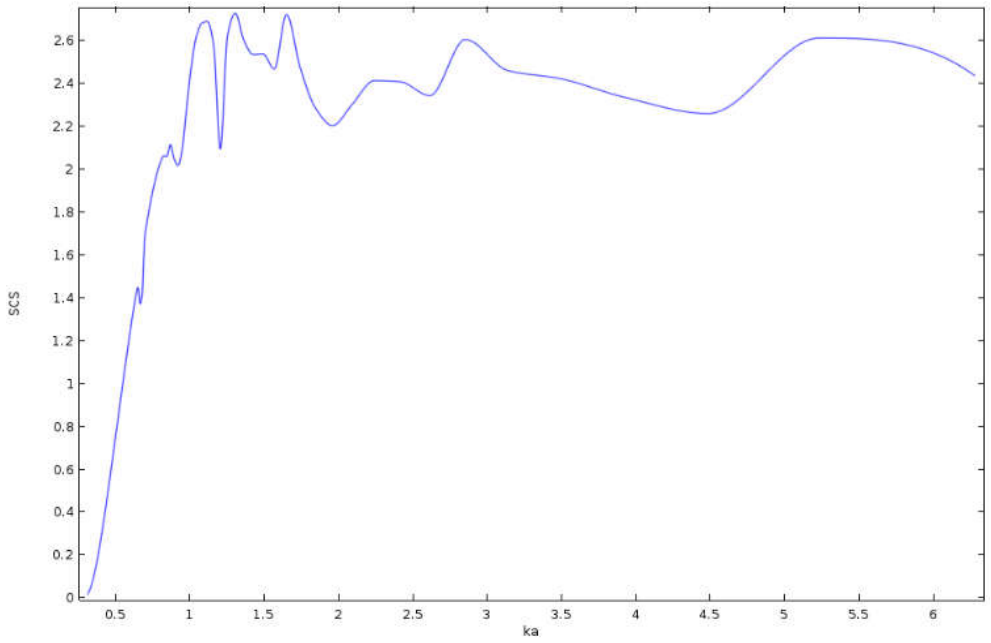

Figure 2. Scattering cross section *SCS* versus defect wave size $k_l a$ relationship if $KN = 10^{15}$ N/m^3

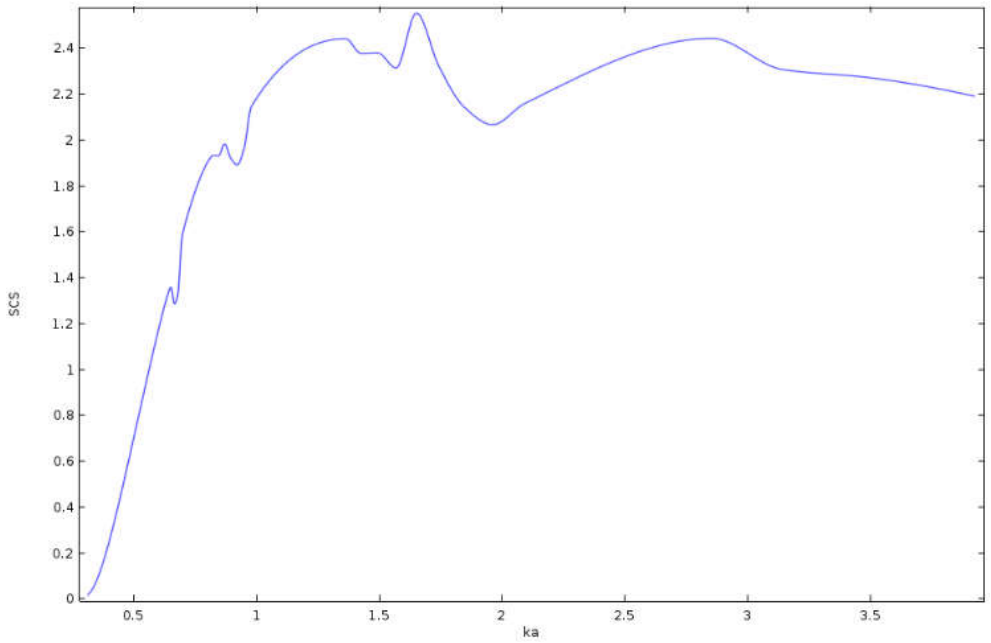

Figure 3. Scattering cross section *SCS* versus defect wave size $k_l a$ relationship if $KN = 10^{13}$ N/m^3

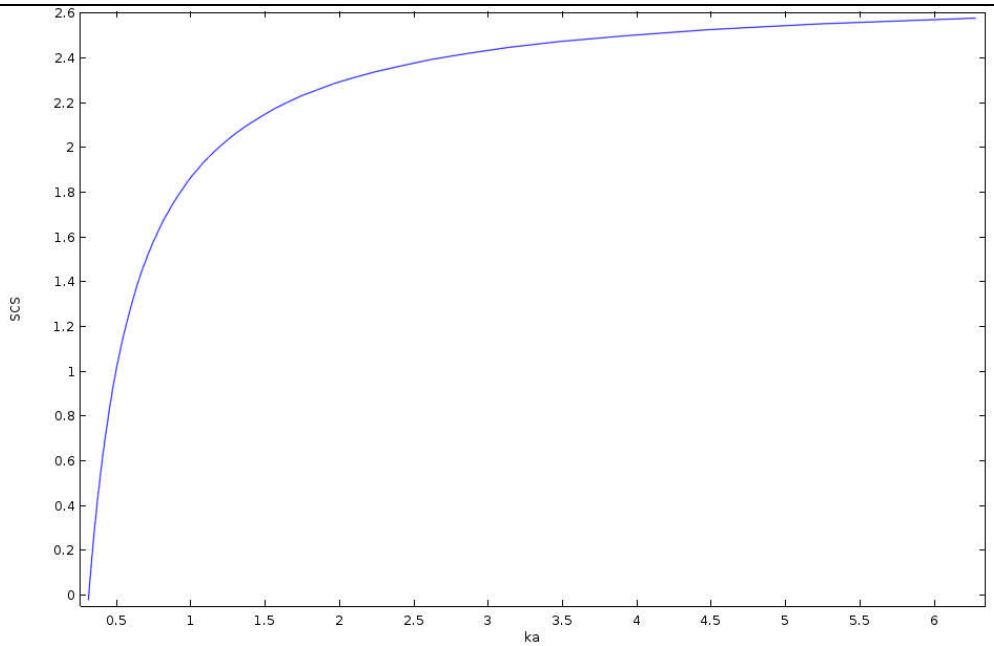

Figure 4. Scattering cross section *SCS* versus defect wave size $k_l a$ relationship if $KN = 10^{12}$ N/m^3

The results of show us that contact rigidity module change causes the change of scattered resulting in resonance phenomena appearance. We see that the change of $KGN = KGT = KN$ in the range from $KN = 10^{12}$ N/m^3 to $KN = 10^{17}$ N/m^3 conforms with the path from a cavity to welded contact. If $KN = 10^{12}$ N/m^3, scattering cross section (Fig. 4) is equal with the results for the cavity in [9].

In Fig. 5–8 the angular distribution of mechanical displacement is shown.

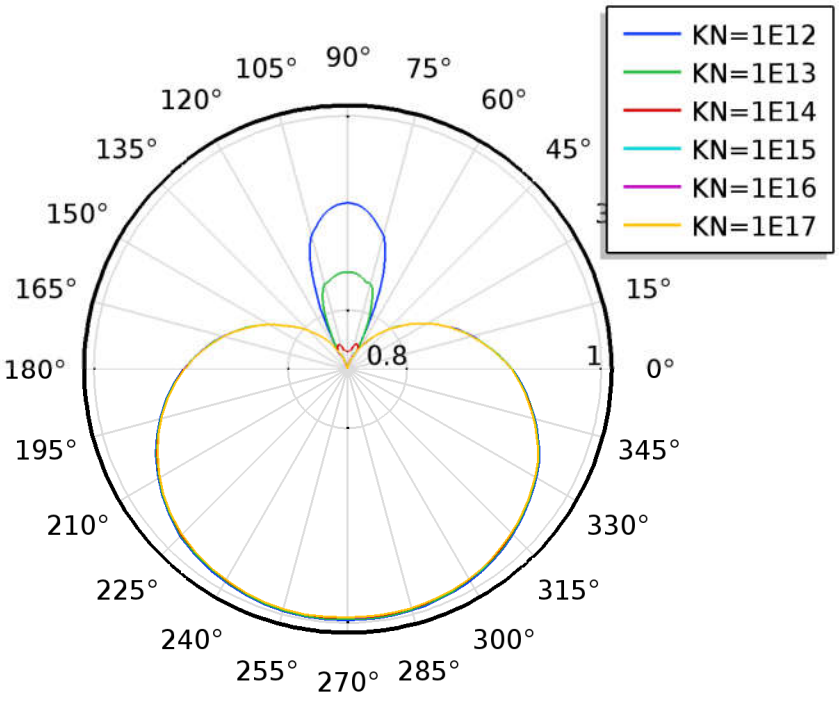

Figure 5. Angular distribution of mechanical displacement on frequency $f = 2.6 \cdot 10^5$ Hz and various values of *KN*

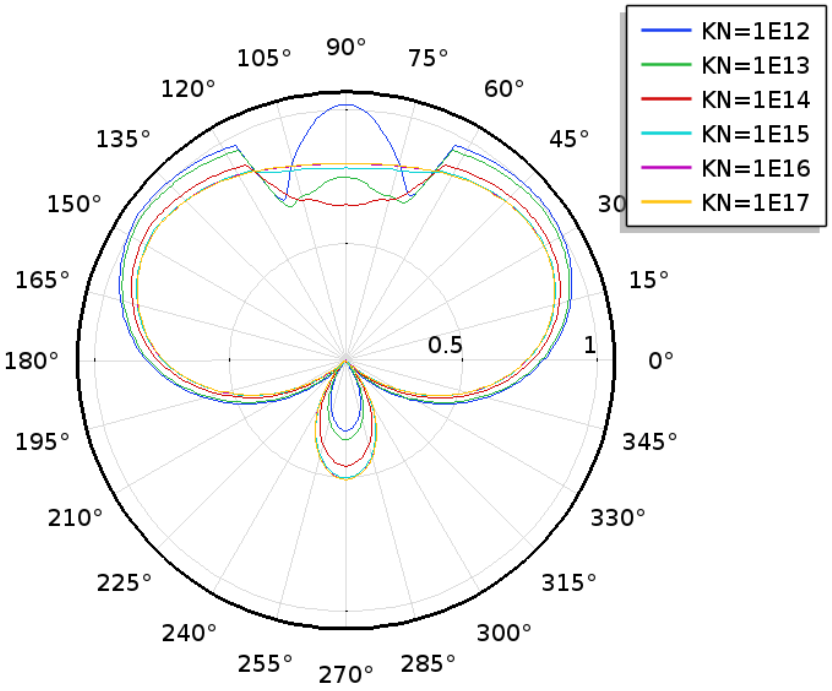

Figure 6. Angular distribution of mechanical displacement on frequency $f = 1 \cdot 10^6$ Hz and various values of KN

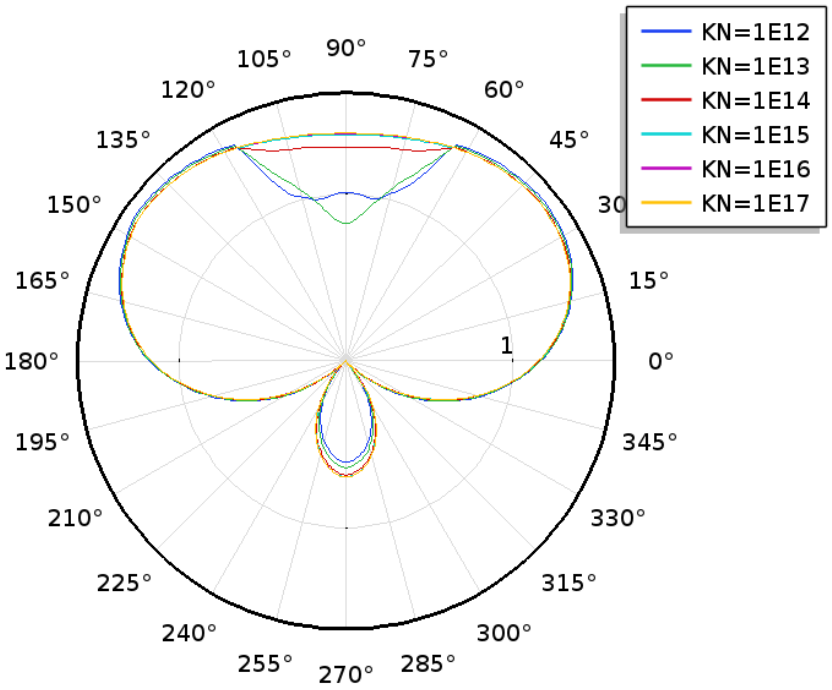

Figure 7. Angular distribution of mechanical displacement on frequency $f = 1.114 \cdot 10^6$ Hz and various values of KN

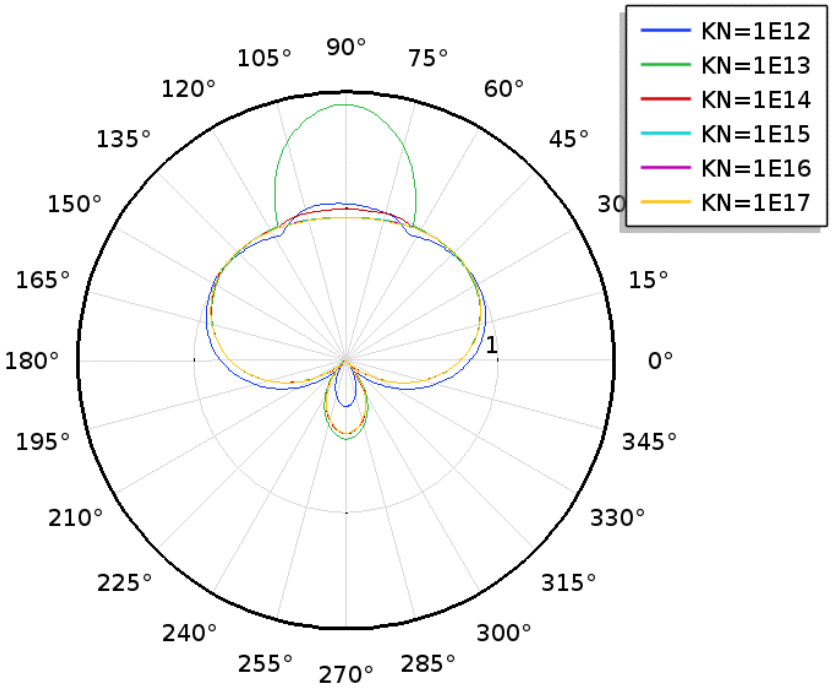

Figure 8. Angular distribution of mechanical displacement on frequency $f = 1.215 \cdot 10^6$ Hz and various values of KN

In Fig. 5–8 we can see that damaged adhesion has different affect on scattered field. For example, in Fig. 5 on the frequency $f = 2.6 \cdot 10^5$ Hz with $KN = 10^{14}$–10^{17} N/m^3 slightly decrease amplitude of displacement in sector, also we can see that the most part of the resulting field is transmitted waves. In Fig. 6 on the frequency $f = 1 \cdot 10^6$ Hz with $KN = 10^{12}$ N/m^3 at the ends of damaged adhesion sector, the amplitude decreases, this may be due to interference on a thin elastic layer. In Fig. 7 on the frequency $f = 1.114 \cdot 10^6$ Hz with $KN = 10^{12}$–10^{14} N/m^3 the displacement amplitude is increase. In Fig. 8 on the frequency $f = 1.215 \cdot 10^6$ Hz with $KN = 10^{13}$ N/m^3 the displacement amplitude is slightly increase, it can be related with resonant scattering or thin elastic layer can be as a quarter-wave matching layer.

Conclusion

Scattering properties of cylindrical heterogeneity are related to the contact quality between the heterogeneity and background medium very much. So damaged adhesion has a large effect on information signals against heterogeneities. It should be taken into account at nondestructive testing, since it can cause both the undetection of the defect or a valid defect can be taken as invalid.

References

1. Schoenberg, M. (1980). Elastic wave behavior across linear slip interfaces. *The Journal of the Acoustical Society of America, 68*(5), 1516–1521. doi:10.1121/1.385077
2. Rokhlin, S. I. (1991). Analysis of boundary conditions for elastic wave interaction with an interface between two solids. *The Journal of the Acoustical Society of America, 89*(2), 503–515. doi:10.1121/1.400374

3. Nihei, K. T., Myer, L. R., & Cook, N. G. W. (1995). Numerical simulation of elastic wave propagation in granular rock with the boundary integral equation method. *The Journal of the Acoustical Society of America, 97*(3), 1423–1434. doi:10.1121/1.412084
4. Huang, W. (1997). Analysis of different boundary condition models for study of wave scattering from fiber–matrix interphases. *The Journal of the Acoustical Society of America*, *101*(4), 2031–2042. doi:10.1121/1.418135
5. COMSOL (2016). COMSOL Multiphysics Reference Manual. Stockholm: COMSOL AB.
6. Cost, J. R., Janowski, K. R., & Rossi, R. C. (1968). Elastic properties of isotropic graphite. *The Philosophical Magazine: A Journal of Theoretical Experimental and Applied Physics, 17*(148), 851–854. doi:10.1080/14786436808223035
7. Cambridge University Engineering Department (2003). *Materials data book.* Retrieved from http://www-mdp.eng.cam.ac.uk/web/library/enginfo/cueddatabooks/materials.pdf
8. Hinders, M. K. (1993). Elastic-wave scattering from an elastic cylinder. *Il Nuovo Cimento B, 108*(3), 285–301. doi:10.1007/BF02887489
9. Liu, Y., Wu, R. S., & Ying, C. F. (2000). Scattering of elastic waves by an elastic or viscoelastic cylinder. *Geophysical Journal International, 142*(2), 439–460. doi:10.1046/j.1365-246X.2000.00173.x

Modeling of Piezoelectric Transducers for Energy Harvesting

R. Emilova, N. Goncharova, B. Ee, R. Konovalov, O. Spirina, V. Tsaplev

Department of Electroacoustics and Ultrasound Techniques
Saint-Petersburg Electrotechnical University "LETI"
E-mails: emilova.roxi@gmail.com
gonchrova9450@gmail.com
ee.boris.eut@gmail.com
rskonovalov.eut@gmail.com
olga.spirina11@gmail.com
valery@convergences-fr.ru

Received: 15.11.2016

Abstract. The paper concerns three different types of piezoelectric transducers for creating energy harvesting devices for small-size radioelectronic devices. Modes of operation of the proposed circuits of piezoelectric transducers are analyzed numerically in the mathematical FEM software package COMSOL 5.1. For a piezoelectric generator of the umbrella type, both numerical and experimental simulations are performed. The load regimes of piezoelements are determined both in the frequency and spatial domains, as well as the frequency dependences of the output voltage for transducers like disk bimorph umbrella-, aeroelastic- and the static-types. It is shown that the matching of the piezoelectric transducer with the load can be coordinated by connecting the piezoelectric elements in parallel to reduce the input resistance of the energy harvesting. The simulation results show the possibility of obtaining rather high voltages at different frequencies, and different designs make possible to use the piezoelectric energy harvesters in various conditions as independent energy sources.

Keywords: energy harvesting, piezoeffect, piezoelectric transducer, mathematical modeling, mechanical stress, strain, output voltage

INTRODUCTION

The design and study of compact piezoelectric energy harvesters now became a very contemporary and important problem, attracting the attention of many scientists and engineers. The interest in this problem is due to the possibility of the prospect of creating different small independent and virtually inexhaustible sources of power for the various autonomous electronic devices. Such sources convert the bargain energy of vibrations that present almost everywhere to the electrical energy and do not require external power sources or do not demand costs for periodic replacement of batteries and their chemical processing [1].

The analysis of numerous works on obtaining electrical energy from vibration for power microelectronic devices shows a significant advantage of piezoelectric method in comparison with the electromagnetic or electrostatic one [2].

The main advantage of the piezoelectric method of energy conversion is large, compared to other methods of conversion, electric power density, and simplicity of design. The range of values of the resulting voltages is much wider than that of all other types of harvesters.

The main disadvantage of piezoelectric method of energy harvesting can be attributed to the large output impedance of the source. However, this disadvantage can be easily compensated by proper choice of the number of piezoelements, or by the proper choice of their connection – parallel or serial. Moreover, this disadvantage can be turned into the advantage. By the proper selection of the number of elements and their connection one can obtain practically any desired output voltage and internal resistance.

Various types of piezoelectric harvesters can be realized using both longitudinal and transverse vibrations, but in most cases they are performed in the form of cantilever beams with piezoelectric elements, one end of which is clamped in the support, and the other is free. To reduce the working frequency range of the piezoelectric bimorph (three-morph) beams a passive load is placed at its free end,

One can conclude, that the piezoelectric method of producing electrical energy is characterized by a high flexibility of choosing its design.

The piezoelectric energy harvester can be placed at any vibrating place, for example fit snugly to the base, or to the element of the building structure or to a floor or to the road surface or to any vibrating surface. As a result of external impact to the piezoelectric element an electric voltage arises at its output, which after rectification can be supplied to the circuit that controls battery charge. Then the energy of the charged battery may be used by the consumer, i.e., used the waste energy of the external impact or vibration of different objects.

All vibrations are of different nature. Accordingly, it is necessary to create a device that can be used effectively under various conditions. In this regard, three types of piezoelectric transducers have been developed: disc – bimorph umbrella-type, aeroelastic and static transducer.

DISK BIMORPH UMBRELLA – TYPE PIEZOELECTRIC TRANSDUCER

Disk bimorph piezoelectric transducer is a cantilevered bimorph piezoelectric transducer, which is vibrating under the influence of external vibrations. Accordingly, alternative electric voltage arises across causing its electrodes due to the direct piezoelectric effect.

It should be noted that "pure bimorph" structure, which is suitable for the construction of the transducer, is not well suited concerning the problem of energy.

Theoretical and experimental analysis shows [3–5], that best design of the piezoelectric harvester must preferably be the "threemorph", rather than "bimorph". That means, that the transducer must contain two piezoceramic plate with an inverted polarization, pasted on the intermediate base metal plate, so that the piezoelectric ceramics must be located in the area of considerable mechanical alternating stresses. However, this increases the thickness of the flexural bimorph piezoelectric element, which in this case goes out of the desired range of vibration frequencies due to the increase of the frequency of its own umbrella resonance. That is why, a rather massive metal ring is glued on the periphery of the round substrate to reduce the frequency of its main resonance.

The piezoelectric transducer (Fig. 1) consists of the round cantilevered plate 1, 110 mm in diameter; the annular mass 3 around the circumference of the plate; and piezoelectric elements 4 on both surfaces of the plate. Each element is made in the form of a thin plate 25 mm in diameter.

To perform a numerical simulation using FEM software COMSOL 5.1 three-dimensional model of bimorph disk piezoelectric transducer of a selected size was created with the necessary parameters and boundary conditions.

The plate oscillates under the action of the externally applied alternated exciting force. The modeling showed, that the offset edges of the plate oscillated harmonically with the amplitude up to 2 mm (Fig. 2).

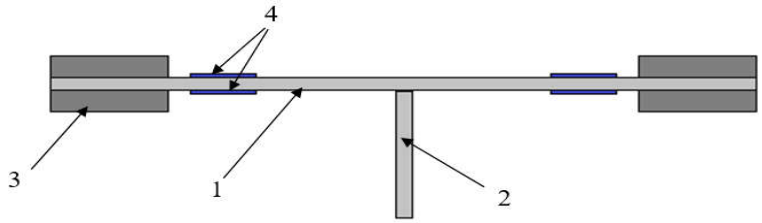

Figure 1. Disk bimorph umbrella piezotransducer:
1 – bronze plate, 2 – leg, 3 – annular mass, 4 – round plate piezoelectric elements

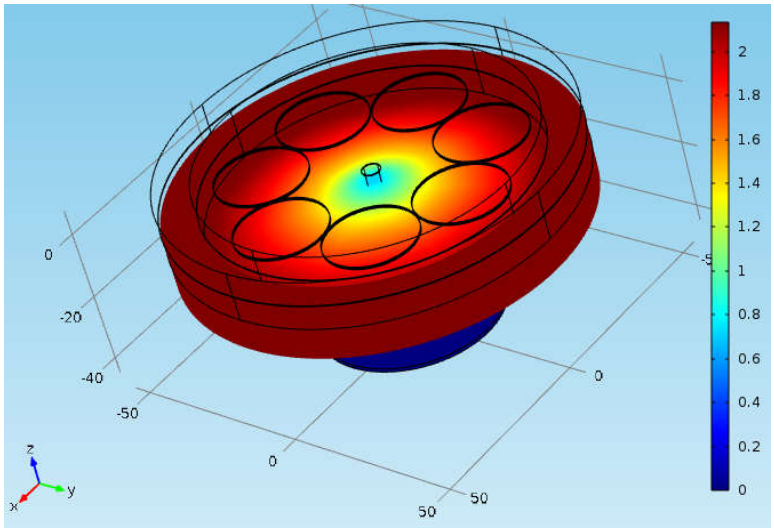

Figure 2. The offset edges of the plate under the action of the external exciting force

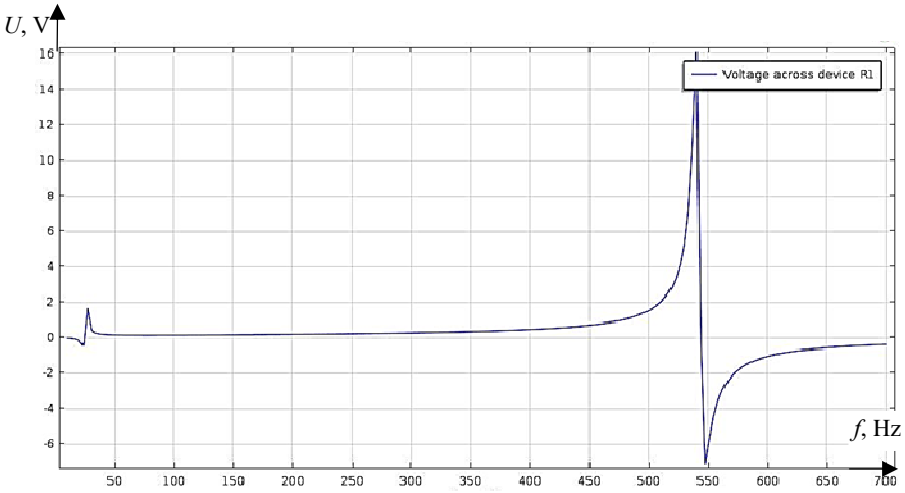

Figure 3. The frequency dependence of the output voltage of the Disk bimorph umbrella piezotransducer

One can see from the curve in Fig. 3, that the output voltage reaches 2 V in the idle mode at the frequency of 46 Hz, and reaches the value of 16 V at the main resonance frequency about 548 Hz. Since the values of the output voltage are complex, the curve is keen.

Modeling of the transducer showed good results. The transducer generated the output electrical voltage up to 16 V in the idle mode. One can obtain better results, if change the settings, sizes, locations of piezoelectric transducers and transducer materials. At this stage of study with the selected parameters the results are optimal.

The usage of this type of bimorph disk transducers for energy harvesting helps to reduce the power consumption by the portable systems of obtaining initial information (electronic devices, sensors, monitoring the state of the environment, etc.) and to provide their autonomous operation for a practically unlimited time due to the energy obtained from vibrations of the environment.

AEROELASTIC PIEZOELECTRIC TRANSDUCER

The turbulent flows that occur in the liquid media or the air around moving bodies, causes flexural deformation of these bodies and flutter. In this context the following aeroelastic model of the piezoelectric transducer was developed [6]. The model provides a rigid wing fastened with a steel rod. On both sides of the end parts of the wing two piezoelectric layers are placed symmetrically from the base of the wing [7]. The wing itself is placed into the air flow, as shown in Figure 4.

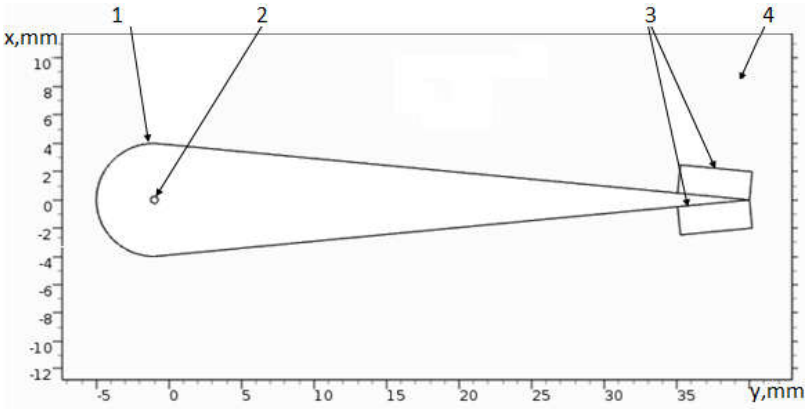

Figure 4. Aeroelastic piezoelectric transducer:
1 – rigid wing, 2 – steel rod, 3 – piezoelectric layers, 4 – environment (liquid or air)

The work of this type of the piezoelectric transducer at different operation modes was simulated by the frequency element method using COMSOL 5.1. The frequency dependence of electric output from the level of mechanical stress is shown in Fig. 5.

The maximum output voltage reaches up to 0.85 at the frequency about 115 Hz. Such changes in the low frequencies range (below 200 Hz) are due to the natural frequencies of the structure model. One can also notice a certain periodical repetitions of the arrival of resonances at frequencies about 300 Hz, 550 Hz, with smaller amplitudes.

Thus, in this paper we analyzed the modes of efficient usage of the energy transducer for the piezoelectric harvester operating in an aerodynamic flow. In the process of mathematical modeling of such piezoelectric harvester with beam-type transducers (the transducers have the form of beams or thick plates) the frequency dependences of the transducer output voltage were determined.

Also the possibility of its usage as a source of electric power when placed in a wind stream, such as air or water. Such an approach is feasible, if put it on the wing of the aircraft, as shown by the simulation results, the generated voltage was more than 0.4 V at the flow velocities over 10 m/s.

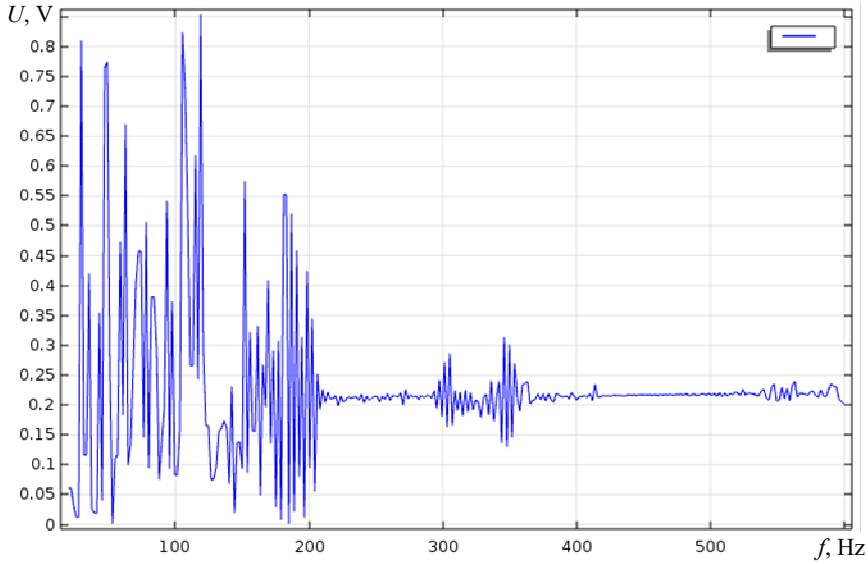

Figure 5. Frequency dependence of generated output voltage of the aeroelastic piezoelectric harvester

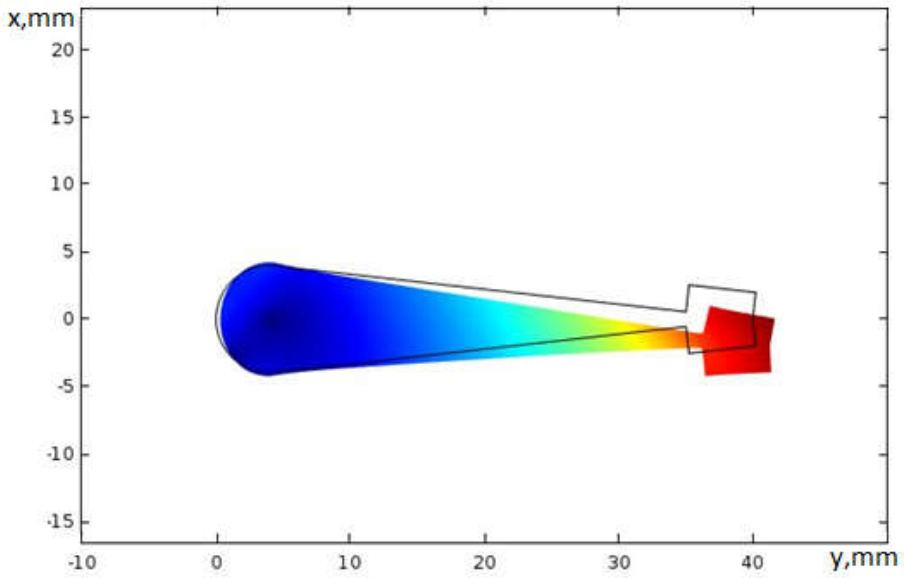

Figure 6. Deformation of the wing (enlarged scale)

Fig. 6 shows an example of deformation of the wing. For the purpose of clarity, the drawing is executed in an enlarged scale.

THE STATIC – TYPE PIEZOELECTRIC TRANSDUCER

The general arrangement of the static-type piezoelectric transducer for energy harvester is shown in Fig.7). In this figure: 1 – steel plate of 600 mm long, the left end being fixed console – 4. The plate acts as a lever, the load being applied through the hemispherical element 2.

Six piezoelectric PZT elements are assembled in a column – 3. The piezoelement dimensions are: thickness – 2 mm, diameter 30 mm). The piezoelements are connected to better align with the input impedance electrical circuit in parallel. The whole structure is supported on a fixed plate 5.

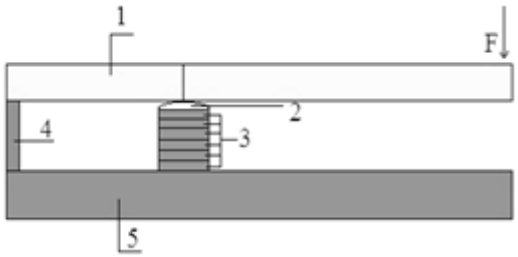

Figure 7. The model of the static-type transducer

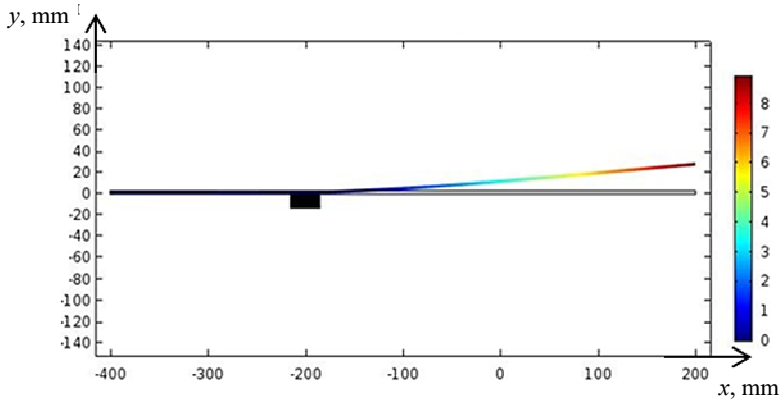

Figure 8. Displacement of the plate

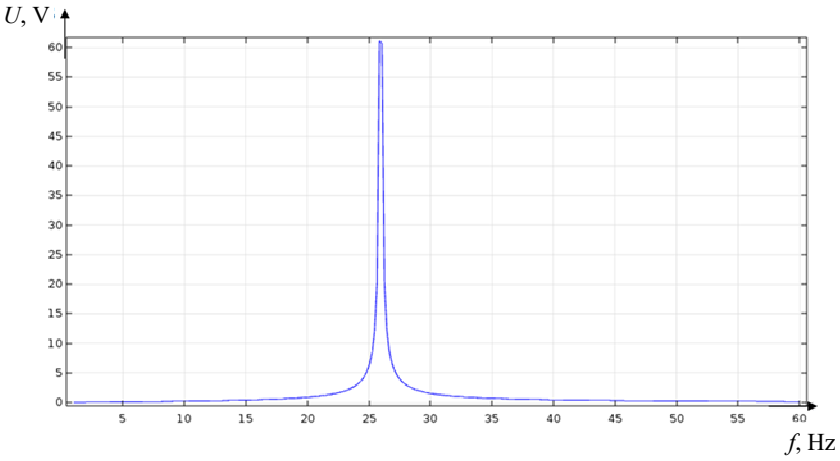

Figure 9. Output voltage frequency response

This type of static generator can be used in different applications. The piezoelectric energy harvesters can be placed at the bottom of some structure that can fit snugly, for example, to the element of the building structure or to a floor or road surface, or to the vibrating surface. One can use it as a power source for lights on the highways, as a low power source for small independent devices, etc.

Numerical modeling [8] has shown that under mechanical load equivalent to the mass of 100 kg, the maximum displacement of the plate was about 9 mm (Fig. 8). The output voltage frequency response is shown in Fig. 9. One can see, that the maximum value of the output voltage may be as much as 60 V.

CONCLUSIONS

Different types of piezoelectric energy sources were analyzed in this paper. The piezoelectric energy harvesters based in these types of piezoelectric transducers are suitable for a great number of electronic devices, sensors, various small appliances as storage elements (batteries). Such devices do not require powerful energy sources, so the piezoelectric transducers are promising.

The simulation results show the possibility of obtaining rather high voltages at different frequencies, and different designs make possible to use the piezoelectric energy harvesters in various conditions as independent energy sources.

Detailed analysis of all possible applications of different types of piezoelectric energy harvesters is far beyond the scope of this work.

The further research will be focused on the study of the influence of the nonlinearity of the piezoelectric ceramic transducers to the properties of piezoelectric energy harvesters.

It should be noted that these types of transducers are based on the usage of commercially available piezoelectric ceramics. They do not require any additional treatment, and they are relatively cheap for production.

ACKNOWLEDGEMENTS

This work has been accomplished as a part of the Ministry of Education and Science of the Russian Federation research assignment "Realization of scientific research (fundamental studies, applied research and advanced developments)". Project code: 2548.

REFERENCES

1. Tsaplev, V., Konovalov, R., & Abbakumov, K. (2015) Disk bimorph-type piezoelectric energy harvester. *Journal of Power and Energy Engineering, 3*(4), 63–68. doi:10.4236/jpee.2015.34010
2. Erturk, A., & Inman, D. J. (2011) *Piezoelectric Energy Harvesting.* New York: Wiley.
3. Cook-Chennault, K.A., Thambi, N., & Sastry, A.M. (2008). Powering MEMS portable devices – a review of non-regenerative and regenerative power supply systems with emphasis on piezoelectric energy harvesting systems. *Smart Materials and Structures, 17,* 043001, 1–33. doi:10.1088/0964-1726/17/4/043001
4. De Marqui Junior, C., Erturk, A., & Inman, D. J. (2009) An electromechanical finite element model for piezoelectric energy harvester plates. *Journal of Sound and Vibration, 327,* 9–25. doi:10.1016/j.jsv.2009.05.015
5. Shu, Y.C., & Lien, I.C. (2006) Analysis of power output for piezoelectric energy harvesting systems. *Smart Materials and Structures, 15,* 1499–1512.
6. Xiang, J., Wu, Y., & Lu, D. (2006) Energy harvesting from the discrete gust response of a piezoaeroelastic wing: modeling and performance evaluation. *Journal of Sound and Vibration, 343,* 176–193. doi:10.1016/j.jsv.2014.12.023
7. Choi, W.J., Jeon, Y., Jeong, J.H., Sood, R., & Kim, S.G. (2006) Energy harvesting MEMS device based on thin film piezoelectric cantilevers. *Journal of Electroceramics, 17*(2–4), 543–548. doi:10.1007/s10832-006-6287-3
8. Kim, S. (2002) *Low power energy harvesting with piezoelectric generators.* PhD diss., University of Pittsburgh. Retrieved from http://d-scholarship.pitt.edu/10228/1/SHKIMA.pdf

Minicopter Nonlinear Control with the Existence of Disturbances

I. N. Ibrahim [1], S. Hussin [2], I. V. Abramov [3]

[1] Mechatronics and Robotics Dept.
E-mail: ibrncfe@gmail.com
[2] Dept. of Applied Mathematics
E-mail: sulimanh17@gmail.com
[3] Mechatronics and Robotics Dept.
E-mail: abramov@istu.ru
Kalashnikov Izhevsk State Technical University, Izhevsk, Russia

Received: 15.11.2016

Abstract. This paper is focusing on studying the nature of equations of motion of a six degree of freedom of a Minicopter. Choosing a Minicopter is challenging in the field of control because it is a highly nonlinear, multivariable, and underactuated system, in addition to its advantages such as high maneuverability and stationary flight. Underactuated systems, defined as a mechanical system in which the dimension of the configuration space exceeds that of the control input space, that is, with fewer control inputs than the degrees of freedom. Modeling of such a system is not a trivial problem due to the coupled dynamics of the aerial vehicle. The dynamic model is formulated using the Newton - Euler method for translational and rotational dynamics, and the contribution of this work is deriving an accurate and detailed mathematical model. Then disturbances that represent outdoors environment were added to be used in the simulation, the topic, which was unmentioned before in most of the literature. The kinematics and dynamics were studied then equations of motion were explained. The state space model was derived with the existence of disturbances in the earth frame. An application was conducted by LabVIEW simulation program using Runge-Kutta 2 method. Correlations were analyzed on all parameters of motion equations; four slide mode controllers were implemented to stabilize the altitude and attitude. Finally, Lyapunov stability was presented.

Keywords: Minicopter, disturbances, Lyapunov stability, UAV control

1. INTRODUCTION

Nowadays, mini-drones invaded several application domains [1–3]. The control of aerial robot such as Minicopter requires dynamics in order to account for gravity effects and aerodynamic forces [1–2]. These aerial vehicles have high maneuverability and stationary flight [4–5]. In this work equations of motion were concluded of the whole system using the Newton-Euler formulation for translational and rotational dynamics of a rigid body [1, 6]. This paper is focusing on studying the nature of equations like nonlinearity and coupled variables, then adding disturbances that were presented as an environment for outdoors simulation [3, 7–9], which is unmentioned in most of the literature. The structure of the paper is as follows: describing kinematics and dynamics then explain equations of motion.

2. REFERENCE SYSTEMS FOR THE UAV MINICOPTER

In order to describe the Minicopter motion only two reference systems are necessary: earth inertial frame (E-frame) and body-fixed frame (B-frame). An Inertial frame is a system that uses the North, East, and Down (NED) coordinates and the origin of this reference system is fixed in one point located on the earth surface as shown in Figure 1, and the (X, Y, Z) axes are directed to the North, East, and Down, respectively. The mobile frame (XB, YB, ZB) is the body fixed frame that is centered in the Minicopter center of gravity and oriented as shown in Figure 1. The angular position of the body frame with respect to the inertial one is usually defined by means of the Euler angles: roll ϕ, pitch θ, and yaw ψ. As the vector: $\sigma = [\phi \quad \theta \quad \psi]^T$, ϕ and $\theta \in \left]-\frac{\pi}{2}, \frac{\pi}{2}\right[$; $\psi \in]-\pi, \pi[$. The inertial frame position of the vehicle is given by vector $\xi = [x \quad y \quad z]^T$ [1–2, 5–6]. The transformation from the body frame to the inertial frame is realized by using the well-known rotation matrix C_b^n [1, 4, 6]:

$$C_b^n = \begin{bmatrix} c\theta c\psi & s\phi s\theta c\psi - c\phi s\psi & s\phi s\psi + c\phi s\theta c\psi \\ c\theta s\psi & c\phi c\psi + s\phi s\theta s\psi & c\phi s\theta s\psi - s\phi\, c\psi \\ -s\theta & s\phi c\theta & c\phi c\theta \end{bmatrix},$$

which is orthogonal, and $c\theta$ equivalent to $\cos\theta$ also $s\theta$ means $\sin\theta$, while the transformation matrix for angular velocities from the body frame to the inertial one is S [3, 5].

$$S = \begin{bmatrix} 1 & \sin\phi\tan\theta & \cos\phi\tan\theta \\ 0 & \cos\phi & -\sin\phi \\ 0 & \sin\phi\sec\theta & \cos\phi\sec\theta \end{bmatrix},$$

where $\dot{\sigma} = S.\Omega$, $\dot{\xi} = C_b^n.V$, the angular velocity Ω is defined by the vector $\Omega = [p\, q\, r]^T$, and the linear velocity is defined by the vector $V = [u\, v\, w]^T$ in the body frame [1–6].

3. AERODYNAMIC FORCES AND MOMENTS IN AXIAL FLIGHT

The UAV Minicopter systems are quite complex; their movements are governed by several effects either mechanical or aerodynamic. Our aim is to provide the mathematical equations driving the dynamical behavior of the Minicopter by means of a generalization of the Quadcopter model presented in [1, 5–7]. The motion of a rigid body can be decomposed into the translational and rotational components. Therefore, in order to describe the dynamics of the Minicopter, assumed to be a rigid body, the Newton-Euler equations, that govern linear and angular motion are used. In order to get equations of motion of entire system, the following assumptions have been made:

- The Minicopter is a rigid body.
- The Minicopter has a symmetrical structure.

Therefore, the following equations are obtained:

$$\begin{bmatrix} m I_{3\times 3} & 0_{3\times 3} \\ 0_{3\times 3} & J \end{bmatrix} \begin{bmatrix} \dot{V} \\ \dot{\Omega} \end{bmatrix} + \begin{bmatrix} \Omega \times (mV) \\ \Omega \times (J\Omega) \end{bmatrix} = \begin{bmatrix} \Sigma F \\ \Sigma M \end{bmatrix}.$$

3.1. Force Analysis

a. Thrust Force

The main force affecting the aircraft movement is the thrust force resulting from the motors and propellers that leads to raise the aircraft in the air. The model consists of 6 motors, and according to the suggested engineering model, the motors in the model are parallel and perpendicular on the aircraft surface, so we conclude that the total thrust force vector of the aircraft is T and it is the sum of the propellers thrust force vectors $\sum_{i=1}^{6} T_i$. The main rotor thrust T orientation is expressed in terms of the lateral and longitudinal cyclic tilt angles a and b (Fig. 1) [4].

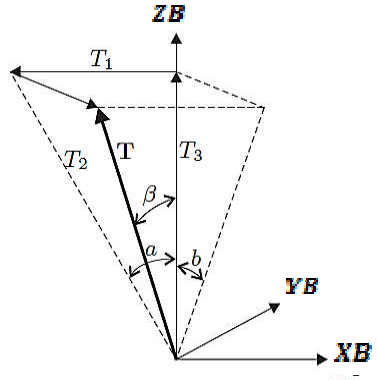

Figure 1. Thrust vector

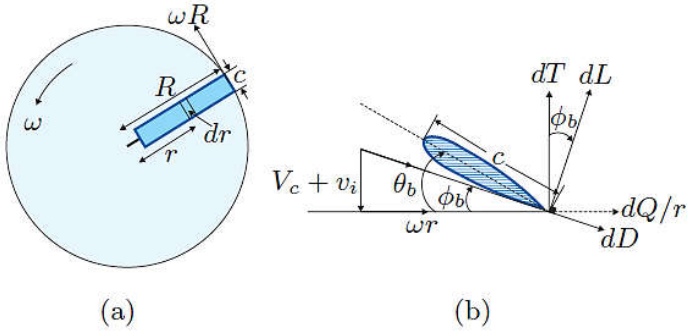

Figure 2. Force components on blade in vertical flight

Then, the main rotor thrust may be expressed as a vector in the body fixed fame as: $T = \frac{1}{\sqrt{1-\sin^2 a \sin^2 b}} \begin{bmatrix} \sin a \cos b \\ \cos a \sin b \\ \cos a \cos b \end{bmatrix} .|T|$. By applying the small-angle assumption T, the total lift of the main Minicopter tilted in comparison to the motor shaft can be rewritten as: $T = |T|.[a \quad b \quad 1]^T$. The aerodynamic forces and moments are derived using a momentum combination; the left force depends on the angular velocity ω and the geometric dimensions of propellers as seen in a top view of the rotor disc in Fig. 2-a where blade rotation is counter-clockwise with angular velocity ω. The blade radius is R; the tip speed therefore is ωR. An elementary blade section is taken at radius r of chord length c and span-wise width d_r. Forces on the blade section are shown in Fig. 2-b. The flow seen by the section has velocity components: ωr in the disc plane, (V_c + v_i) in the axial, and induced velocities perpendicular to it. The angle θ_b denotes the blade pitch angle, and ϕ_b is the inflow angle. In addition, dT, dQ, dL, and dD are the elementary thrust, torque, lift, and drag forces respectively. The thrust and torque, are [5]: $|T_i| = \rho C_T A R^2 \omega_i^2$, $|Q_i| = \rho C_Q A R^3 \omega_i^2$, where blade rotation is with angular velocity ω, the blade radius is R, C_T and C_Q are the thrust and torque coefficients respectively, ρ is the air density, and A the disc area. The thrust and torque coefficients can be written as:

$$C_T = \frac{1}{4}\sigma C_{L\alpha}\left[\frac{2\theta_b}{3} - (\gamma_c + \gamma_i)\right], \quad C_Q = \frac{1}{2}\sigma[C_{L\alpha}(\gamma_c + \gamma_i)\left\{\frac{\theta_b}{3} - \frac{\gamma_c + \gamma_i}{2}\right\} + \frac{C_D}{4},$$

where σ is the rotor solidity, $C_{L\alpha}$ is the lift slope coefficient, C_D is the drag coefficient γ_c, and γ_i are the inflow factors [5]. Finally, the total force of thrust generated by the six propellers in the earth frame is defined as:

$$F_{TI} = C_b^n \begin{bmatrix} 0 \\ 0 \\ \sum_{i=1}^{6} |T_i| \end{bmatrix}_B = \begin{bmatrix} (c\phi\, c\psi\, s\theta + s\phi\, s\psi) \sum_{i=1}^{6} |T_i| \\ (c\phi\, s\theta\, s\psi - s\phi\, c\psi) \sum_{i=1}^{6} |T_i| \\ (c\phi\, c\theta) \sum_{i=1}^{6} |T_i| \end{bmatrix}_E .$$

b. Drag Force

It is the opposing force to the travelling of the Minicopter in air, which is resulting from the aerodynamic friction, air density, velocity, and can be expressed by the following equation at the earth's frame: $F_{AI} = K_{TI}.\dot{\xi}$, where K_{TI} is a diagonal matrix related to the aerodynamic friction constant k_t [4][5].

c. Gravitational Force

The gravity force is directed toward the center of the earth and the relation of gravity force in the earth frame by [1][2]: $F_{GI} = m[0 \;\; 0 \;\; g]_E^T$.

d. Disturbance Force

Other forces like Coriolis force from the earth, wind, and Euler forces are considered as **disturbances, summarized as F_{DI} in the Earth frame: F_{DI}=$[F_{dIx} \;\; F_{dIy} \;\; F_{dIz}]_E^T$. Therefore, the** equations of motion that govern the translational motion with respect to the Earth frame are:

$$\Sigma M = M_T - M_{AI} + M_{gyro} + M_{DI} = J.\dot{\Omega} + \Omega \times (m.\Omega)$$

$$\begin{bmatrix} M_p \\ M_q \\ M_r \end{bmatrix}_E - \begin{bmatrix} k_r \dot{\phi}^2 \\ k_r \dot{\theta}^2 \\ k_r \dot{\psi}^2 \end{bmatrix}_E + \begin{bmatrix} 0 \\ 0 \\ J_r \dot{\omega}_r \end{bmatrix}_E + \begin{bmatrix} 0 \\ 0 \\ J_r \dot{\omega}_r \end{bmatrix}_E + \begin{bmatrix} M_{dI\phi} \\ M_{dI\theta} \\ M_{dI\psi} \end{bmatrix}_E = J \begin{bmatrix} \ddot{x} \\ \ddot{y} \\ \ddot{z} \end{bmatrix}_E ,$$

where $\Omega \times (m.\Omega)$ has a small effect and approximately equal to zero. Therefore, the equations after some simplifications will be:

$$\left\langle \begin{array}{l|l} \ddot{x} = U_x - \dfrac{k_t}{m}\dot{x} + \dfrac{F_{dIx}}{m} & U_x = (c\phi c\psi s\theta + s\phi s\psi) u_T / m = a_x(\phi,\theta,\psi) \sum_{i=1}^{6} \omega_i^2 \\ \ddot{y} = U_y - \dfrac{k_t}{m}\dot{y} + \dfrac{F_{dIy}}{m} & U_y = (c\phi s\theta s\psi - s\phi c\psi) u_T / m = a_y(\phi,\theta,\psi) \sum_{i=1}^{6} \omega_i^2 \\ \ddot{z} = U_z - \dfrac{k_t}{m}\dot{z} - g + \dfrac{F_{dIz}}{m} & U_z = (c\phi c\theta) u_T / m = a_z(\phi,\theta) \sum_{i=1}^{6} \omega_i^2 \\ & u_T = \sum_{i=1}^{6} |T_i| = \rho C_T A R^2 \sum_{i=1}^{6} \omega_i^2 \\ & a = \dfrac{k_t}{m} \to 0 \end{array} \right\rangle .$$

Therefore, the final equations with respect to the earth frame are:

$$\begin{bmatrix}\ddot{x}\\ \ddot{y}\\ \ddot{z}\end{bmatrix}=\begin{bmatrix}-a\dot{x}+U_x\\ -a\dot{y}+U_y\\ -a\dot{z}+U_z-g\end{bmatrix}+\begin{bmatrix}\frac{F_{dIx}}{m}\\ \frac{F_{dIy}}{m}\\ \frac{F_{dIz}}{m}\end{bmatrix}=\begin{bmatrix}U_x\\ U_y\\ U_z-g\end{bmatrix}+\begin{bmatrix}\frac{F_{dIx}}{m}\\ \frac{F_{dIy}}{m}\\ \frac{F_{dIz}}{m}\end{bmatrix}.$$

3.2. Moments Analysis

The aircraft is affected by several types of moments: the thrust moment resulting from the motors, the motors inertia moment, the aerodynamic moment, and the disturbances moment. Supposing, the inertia matrix of the aircraft is *J*, the structure of the aircraft is symmetric, and the inertia matrix is of the following form: $J=[J_{xx}\ 0\ 0;\ 0\ J_{yy}\ 0;\ 0\ 0\ J_{zz}]^T$; $J\in R_{3\times3}$ [5], therefore, the moments acting on the center of the aircraft can be analyzed in the following:

a. Propeller Moments

The moment M_{thrust} is part of the external moments, that described by the propeller thrust $\sum_{i=1}^{6}T_i$ generated by the propellers, and the distance l from CG to the center of the propeller. The attitude of the vehicle in the air, i.e., Euler angles $\sigma=[\phi\ \theta\ \psi]^T$ change, by controlling the angular velocity of the motors. This means, there is a different thrust moment over time $M_T=[M_p\ M_q\ M_r]^T$, where M_p, M_q, M_r are the moments about the axes X_B, Y_B, Z_B in the body frame [1, 3, 4], noticing that the torque vectors across each other are in the same direction, and the motors that are closest to each other have torque vectors in opposite directions as in Fig. 3.

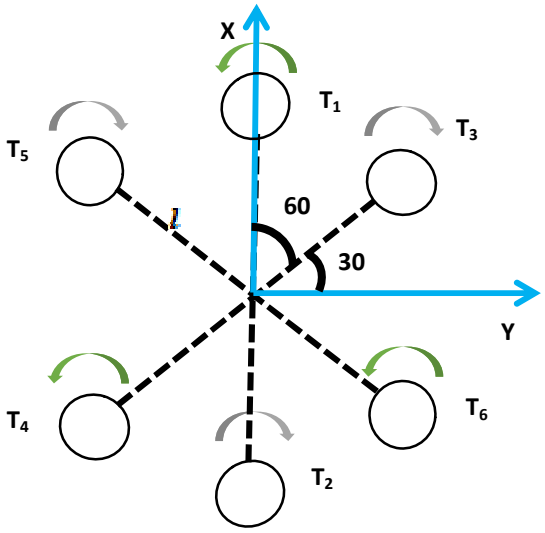

Figure 3. Minicopter architecture

This is the design requirement to keep the Minicopter from spinning out of control [1, 5, 7]. The moments generated by motors as shown in Figure 3, can be explained as follows:

$$M_T = \begin{bmatrix} \frac{\sqrt{3}}{2} l\left(|T_3| - |T_4| - |T_5| + |T_6|\right) \\ \frac{1}{2} l\left(|T_3| - |T_4| + |T_5| - |T_6| + 2|T_1| - 2|T_2|\right) \\ \rho C_Q A R^3 \left(\omega_1^2 + \omega_4^2 + \omega_6^2 - \omega_2^2 - \omega_3^2 - \omega_5^2\right) \end{bmatrix}.$$

b. The aerodynamic moment

It is the moment resulting from the aerodynamic friction in air and is proportional to the torque around the axes, and it is expressed by the following equation: $M_{AI} = K_{RI}.\Omega^2 = K_{RI}\left[\dot{\phi}^2 \;\; \dot{\theta}^2 \;\; \dot{\psi}^2\right]^T$, where K_{RI} is a diagonal matrix related to the rotational aerodynamic friction constant by the parameter k_r [4–5].

c. Disturbance moment

It is the total of the disturbances affecting the torque around the aircraft axes resulting from disturbances in the motors movement, the wind, and the load in the aircraft, expressed as: $M_{DI} = \left[M_{dI\phi} \;\; M_{dI\theta} \;\; M_{dI\psi}\right]^T$.

d. Propeller Gyroscopic effect

The rotation of the propellers produces a gyroscopic effect: $M_{gyro} = \left[-J_r \dot{\theta}\omega_r \;\; J_r \dot{\phi}\omega_r \;\; 0\right]^T$ [3], where J_r is the rotational inertia of the propeller $\left[NmS^2\right]$, and ω_r $[rad/S]$ is the overall propeller speed: $\omega_r = -\omega_1 + \omega_2 - \omega_3 + \omega_4 - \omega_5 + \omega_6$.

e. Yaw counter moment

Differences in rotational acceleration of the propellers produces a yaw inertial counter moment as follow: $M_{counter} = [0 \;\; 0 \;\; J_r \dot{\omega}_r]^T$ [3]. Therefore, the equations of motion that govern the rotational motion with respect to the body frame are:

$$\Sigma M = M_T - M_{AI} + M_{gyro} + M_{counter} + M_{DI} = J.\dot{\Omega} + \Omega \times (m.\Omega)$$

$$\begin{bmatrix} M_p \\ M_q \\ M_r \end{bmatrix}_E - \begin{bmatrix} k_r \dot{\phi}^2 \\ k_r \dot{\theta}^2 \\ k_r \dot{\psi}^2 \end{bmatrix}_E + \begin{bmatrix} -J_r \dot{\theta}\omega_r \\ J_r \dot{\phi}\omega_r \\ 0 \end{bmatrix}_E + \begin{bmatrix} 0 \\ 0 \\ J_r \dot{\omega}_r \end{bmatrix}_E + \begin{bmatrix} M_{dI\phi} \\ M_{dI\theta} \\ M_{dI\psi} \end{bmatrix}_E = J \begin{bmatrix} \dot{p} \\ \dot{q} \\ \dot{r} \end{bmatrix}_E + \begin{bmatrix} p \\ q \\ r \end{bmatrix} \times J \begin{bmatrix} p \\ q \\ r \end{bmatrix},$$

$$\left\langle \begin{array}{l|l} \dot{p} = \dfrac{M_p}{J_x} + qr\dfrac{(J_y - J_z)}{J_x} - \dfrac{k_r}{J_x}p - \dfrac{J_r}{J_x}\dot{\theta}\omega_r + \dfrac{M_{dI\phi}}{J_x} & \textit{Transformation} \quad \textit{Equation} \\ \dot{q} = \dfrac{M_q}{J_y} + pr\dfrac{(J_z - J_x)}{J_y} - \dfrac{k_r}{J_y}q + \dfrac{J_r}{J_y}\dot{\phi}\omega_r + \dfrac{M_{dI\theta}}{J_y} & \dot{\sigma} = \begin{bmatrix} \dot{\phi} \\ \dot{\theta} \\ \dot{\psi} \end{bmatrix}_E = S.\begin{bmatrix} p \\ q \\ r \end{bmatrix}_B \\ \dot{r} = \dfrac{M_r}{J_z} + pq\dfrac{(J_x - J_y)}{J_z} - \dfrac{k_r}{J_z}r + \dfrac{J_r}{J_z}\dot{\omega}_r + \dfrac{M_{dI\psi}}{J_z} & \end{array} \right\rangle .$$

Transformation matrix $S \to I$ when the hexa-copter tends to the stable point, therefore the equations of angular rate will be related to the Earth frame, in addition to some assumptions: $\dfrac{J_r}{J_x} = \dfrac{J_r}{J_y} = \dfrac{J_r}{J_z} \to 0$ is a small effect around zero, and $J_x = J_y$. Then the equations will be as follows:

$$\left\langle \begin{array}{l|l} & U_p = \dfrac{M_p}{J_x} = \dfrac{\sqrt{3}\rho l C_T A R^2}{2J_x}\left(\omega_3^2 + \omega_6^2 - \omega_4^2 - \omega_5^2\right) \\ & U_p = a_\phi\left(\omega_3^2 + \omega_6^2 - \omega_4^2 - \omega_5^2\right) \\ \ddot{\phi} = U_p + b_1\dot{\theta}\dot{\psi} + c_1\dot{\phi}^2 + \dfrac{M_{dI\phi}}{J_x} & U_q = \dfrac{M_q}{J_y} = \dfrac{\rho l C_T A R^2}{2J_y}\left(\omega_3^2 + \omega_5^2 + 2\omega_1^2 - \omega_4^2 - \omega_6^2 - 2\omega_2^2\right) \\ \ddot{\theta} = U_q + b_2\dot{\phi}\dot{\psi} + c_2\dot{\theta}^2 + \dfrac{M_{dI\theta}}{J_y} & U_q = a_\theta\left(\omega_3^2 + \omega_5^2 + 2\omega_1^2 - \omega_4^2 - \omega_6^2 - 2\omega_2^2\right) \\ \ddot{\psi} = U_r + c_3\dot{\psi}^2 + \dfrac{M_{dI\psi}}{J_z} & U_r = \dfrac{M_r}{J_z} = \dfrac{\rho l C_Q A R^3}{2J_z}\left(\omega_1^2 + \omega_4^2 + \omega_6^2 - \omega_2^2 - \omega_3^2 - \omega_5^2\right) \\ & U_r = a_\psi\left(\omega_1^2 + \omega_4^2 + \omega_6^2 - \omega_2^2 - \omega_3^2 - \omega_5^2\right) \\ & b_1 = \dfrac{J_y - J_z}{J_x}, b_2 = \dfrac{J_z - J_x}{J_y}, c_1 = -\dfrac{k_r}{J_x}, c_2 = -\dfrac{k_r}{J_y}, c_3 = -\dfrac{k_r}{J_z} \end{array} \right\rangle .$$

Figure 4 shows the diagram of the control system model using LabVIEW application that contains the programming of the equations of motion. These equations require entering the input variables and physical characteristics for getting the state variables.

4. State Space Model

The dynamics model presented in the translational and rotational equation set can be re-written in the state-space form as:

$$\dot{X} = f(X,U) + \delta.$$

where δ is the disturbances, and the $X \in \mathbf{R}^{12}$ is the vector of state variables given as follow:

$$X = [x \quad \dot{x} \quad y \quad \dot{y} \quad z \quad \dot{z} \quad \phi \quad \dot{\phi} \quad \theta \quad \dot{\theta} \quad \psi \quad \dot{\psi}]^T.$$

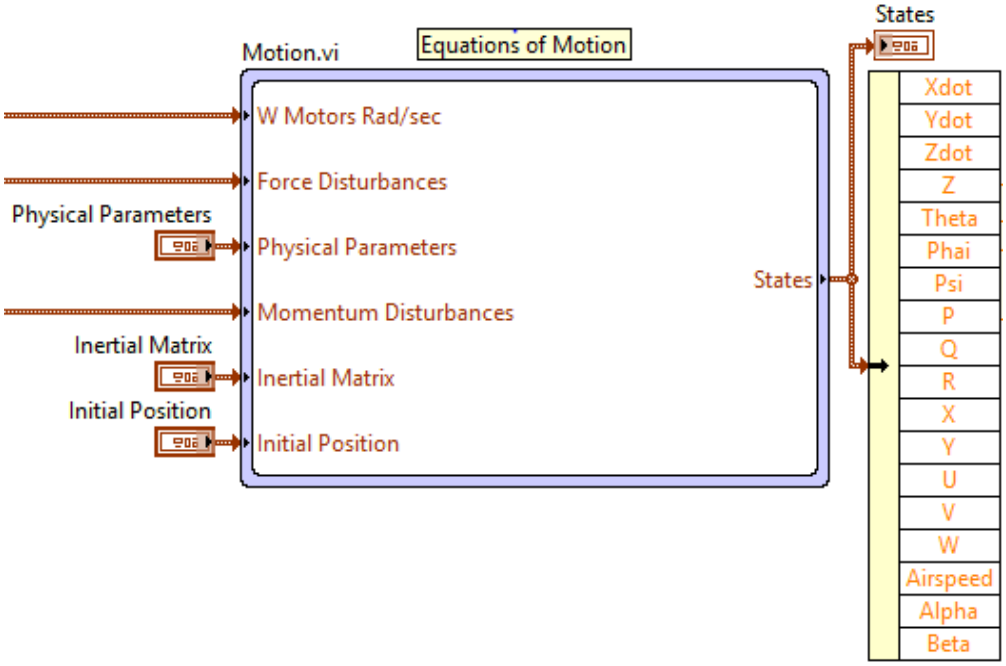

Figure 4. Mathematical model designed in LabVIEW

Then we can conclude to the final equations of the system in state space, which governs the transitional and rotational of the hexa-copter with respect to the Earth Frame, as follows:

$$\begin{pmatrix}\dot{x}_2\\ \dot{x}_4\\ \dot{x}_6\end{pmatrix}=\begin{pmatrix}-a & 0 & 0\\ 0 & -a & 0\\ 0 & 0 & -a\end{pmatrix}\begin{pmatrix}x_2\\ x_4\\ x_6\end{pmatrix}+\begin{pmatrix}1 & 0 & 0\\ 0 & 1 & 0\\ 0 & 0 & 1\end{pmatrix}\begin{pmatrix}U_x\\ U_y\\ U_z\end{pmatrix}+\begin{pmatrix}F_{dIx}/m\\ F_{dIy}/m\\ \frac{F_{dIz}}{m}-g\end{pmatrix}=\begin{pmatrix}U_x\\ U_y\\ U_z\end{pmatrix}+\begin{pmatrix}F_{dIx}/m\\ F_{dIy}/m\\ \frac{F_{dIz}}{m}-g\end{pmatrix};$$

$$\begin{pmatrix}\dot{x}_8\\ \dot{x}_{10}\\ \dot{x}_{12}\end{pmatrix}=\begin{pmatrix}b_1x_{10}x_{12}+c_1x_8^2\\ b_2x_8x_{12}+c_2x_{10}^2\\ b_3x_8x_{10}+c_3x_{12}^2\end{pmatrix}+\begin{pmatrix}1 & 0 & 0\\ 0 & 1 & 0\\ 0 & 0 & 1\end{pmatrix}\begin{pmatrix}U_p\\ U_q\\ U_r\end{pmatrix}+\begin{pmatrix}M_{dI\phi}/J_x\\ M_{dI\theta}/J_x\\ M_{dI\psi}/J_x\end{pmatrix}.$$

The suggested real and complex dynamics mathematical model were derived as shown in the equations before. Basically, this model was consisting of 6 equations and characterized by nonlinearity, time-variance, and coupling among the system variables where any change in the input variables leads to changes in most of the output variables. The control mechanism consists of two-level control, the first level controls the horizontal motion using the input vector $U_1=[U_x \quad U_y]^T$, while the next level controls the attitude and altitude motion using the control vector $U_2=[U_p \quad U_q \quad U_r \quad U_z]^T$, and the command control of the Minicopter is vector $D=[x_d \quad y_d \quad z_d \quad \psi_d]^T$, which gives the position and rotation in the space. Furthermore, the horizontal control (x, y) depends on the angles ϕ, θ of the aircraft. With respect to the control input vector $U=[U_x \quad U_y \quad U_z \quad U_p \quad U_q \quad U_r]^T$, it is clear that the rotational subsystem is fully-actuated, it is only dependent on the rotational state variables x_7 to x_{12},

while the translational subsystem is under-actuated as it is dependent on both the translational state variables x_1 to x_6 and the rotational ones x_7 to x_{12}. The control strategy is through controlling the motors speed variables $\omega_1, \omega_2 \ldots \omega_6$ by a defined style explained as follows:

1. There are 3 movements that describe all possible combinations of attitude: Roll (rotation around the *X* axis by angle ϕ), Pitch (rotation around the *Y* axis by angle θ), and Yaw (rotation around the *Z* axis by angle ψ). The roll control is obtained by changing the velocity of motors 3, 4, 5, 6, and this movement is called lateral motion. Then the pitch control is obtained by changing the velocity of all motors, resulting in the longitudinal motion. Finally, the yaw control is obtained by changing the velocity of all motors.

2. The change of motors speed for attitude control should be fixed and based on differential control strategy as seen in Fig. 3 and equations of moments, i.e., the Pitch control around axis *Y* is obtained by changing the torques around this axis by increasing (T_1, T_3, T_5) and decreasing another side (T_2, T_4, T_6) using the following equation:

$$Pitch\_control \Leftrightarrow l \times \cos 60 \times \left(|T_3| - |T_4| + |T_5| - |T_6|\right) + |T_1| - |T_2|.$$

The roll control is obtained as follows:

$$roll\_control \Leftrightarrow l \times \cos 30 \times \left(|T_3| - |T_4| - |T_5| + |T_6|\right).$$

While the yaw control is based on the torque difference between the neighboring motors:

$$yaw\_control \Leftrightarrow Q_1 + Q_4 + Q_6 - Q_2 - Q_3 - Q_5.$$

3. Altitude control is obtained by changing all motors' velocity with a fixed change. This is based on the force equations in Z component, noticing that the thrust is equivalent to the square of the motors angular velocities. To increase the altitude, all motors velocities must be increased, and vice versa. The equation that governs the altitude is:

$$altitude\_control \Leftrightarrow \sum_{i=1}^{6} |T_i|.$$

From the control problem based on Fig. 5 and its angular speed correction, which govern the attitude and altitude in space, the artificial vector $U_2 = [U_p \quad U_q \quad U_r \quad U_z]^T$ can be found. This simplifies the control of the system in Pitch, Roll, Yaw and altitude movements instead of using real motors' velocities vector ω [5]. Now we can put the equations that connect between artificial and real input vectors as follows:

$$\begin{bmatrix} U_P \\ U_q \\ U_r \\ U_z \end{bmatrix} = \begin{bmatrix} 0 & 0 & +a_\phi & -a_\phi & -a_\phi & +a_\phi \\ 2a_\theta & -2a_\theta & +a_\theta & -a_\theta & +a_\theta & -a_\theta \\ +a_\psi & -a_\psi & -a_\psi & +a_\psi & -a_\psi & +a_\psi \\ +a_z & +a_z & +a_z & +a_z & +a_z & +a_z \end{bmatrix} \cdot \begin{bmatrix} \omega_1^2 \\ \omega_2^2 \\ \omega_3^2 \\ \omega_4^2 \\ \omega_5^2 \\ \omega_6^2 \end{bmatrix}.$$

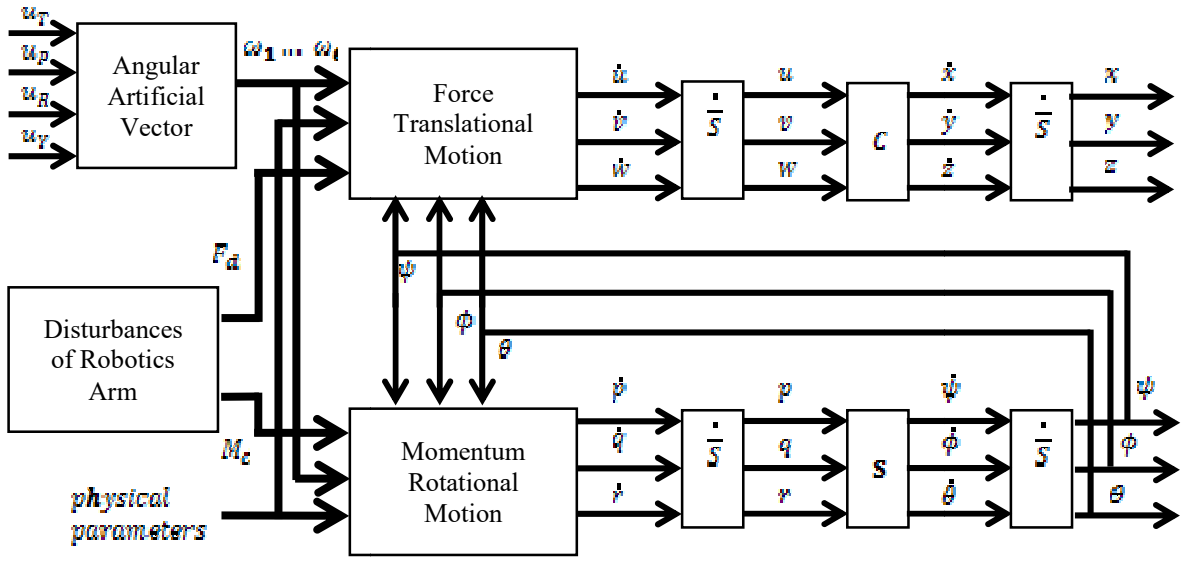

Figure 5. Block diagram of a dynamical system for Minicopter

5. Slide Mode Control and Lyapunov Stability

The sliding mode controller designing procedure is exerted in two steps. Firstly, the choice of the sliding surface (S) is produced according to the tracking error; in the second step a Lyapunov function is considered verifying the necessary condition for the stability in Lyapunov law. The sliding mode control of the state variables estimated dynamics is presented by establishing the statement of the control input. The sliding surfaces are described as follows [4, 8–9]:

$$S_x = e_2 + \lambda_1 e_1, \quad S_y = e_4 + \lambda_2 e_3, \quad S_z = e_6 + \lambda_3 e_5,$$
$$S_p = e_8 + \lambda_4 e_7, \quad S_q = e_{10} + \lambda_5 e_9, \quad S_r = e_{12} + \lambda_6 e_{11}$$

such that $\lambda_i > 0$ and $e_i = x_{id} - x_i$, $i \in [1,11]$, $e_{i+1} = \dot{e}_i$. The following Lyapunov function is chosen: $V(S_x) = \frac{1}{2} S_x^2$, then the necessary sliding condition is verified and Lyapunov stability is guaranteed. The chosen law for the attractive surface is the time derivative of $V(S_x)$ satisfying $(S_x \dot{S}_x < 0)$ [8, 9] where:

$$\dot{S}_x = -k_1 sign(S_x) = \dot{x}_{2d} - \dot{x}_2 + \lambda_1 \dot{e}_1 = \ddot{x}_{1d} + a x_2 - U_x - \frac{F_{dIx}}{m} + \lambda_1 \dot{e}_1$$

$$U_x = -k_1 sign(S_x) + a x_2 - \frac{F_{dIx}}{m} + \ddot{x}_d + \lambda_1 e_2$$

The same steps are followed to extract U_y, U_z, U_p, U_q, U_r:

$$U_y = -k_2 \,\mathrm{sign}(S_y) + a x_4 - \frac{F_{dIy}}{m} + \ddot{y}_d + \lambda_2 e_4,$$

$$U_z = -k_3 \,\mathrm{sign}(S_z) + a x_6 - \frac{F_{dIz}}{m} + g + \ddot{z}_d + \lambda_3 e_6,$$

$$U_p = -k_4 \operatorname{sign}(S_p) - b_1 x_{10} x_{12} - c_1 x_8^2 - \frac{M_{dI\phi}}{j_x} + \ddot{p}_d + \lambda_4 e_8,$$

$$U_q = -k_5 \operatorname{sign}(S_q) - b_2 x_8 x_{12} - c_2 x_{10}^2 - \frac{M_{dI\theta}}{j_y} + \ddot{q}_d + \lambda_5 e_{10},$$

$$U_r = -k_6 \operatorname{sign}(S_r) - b_3 x_8 x_{10} - c_3 x_{12}^2 - \frac{M_{dI\psi}}{j_x} + \ddot{r}_d + \lambda_6 e_{12}.$$

6. Experiments and Results

The system's parameters that are used in the simulation of the model, are listed in table 1. Real and complex dynamics model was taken into account, which has addressed the nonlinearity, time variance, under-actuation, and disturbances with respect to the earth frame. An application was conducted by LabVIEW simulation program using Runge-Kutta 2 method with fixed step 0.05 (sec). Correlations were analyzed on all parameters of motion equations; four slide mode controllers were implemented to stabilize the altitude and attitude as shown in figures (6) to (9) that we may notice the stability and disturbances free as possible in our response with multiple set points taken into account. The tuning process achieved after multi attempts of experiments. Our scenario is the hovering flight at altitude 10 meters in the air.

Table 1. Parameters used in the simulation

m=4 kg	**g=9.806 m/s^2**	**l=0.36 m**
I_x, I_y = 3.8e^{-3} N.m.s^2/rad	R = 0.15 m	k_t = 4.8e^{-2} N.s/m
I_z = 7.1e^{-3} N.m.s^2/rad	A = 0.071 m^2	k_r = 6.4e^{-4} N.m.s/rad
C_T = 0.01458	C_Q = 1.037e^{-3}	ρ = 1.293 kg/m^3

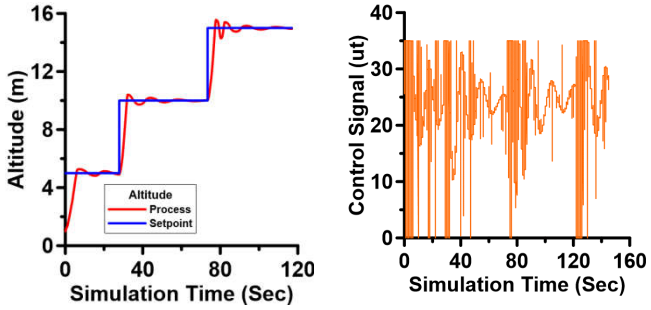

Figure 6. Stability response of altitude and control signal

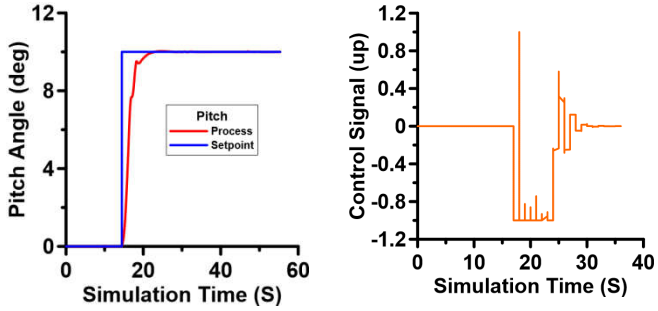

Figure 7. Stability response of pitch angle and control signal

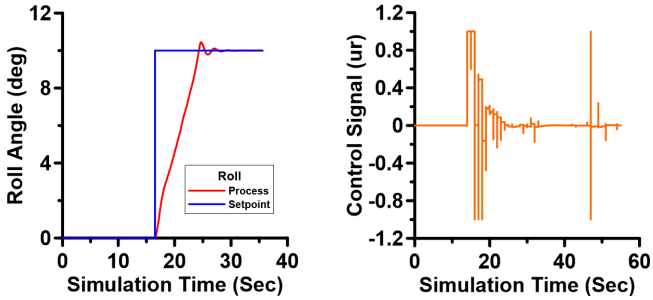

Figure 8. Stability response of roll angle and control signal

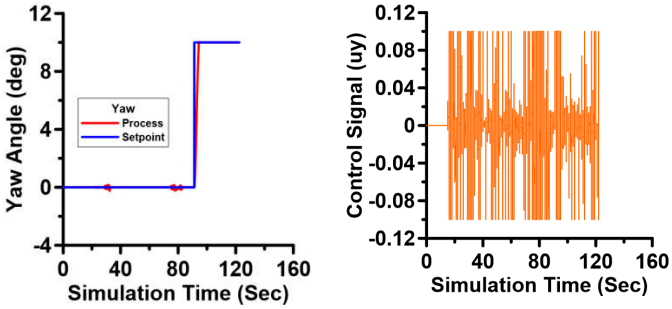

Figure 9. Stability response of yaw angle and control signal

7. The Conclusion

In this work, controllers were designed and were tuned in order to control a Minicopter, a special type of UAV. In this paper, real and complex dynamics model was taken into account, which has addressed the nonlinearity, time variance, under-actuation, and disturbances with respect to the earth frame. An application was conducted by LabVIEW simulation program using Runge-Kutta 2 method. Correlations were analyzed on all parameters of motion equations; four slide mode controllers were implemented to stabilize the altitude and attitude. The stability and disturbances free as possible in our response with multiple set points taken into account. The tuning process achieved after multi attempts of experiments. Future work is to develop a precise trajectory control by using robust techniques to stabilize the whole system and drive the Minicopter to the desired trajectory of Cartesian position, attitude, and airspeed.

References

1. Bouadi, H., & Tadjine, M. (2007). Nonlinear observer design and sliding mode control of four rotors helicopter. *World Academy of Science, Engineering and Technology. International Journal of Aerospace and Mechanical Engineering, 1*(7), 329–335. urn:dai:10.1999/1307-6892/1748
2. Abas, N., Legowo, A., & Akmeliawati, R. (2011, May). Parameter identification of an autonomous quadrotor. In *4th International Conference on Mechatronics (ICOM), 2011,* 1–8. doi:10.1109/ICOM.2011.5937198
3. Fogelberg, J. (2013). *Navigation and autonomous control of a minicopter in indoor environments.* Msc Thesis. Lund, Sweden: Lund University. ISSN 0280-5316.
4. Moussid, M., Sayouti, A., & Medromi, H. (2015). Dynamic modeling and control of a hexarotor using linear and nonlinear methods. *International Journal of Applied Information Systems, 9*(5). 9–17. doi:10.5120/ijais2015451411
5. Sanca, A. S., Alsina, P. J., & Cerqueira, J. J. F. (2010). Dynamic modeling with nonlinear inputs and backstepping control for a hexarotor multi-aerial vehicle. *Latin American Robotics Symposium and Intelligent Robotic Meeting (LARS)*. doi:10.1109/LARS.2010.14

6. Ibrahim, N. I. (2016). Modeling and predictive control of nonlinear coupled and underactuated dynamics of a hexacopter. *Bulletin of Kalashnikov ISTU, 19*(4), 35–38. doi:10.22213/2413-1172-2016-4-35-38
7. Di Lucia, S., Tipaldi, G. D., & Burgard, W. (2015). Attitude stabilization control of an aerial manipulator using a quaternion-based backstepping approach. *European Conference on Mobile Robots (ECMR), 2015*. doi:10.1109/ECMR.2015.7324191
8. Bouadi, H., Bouchoucha, M., & Tadjine, M. (2007). Sliding mode control based on backstepping approach for an UAV type-quadrotor. International Journal of Mechanical and Mechatronics Engineering, 1(2), 39–44. urn:dai:10.1999/1307-6892/11524
9. Bouabdallah, S., & Siegwart, R. (2005, April). Backstepping and sliding-mode techniques applied to an indoor micro quadrotor. In *Proceedings of the 2005 IEEE International Conference on Robotics and Automation (ICRA), 2005*, 2247–2252. doi:10.1109/ROBOT.2005.1570447

Determination of Organic Contaminants Concentration on the Silica Surface by Lateral Force Microscopy

N. Ivliev [1,2], V. Kolpakov [2], S. Krichevskiy [2], N. Kazanskiy [1,2]

[1] Image Processing Systems Institute of RAS, Branch of the FSRC "Crystallography and Photonics" RAS
E-mail: ivlievn@gmail.com
[2] Samara National Research University
Samara, Russia

Received: 25.11.2016

Abstract. We present a method for determining the concentration of organic contaminants on the silica surface by using lateral force maps and surface topology images obtained with scanning probe microscopy. In this study, we optimized the scanning frequency to increase image contrast and facilitate interpreting data obtained. We also proved experimentally that the sensitivity of the method reaches 10^{-11} g/cm^2.

Keywords: concentration of organic contaminants, surface, lateral force

INTRODUCTION

Monitoring the surface cleanliness of semiconductor and dielectric substrates finds wide application in micro- and nanoelectronics [1–3], diffractive optics [4, 5], and nanophotonics [6]. This is necessitated by adsorbed contamination, which causes changes in electro-physical surface properties [7, 8], deteriorates the adhesion of applied process layers [9, 10], increases the thickness of surface oxide during thermal oxidation [11], and thus deteriorates the operating characteristics of the fabricated element or results in its failure.

Micro- and nanominiaturization of fabricated structures leads to higher requirements for the cleanliness of substrate surfaces. Today the allowable carbon-atom concentration for fabricating semiconductor devices is 10^{12} atoms/cm^2 [12]. The value is that low because carbon atoms have a significant effect on local surface conductivity. According to [11, 13, 14], those organic-compound molecules that, even under clean-room conditions, come from plasticizers in plastic products (such as polyethylene packaging for substrates and Petri dishes) present carbon contamination that is hardest to remove. Therefore, monitoring such contamination is a priority.

Using modern techniques based on mass spectrometry [15, 16] and multiple internal reflection infrared spectroscopy [1, 17] to assess the concentration of organic contaminants makes it possible to attain the required sensitivity. But those techniques do not yield information on how the molecules are distributed across the surface, although that information is needed in the case of nonuniform contamination.

Studies [18–20] present AFM (atomic force microscopy) methods based on the registration of lateral forces (LF) acting on the atomic force microscope's probe that is in constant con-tact with the surface. Probe scanning along a line in two directions rules out the forces caused by surface roughness. Thus, LF maps obtained from the measurement result from the action of adhesion bonds between the probe and the surface, and the bonds energies characterize the chemistry of the phase boundary. This can be used for assessing the concentration and distribution of surface contaminants.

Thus, this paper aims to study the local tribological properties of substrates with the AFM method of lateral forces in order to realize the method for determining the concentration of organic contaminants.

THEORETICAL ANALYSIS

Molecules of organic contaminants adsorb on the surface and interact with electronic states at the surface. The energy of that interaction corresponds to the van der Waals forces and depends on the structure of adsorbed molecules [21].

Dioctyl- and dibutyl phthalate are the most commonly used industrial plasticizers. The presence of C=O and −OH groups in the molecular structure of these cyclic hydrocarbons determines their strong polarity, and the polarity causes the surface and the contaminant to bond. The energy of that bond is, in this case, determined by the hydrogen bridges formed with the −OH groups of the native oxide as well as by the orientation interaction between the dipole and the surface. The value of the orientation interaction can be calculated with the expression [22]:

$$E_{or} = -\frac{2p_1p_2}{r^3}, \tag{1}$$

where p_1, p_2 – dipole moments of a contaminant molecule and the −OH group, respectively; r – length of the O···HO hydrogen bond.

The energy of the O···HO hydrogen bond is 21.5 kJ/mol [23]. Therefore, given the orientation interaction calculated with (1), the aggregate bond energy of the substances in question reaches 50 kJ/mol, a value close to a stable chemical bond that is difficult to break. Therefore, the force that acts on the surface from the AFM probe during the measurement and that equals dozens of nanonewtons cannot cause dioctyl- and dibutyl phthalate molecules to desorb.

AFM methods make it possible to register only the molecular concentration of contaminants – that is, the methods cannot measure the concentration of carbon atoms in atoms per square centimeter. That dimension is comparable with the dimension of the mass concentration of organic contaminants under ISO 14644-10–2013 in grams per square centimeter through the use of the expression [24, 25]:

$$C_{mol} = \frac{C_{at}M}{N_AN_c}, \tag{2}$$

where C_{mol} – mass concentration of organic contaminants; C_{at} – concentration of carbon atoms; N_A – Avogadro constant; Nc – number of carbon atoms in a contaminant molecule.

The mass concentrations of dioctyl- and dibutyl phthalate calculated with (2) that correspond to 10^{12} atoms/cm^2 are equal to $2.7\cdot10^{-11}$ and $3\cdot10^{-11}$ g/cm^2, respectively. For this reason, the value 10^{-11} g/cm^2 is the required sensitivity level for the present method.

EXPERIMENTAL TECHNIQUE

Experimental research into local tribological surface properties as a function of the concentration of organic contaminants necessitates forming surfaces with varying degrees of contamination, a procedure that consists of three stages.

The first stage consists in cleaning substrate surfaces to the degree of production-grade cleanliness. This is accomplished through rough and final cleaning. Rough cleaning, which serves to remove primary contaminants from the surface, was accomplished with the chemical technique of boiling substrates alternately in alkaline and alcohol solutions such as NaOH and C_3H_8O for ten-minute periods. Final cleaning was accomplished by using Solurus 950, a plasma cleaning system from Gatan, in Ar/O_2 plasma with a gas ratio of 75/25%, respectively, as recommended by the manufacturer. The substrates were irradiated for 4 min at 50 W, the maximal generator power.

The second stage consists in contaminating, by using a special device, the cleaned surfaces with dibutyl-phthalate molecules to the concentration corresponding to the monomolecular level, under the method described in [5].

In the third stage, final plasma cleaning is repeated to adjust the degree of surface cleanliness by changing the irradiation time, ranging from 0 to 4 min in increments of 0.5 min.

The lateral forces of the prepared specimens were then studied in contact mode with Solver PRO-M, a scanning probe microscope from NT-MDT.

Measurements in contact mode are characterized by the high possibility of the probe surface becoming contaminated (Fig. 1a; the contamination is shown with arrows). Because of this, before each measurement took place, the probe was cleaned with Ar/O_2 plasma under the same conditions as those for the substrates. Figure 1b shows the cleaning results. Large contaminant fractions are not observed in the figure, which indicates that the initial surface properties were restored.

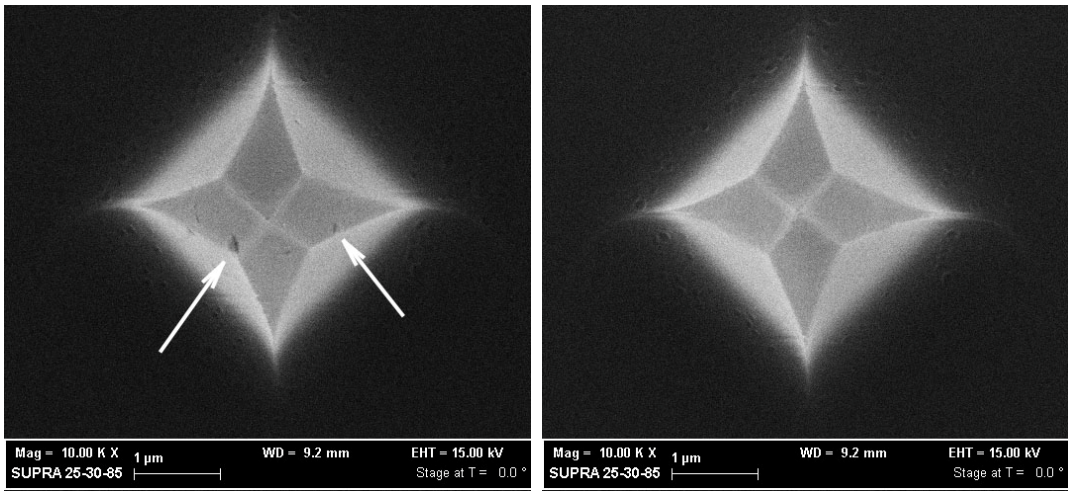

(a) (b)

Figure 1. SEM images of the CSC12 AFM probe: (a) before and (b) after cleaning

The specimens were 1 cm^2 SiO_2 NanoInk wafers used in dip-pen nanolithography. A feature of those wafers is low surface roughness, making it possible to minimize the torsional deflection of the cantilever caused by the local inclination of the surface and thus minimize the error of LF measurement.

RESULTS AND DISCUSSION

Figure 2a shows an AFM image of an LF map obtained by scanning, at a frequency of 0.5 Hz, a 1×1 μm area on the surface of a substrate that has gone through the full cleaning process. The area in the image exhibits a uniform structure and does not have sharply contrasting fragments. But when the scanning frequency was increased to 1 Hz, the LF map developed well-pronounced grains (Fig. 2c) corresponding to roughness protrusions (Fig. 2d). At the same time, the roughness values did not change in relation to the map obtained at 0.5 Hz (Fig. 2b). This rules out differences in the surface structure in different substrate areas.

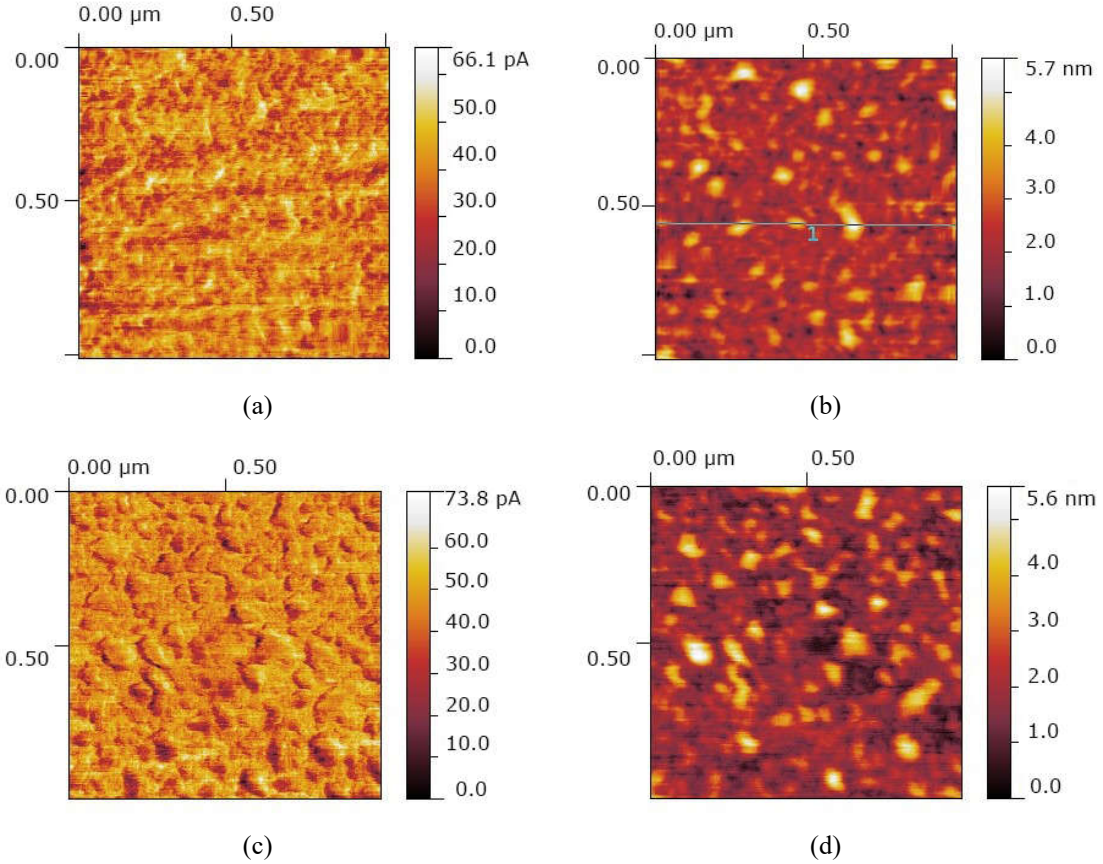

Figure 2. AFM images showing the surface of a cleaned substrate, obtained at 0.5 Hz (*a* shows an LF map and *b*, the surface relief) and 1 Hz (*c* shows an LF map and *d*, the surface relief)

The maximal LF value at 1 Hz (Fig. 2*c*) corresponds to the maximal photodetector current, 73.8 pA, on the gradient scale. Figure 2*c* shows that the value increased by 7.7 pA – about 11% of the initial value – in relation to that in Figure 2*a*. The change cannot be coincidental because scanning takes place in constant-force mode.

Thus, the only possible cause of both the grains and the increase in the torsional deflection of the cantilever when the scanning rate is increased is the action of the capillary forces due to the viscosity of the adsorbed water film; and the homogeneity of the structure confirms indirectly that the surface is clean to a degree conforming to production-grade cleanliness.

Figures 3*a* and 3*b* show AFM images of a substrate surface cleaned with Ar/O_2 plasma for a period of $t = 2.5$ min.

Dark spots on the LF map (Fig. 3*a*) correspond to the minimal torsional deflection of the cantilever for this area of the surface. In this case, the maximal photodetector current corres-

ponding to the maximal cantilever deflection equals 134 pA, a value 2 times higher than the current for the clean surface (Fig. 2*a*). This indicates a 2-fold decrease in the minimal cantilever deflection. The location of dark spots on the LF map corresponds to the regions of the largest heights in the image showing the surface relief (Fig. 3*b*). This presents the conclusion that the dark spots correspond to molecular contaminants that act as a lubricant between the probe and the substrate surface.

When the scanning frequency is increased to 1 Hz (Fig. 3*c*), the range of the registered torsional deflection significantly broadens because of the absence of adsorbed water molecules on the surfaces of molecular-contaminant islets. This causes the color contrast of the image to increase and thus simplifies analyzing the organic-contaminant concentration, which is characterized by the volume of protrusions in the relief images (Fig. 3, *b* and *d*), corresponding to the dark areas on the LF maps. Contaminated regions can be allocated by the threshold principle: the higher the image contrast, the sharper the threshold.

Because a further increase in the scanning frequency does not improve the image contrast significantly but instead increases the wear of the probe, it is inadvisable.

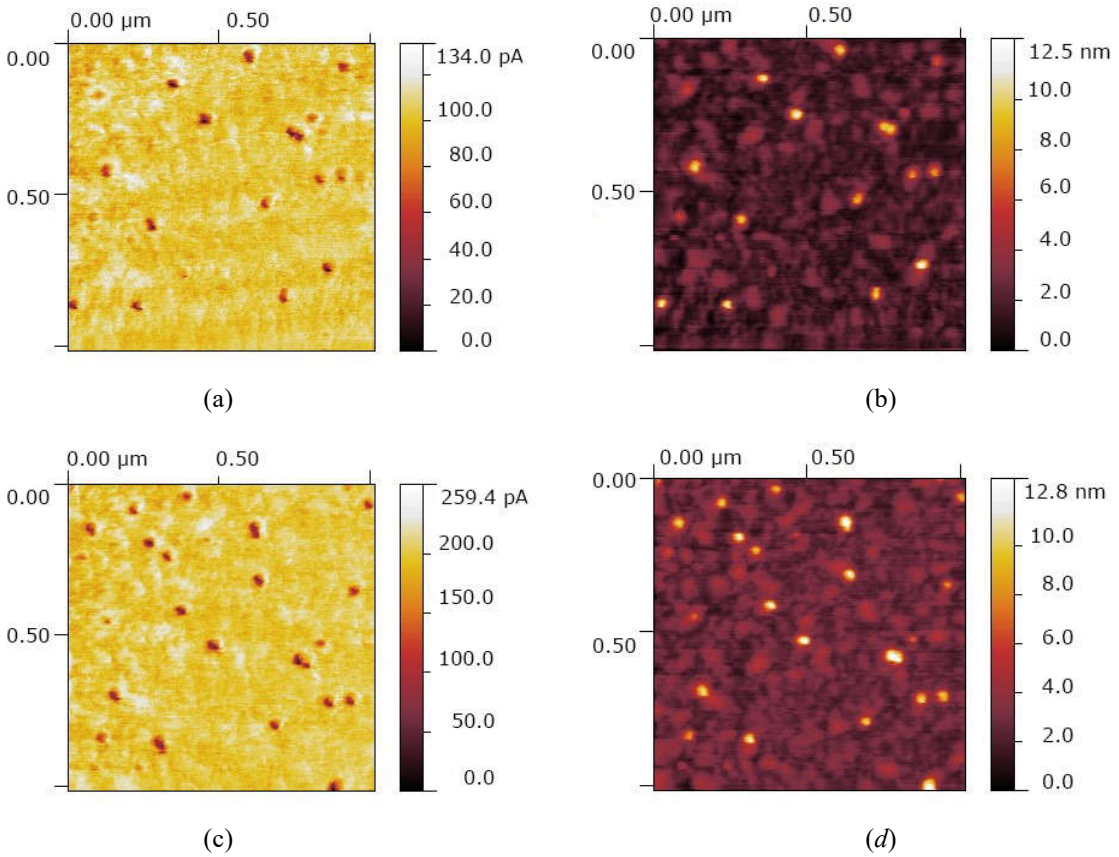

Figure 3. AFM images of contaminated surfaces, obtained at 0.5 Hz (*a* shows an LF map and *b*, the surface relief) and 1 Hz (*c* shows an LF map and *d*, the surface relief)

To determine contaminant concentrations with LF maps, we developed an application program to allocate light spots in relief images so that the spots geometrically correspond to the dark spots on LF maps and to determine the volume of the areas so allocated. To calculate contaminant concentrations, we used the equation:

$$C_a = \frac{\rho V_a}{S}, \qquad (3)$$

where ρ – adsorbate density, and it is equal to 0.982 g/cm^3 for dibutyl phthalate; S – surface area of the measured surface; V_a – volume of the allocated areas.

Figure 4 shows the relationship between the concentration of organic contaminants and the irradiation time. The relationship was obtained with the present method. For each contamination level, concentrations were measured in three surface points, and their averages were recorded on a plot. From the relationship in Figure 4, it follows that the concentration ranges between 10^{-11} and 10^{-8} g/cm^2. Note that the lower limit of this range is determined by the considerable sparsity of contamination observed for this concentration rather than by the sensitivity of the AFM method. The sparsity necessitates increasing both the scanning area and the number of points where the measurement is taken from the surface, and this significantly complicates the measurement process.

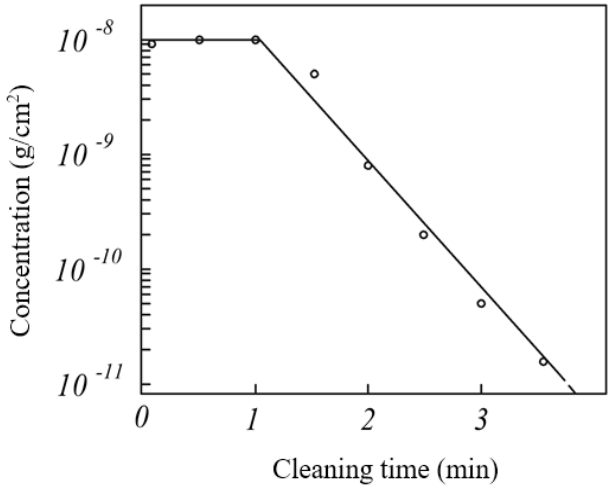

Figure 4. Relationship between the concentration of an organic contaminant and the time of irradiation in Solarus 950, obtained with the present method: the symbol ° denotes experimental values, and the continuous line shows the approximations of experimental data

For a cleaning time ranging from 0 to 1 min, the measured concentration remains constant and equals 10^{-8} g/cm^2. This means that the present method has a low sensitivity when the degree of contamination corresponds to the monomolecular film of the adsrobate. But surfaces with that amount of contamination are not of interest to modern micro- and nanostructuring technology.

CONCLUSION

In this paper, we looked into a method for determining the concentration of organic contaminants on the surfaces of semiconductor and dielectric materials, consisting of two stages. The first stage consists in making maps of lateral forces that act between the probe of the scanning probe microscope and the surface under study as well as in registering the typology of the same surface section. The second stage consists in analyzing both the maps and typology to determine the mass concentration of contaminants.

We have proved experimentally that the optimal frequency for scanning a surface is 1 Hz. Scanning at 1 Hz increases image contrast and facilitates interpreting data. The sensitivity of our method reaches 10^{-11} g/cm^2, a value that meets the modern requirements of micro- and nanostructuring technology.

ACKNOWLEDGMENT

The work was supported by RSF (project No. 18-12-00013).

REFERENCES

1. Rochat, N., Olivier, M., Chabli, A, Conne, F., Lefeuvre, G., & Boll-Burdet, C. (2000). Multiple internal reflection infrared spectroscopy using two-prism coupling geometry: A convenient way for quantitative study of organic contamination on silicon wafers. *Applied Physics Letters, 77*(14), 2249-2251. doi:10.1063/1.1314885
2. New ISO draft standard classifies surface particle cleanliness (2007). *Journal of IEST, 50*(2), 1–4. doi:10.17764/jiet.50.2.d622juj1548x2485
3. Zhang, X., & Chae, J. (2011). A wireless and passive wafer cleanliness monitoring unit via electromagnetic coupling for semiconductor/MEMS manufacturing facilities." *Sensors and Actuators A: Physical, 171*(2), 414–420. doi:10.1016/j.sna.2011.08.005
4. Soifer, V. A., ed. (2003). *Metody komp'yuternoy optiki [Methods of Computer Optics]*. Moscow: Fizmatlit (in Russian).
5. Kazanskiy, N. L., & Kolpakov, V. A. (2009). Microstructuring the surfaces of optical materials with a directed flux of off-electrode plasma: A Monograph. Moscow: Radio and Communications.
6. Goddard, J., Mandal, S., & Erickson, D. (2009). Optically resonant nanophotonic devices for label-free biomolecular detection. In *Advanced Photonic Structures for Biological and Chemical Detection*, 445–470. New York: Springer. doi:10.1007/978-0-387-98063-8
7. Lin, M. C., Wang, M. Q., Lai, J., Huang, R., Weng, C. M., Liao, J. H., Tang, J. S., Weng, C. H., Lu, W., Chen, H. W., & Lee, J. T. C. (2007). Metal hard mask employed Cu/Low *k* film post ash and wet clean process optimization and integration into 65 nm manufacturing flow. *Solid State Phenomena, 134*, 359–362. doi:10.4028/www.scientific.net/SSP.134.359
8. Liu, Y. J., Waugh, D. M., & Yu H. Z. (2002). Impact of organic contamination on the electrical properties of hydrogen-terminated silicon under ambient conditions. *Applied Physics Letters, 81*(26), 4967–4969. doi:10.1063/1.1532758
9. Alberici, S., Dellafiore, A., Manzo, G., Santospirito, G., Villa, C. M., & Zanotti, L. (2004). Organic contamination study for adhesion enhancement between final passivation surface and packaging molding compound. *Microelectronic Engineering, 76*(1–4), 227–234. doi:10.1016/j.mee.2004.07.040
10. Khanna, V. K. (2011). Adhesion–delamination phenomena at the surfaces and interfaces in microelectronics and MEMS structures and packaged devices. *Journal of Physics D: Applied Physics, 44*(3), 1–19. doi:10.1088/0022-3727/44/3/034004
11. Kim, K. S., Kim, J. Y., Kang, H. B., Lee, B. Y., & Park, S. M. (2008). Effects of organic contaminants during metal oxide semiconductor processes. *Journal of the Electrochemical Society, 155*(6), H426–H431. doi:10.1149/1.2904453
12. Guan, J. J., Gale, G. W., & Bennett, J. (2000). Effects of wet chemistry pre-gate clean strategies on the organic contamination of gate oxides for metal-oxide-semiconductor field effect transistor. *Japanese Journal of Applied Physics, 39*(7), 3947–3954. doi:10.1143/JJAP.39.3947
13. Tsai, C. L., Roman, P., Wu, C. T., Pantano, C., Berry, J., Kamieniecki, E., & Ruzyllo, J. (2003). Control of organic contamination of silicon surfaces using white light illumination in ambient air. *Journal of the Electrochemical Society, 150*(1), G39–G44.
14. Saga, K., & Hattori, T. (1996). Identification and removal of trace organic contamination on silicon wafers stored in plastic boxes. *Journal of the Electrochemical Society, 143*(10), 3279–3284. doi:10.1149/1.1837198
15. Reinhardt, K. A., & Kern, W. (2008). *Handbook of silicon wafer cleaning technology*. 2nd ed. Norwich, NY: William Andrew Publishing.
16. Chia, V. K. F. (2010) Process tool cleanliness for clean manufacturing. In *advanced Semiconductor manufacturing conference*, 79–83. IEEE. doi:10.1109/ASMC.2010.5551422

17. Endo, M., Yoshida, H., Maeda, Y., Miyamoto, N., & Niwano, M. (1999). Infrared monitoring system for the detection of organic contamination on a 300 mm Si wafer. *Applied Physics Letters, 75*(4). 519–521. doi:10.1063/1.124434

18. Liu, Y., Wu, T., & Evans, D. F. (1994). Lateral force microscopy study on the shear properties of self-assembled monolayers of dialkylammonium surfactant on mica. *Langmuir, 10*(7), 2241–2245. doi:10.1021/la00019a035

19. Dubravin, A. M., Komkov, O. Yu., & Myshkin, N. K. (2005). Local tribometry with the scanning probe microscope. *Trenie i iznos (Friction and Wear), 26*(3), 269–278.

20. Guo, Y. B., Wang, D. G., & Zhang, S. W. (2011). Adhesion and friction of nanoparticles/polyelectrolyte multilayer films by AFM and micro-tribometer. *Tribology International, 44*(7–8), 906–915. doi:10.1016/j.triboint.2011.03.007

21. Chernyaev, V. N. (1987). *Physical and chemical processes in electronics manufacture*. Moscow: Vysshaya shkola (in Russian).

22. Volkenstein, M. V. (1975). *Molecular biophysics*. Moscow: Nauka (in Russian).

23. Glinka, N. L. (2012). *General chemistry: a textbook*. Moscow: KnoRus (in Russian).

24. Podlipnov, V. V., & Dubovik, A. S. (2012). Matematicheskaya model' pribora kontrolya chistoty poverkhnosti podlozhek po skorosti rastekaniya kapli zhidkosti [A mathematical model for a device for assessing the cleanliness of substrate surfaces by the spread rate of a liquid drop]. *Nauchnoye priborostroyeniye [Scientiific Instrumental Engineering], 22*(2), 74-81 (in Russian).

25. Habuka, H., Naito, T., & Kawahara, N. (2010). Molecular interaction radii and rate constants for clarifying organic compound physisorption on silicon surface. *Journal of the Electrochemical Society, 157*(11), H1014–H1018. doi: 10.1149/1.3489364

Electrical Power Supply System for a Maneuvering System of a Nanosatellite

A. Kumarin, I. Kudryavtsev

Space research department, Samara University, Samara, Russia
E-mail: alky_samara@mail.ru

Received: 28.11.2016

Abstract. Modern CubeSats has become an attractive platform for different types of missions. Some of them involve high peak power consumers. Most of them were originally meant for heavier classes of satellites. Possibility and features of using electrical double layer capacitors (EDLC) in electrical power system for maneuvering system of a nanosatellite are discussed in this paper. Results of calculation of operation are presented. A method of effective charging EDLC in series with switching balancing is described.

Keywords: EDLC, CubeSat, power system, maneuvering system, energy saving

INTRODUCTION

Modern nanosatellite payloads require more and more power to operate. Tasks of space vehicles involve power-consuming systems, some of them originally were not supposed to be used on this class of vehicles. At the same time, the size of modern satellites is limited to several CubeSat units. The CubeSat standard itself defines a row of restrictions in size and mass and development of an appropriate power supply unit becomes a problem. Typical electrical power supply system (EPS) includes solar battery, chemical battery (accumulator) and an electronic control system (CS).

The most used type of batteries are Li-Ion and Li-Polymer. They have some current restrictions, commonly 2C where C denotes the capacitance of a battery in mA*h. For example typical 2 Ah Li-Ion battery might have maximum current I_{max} = 4 A and maximum power P_{max} = 16.8 W. Connecting two batteries in series doubles these values. However, these values do not fulfill the requirements for some specific applications, which in current case is a maneuvering system. It require at least 50 W, however it works for about 10–15 s. Moreover, it has its limits of supply voltage: maximum is 5.5 V. Thus, lowering maximum current by rising supply voltage via connecting multiple cells in series is not an option in this case.

Therefore, the task standing is to find a storage device, capable of delivering high current. There is a type of capacitors known as supercapacitors or ultracapacitors or electric double-layer capacitors (EDLC), which current limit is acceptable for such a task. Their specific energy is lower than Li-Ion batteries can provide, but far greater than ordinary capacitors can. For instance, BCAP350 have been used in this study. Their capacitance is about 350 F, maximum voltage is 2.7 V, ESR is ~3 mOhm and continuous current limit is about 20 A. There-

fore, maximum achievable continuous power is about 54 W/cell, though it cannot be maintained for a long period. Maximum stored energy is about 1.3 kJ. Maximum extractable energy depends on minimum acceptable voltage.

Analysis of scientific activity on this subject shows that several research groups are studying EDLC to use in nanosatellites [1]. However, most scientists are interested in using EDLC in microsatellites. Though these topics seem to be similar, they both have many specific features. Thus, the aim of this study is to find out, whether EDLC are acceptable choice for supplying maneuvering system with particular requirements, marked before.

PROBLEMS USING EDLC

EDLCs main features except high capacitance are low ESR and sensitivity to overvoltage. Allowing voltage to rise beyond 2.8 V will cause dielectric breakdown. On another hand, nearly half of energy is extracted by discharging EDLC from 2.7 to 2 V. Therefore, using just this voltage range will grant an appropriate output voltage range and appropriate energy when connecting two EDLC in series: 4 .. 5.4 V and 1152 J respectively. In addition, this will grant an energy reserve for an emergency case. Thus, the aim of EPS is to charge both capacitors to maximum voltage avoiding overvoltage. Implementation of this is not a trivial task because of the EDLCs' features.

Most common tolerance of component of-the-shelf (COTS) electrolytic capacitors in common and EDLC in particular is –20/+80 %. Therefore, capacitance can be significantly different. Even selection of EDLCs with close values of initial capacitance would not guarantee that they would not become different during operation because of degradation. The difference of capacitances when connecting EDLC in series will cause difference in voltages. Therefore, when one of the capacitors reaches maximum voltage charging must be stopped. However, another capacitor would be undercharged. In the worst case, it would contain only a half of maximum energy. To avoid such situations some kind of balancing method should be applied. The most used method of balancing EDLC is adding resistors in parallel with each cell. However, this method adds wasted power, which should be avoided in space missions. Therefore, an efficient and scalable switching method should be developed.

Thus, the main purpose of the study is to find out whether EDLCs are suitable for supplying a maneuvering system of a nanosatellite and to find a method to efficiently charge them.

MODELLING

Before designing any circuit, a basic modelling is to be done. For that purpose, a simulating program has been created, capable of modeling different scenarios. EDLCs operate just like ordinary capacitors if the voltage changes slowly [2], which is the case all the time except the beginning/ending of charging/discharging process. In addition, schematic of [2] can be simplified to one capacitance and one resistance in series due low actual value of ESR. Therefore, a formula can be defined for EDLC voltage from basic considerations:

$$U(t+dt) = U(t) + \left(\frac{I}{C} - \frac{P_L}{CU(t)} \right) dt,$$

where C – capacitance, P_L – leak power, I – input current.

Here leaks are represented as a static power, which depends on cell voltage. As this relation between leak power and cell voltage is not provided by EDLC manufacturer's datasheet,

it has to be measured. Therefore, an experiment has been conducted. The target EDLC was charged and disconnected from any circuits except high impedance measurement system to avoid leaks through them. P-V diagrams represent analysis of experiment data for BCAP350 (Figure 1b). For a comparison same data is presented for EECHW0D226 (Figure 1a) – an elder model of EDLC with lesser capacitance – 22 F. In both cases relation can be approximated as exponential.

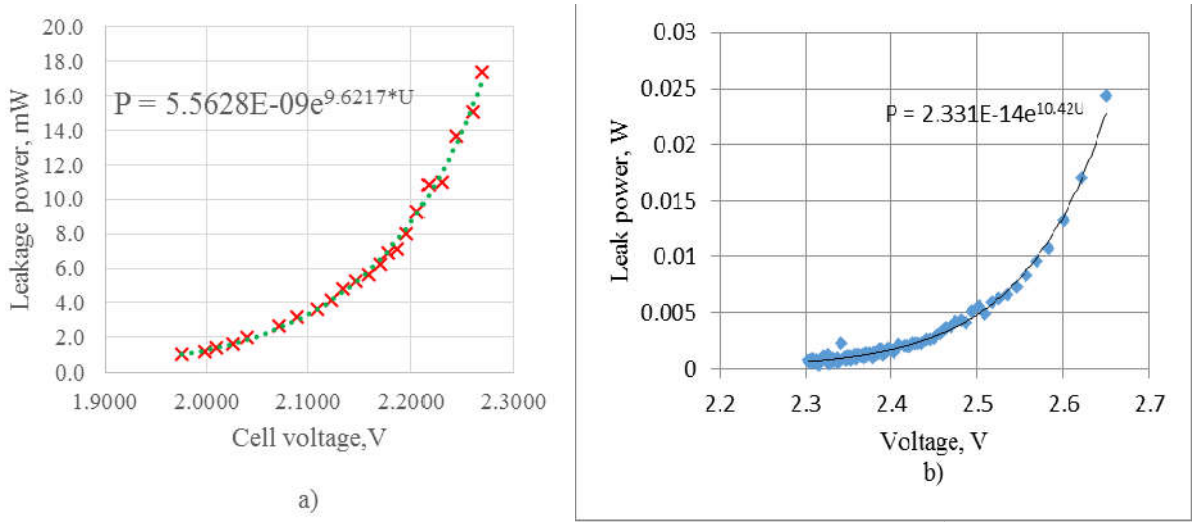

Figure 1. Leak power vs. cell voltage (a) EECHW0D226, (b) BCAP350

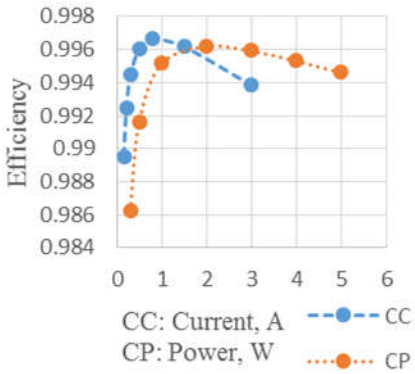

Figure 2. Charging EDLC

Using this data an operation calculation can be made for a single EDLC. First, diagrams on Figure 2 represent charging efficiency of constant current (CC) and constant power (CP) charging methods vs. the values of current and power respectively. Clearly, a wide range of currents or powers can be used to charge EDLC with charge times from 3 to 45 minutes. In addition, some special methods can be created to ensure even more fast/efficient charging if needed. However, keeping EDLC with high voltage will lead to waste of energy trough leaks. Therefore, starting time and intensity of charging is to be chosen from the considered usage time.

Similarly discharging process can be calculated. The efficiency exceeds 97% even at 15s working at resistive load with 50 W peak power, which is twice as high as the considered value. The main source of energy losses at discharging is EDLC's ESR. However, its value is ~3 mOhm, which is much less than most switches. In addition, the resistance of contacts and wires can be even greater. Therefore, ESR can be ignored for considered powers. That combined with high continuous current is a great advantage against Li-Ion, which ESR is significantly higher (about 0.2–0.5 Ohm). In addition, EDLC's cycle life is about 1 million, which is significantly greater than any rechargeable battery can provide.

Thus, the efficiency of EDLC itself exceeds 95 %. Therefore, the efficiency of EPS will mostly depend on the effectiveness of hardware implementation of charging and switching circuit.

CHARGING THE EDLC

To charge an EDLC the main EPS's battery is used as the power source (PWR). Therefore, the voltage is nominally 7.4 or 14.8 V. If charging takes place only during lighted orbit time, the main battery is not affected, the entire load is on battery charger. Since the voltage of EDLC can vary from nearly zero at the very first charge to 2.7 V for a cell, the only option is to regulate charging current. However, for space applications basic linear regulators are not suitable because of their high power dissipation. Moreover, most switching-type current source ICs, which are mostly used in LED lamps, are not suited either. This is because of their internal switching devices – Darlington transistors. Since these transistors are bipolar, their significant voltage drop makes them ineffective. Therefore, an effective step-down (buck) DC-DC voltage regulator should be applied. Effectiveness is provided by low open channel resistance MOSFET-transistor as switches. A transistor also replaces diode in buck circuit. En example of such a solution is LM46000 integrated circuit (IC) [3]. An adjustment should be made to the feedback system to make voltage regulator regulate current. Figure 3 shows a feedback schematic of the charger. An external analog signal (EXT_SIG) is added to make an opportunity to change current limit. The current is measured by measuring amplified voltage on shunt resistor Rsh.

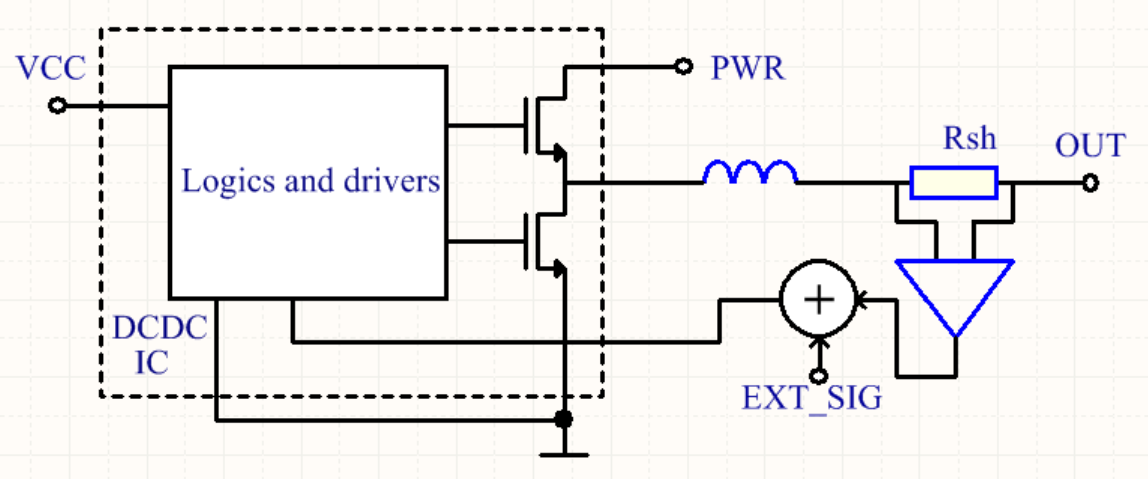

Figure 3. Feedback schematic for charger

Charging EDLC in series is another problem. As was stated before, voltage can differ for different cells [4]. Therefore, a special switching schematic has been designed for temporary switching off some of the cells. Figure 4 shows a two-cell (C1, C2) version of the schematic. The main principle is to bypass a cell, which voltage is significantly higher than others' are using SW1 and SW3. However, the bypassing method should not discharge the cell. Therefore, some device should be used to prevent current to flow in discharge direction. For a point between cells (middle point), SW2 must be used, because reverse current is to be when discharging to a load. For the top cell, a simple Schottky diode (D1) can be used. Since the charging current is considered low, this diode would have

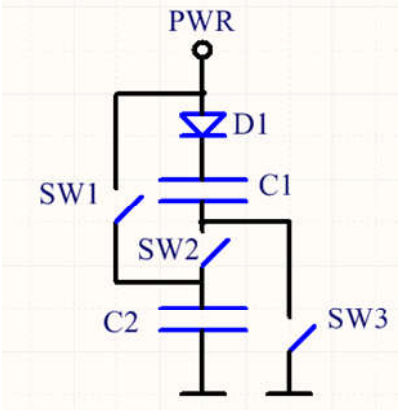

Figure 4. Series balancing schematic

acceptable power dissipation. For high charging current, the method would be the same as for a middle point.

Implementation of this schematic uses low open-channel resistance n-MOSFET transistors. Therefore, power dissipation is low. The problem is to drive a transistor with source tied to an EDLC. Since gate voltage is related to source, a higher voltage related to ground is needed to open the transistor. Therefore, there should be a voltage source capable of driving the gate of the highest transistor. For example, IRF7832 will require 3 V above the maximum output. Since the main battery's voltage is 14.8 V, it is possible to connect up to four cells without any external voltage source. In that case, the maximum output would be 10.8 V. That is suitable for current and most of future versions of the maneuvering system.

DISCUSSION

The main aim of the study was to find out, whether EDLCs are suitable power source for supplying a maneuvering system of a nanosatellite and find a way to charge them effectively. The first criteria is mass and volume. A single cell of BCAP350 has mass about 60 g, 61.5 mm length and 33.3 mm diameter. Therefore, two cells require more volume than main batteries. However, since the maneuvering system itself fills 1U of CubeSat standard, that is suitable.

The modelling based on experimental data showed, that the efficiency of an EDLC itself in charging and discharging processes is about 95 % in extreme power operation. That is achieved because of low ESR, which mostly affects the performance during discharging, and relatively short time of charging, when the leakage effect prevails. This results combined with environmental tests [5] signify that EDLC should be suitable for an electrical power system for a maneuvering system.

A charging scheme has been made for EDLC. Since it is a switching current regulator with an external control option, almost any charging profile can be achieved. An implementation circuit determines the efficiency of charging. Choosing an IC with low open-channel resistance MOSFET switch, for example − LM46000, will guarantee performance greater than 90 %.

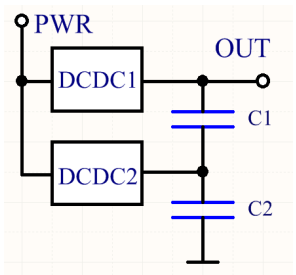

Figure 5. Alternative charging schematic

A balancing has been developed for proper charging several EDLCs in series. It seems a simple and efficient solution. Its main advantages are relatively simple circuit, scalability, low power dissipation. The disadvantages are impossibility of balancing if discharging, additional components are required to prevent short circuit in case of program error, and the switches require higher voltage to open.

Figure 5 shows an alternative balancing schematic for a comparison. Similar schemes are used in chemical batteries chargers. DCDC converters can be applied like shown or connected in series. The advantages of such scheme comparing to previous are possibility to balance cells in use, no additional ESR. The main disadvantages are the complexity of the circuit and bad scalability. The benefits do not seem to compensate the additional problems. Therefore, the first scheme seem to be the most suitable. Therefore, a suitable charging method seems to be found.

The results of this paper are to be used to design an implementation of an EPS for a maneuvering system of a nanosatellite. In addition, some of the results might be interesting for designers of EPS for a nanosatellite. Since the balancing schematic is scalable, it is possible to use more cells in series to obtain higher maximum voltage, e.g. 5.4 V, 8.1 V, 10.8 V with 2, 3, 4 cells respectively. A lower capacitance can be used to reduce mass and volume in satellites,

where less energy is needed. Finally, the results of this study are not limited to space applications. They can be used in any energy harvesting system for prolonging cycle life.

REFERENCES

1. Alkali, M., Edres, M., Khan, A., Masui, H., & Cho, M. (2015). Preliminary study of electric double layer capacitor as an energy storage of simple nanosatellite power system. *65th International Astronautical Congress, Toronto, Canada.*
2. Kang, J., Wen, J., Jayaram, S.H., Yu, A., & Wang, X. (2014). Development of an equivalent circuit model for electrochemical double layer capacitors (EDLCs) with distinct electrolytes. *Electrochimica Acta, 115*, 587–598. doi:10.1016/j.electacta.2013.11.002
3. SNVSA45A–JUNE 2014. *LM46000 simple switcher technical datasheet.* Texas Instruments.
4. Ionescu, C., Vasile, A., & Negroiu, R. (2016). Investigations on balancing circuits for supercapacitor modules. *39th International Spring Seminar on Electronics Technology (ISSE)*, Pilsen, 2016, 521–526. doi:10.1109/ISSE.2016.7563253
5. Alkali, M., Edres, M., Khan, A., Masui, H., & Cho, M. (2015). Environment test campaign of a commercial-off-the-shelf electrical double layer capacitor for space use. *34th ISAS/JAXA Space Power Symposium*, 6th March, 2015, Institute of Space and Astronautical Science (ISAS) / Japan Aerospace Exploration Agency (JAXA), Sagamihara, Japan.

Generator of Powerful Current Pulses for Electrostimulated Metal Processing

V. A. Kuznetsov, V. E. Gromov, E. S. Kuznetsova, A. Yu. Gagarin, D. A. Kosinov, K. V. Aksenova, A. P. Semin

Siberian State Industrial University, Novokuznetsk, Russia
E-mail: gromov@physics.sibsiu.ru

Received: 23.11.2016

Abstract. The description of the powerful generator of unipolar pulses having the charger connected to power capacitors and the thyristor switch, discharging the capacitors to the low ohm load is presented. In order to reduce the main power, the charge exchange device on the base of thyristor connected antiparallelly in thyristor switch is introduced in the scheme. To realize the possibility of pulse amplitude control and increase in its capacity two irreversible thyristor transformers are used in charger instead of an unregulated direct current source. These thyristor transformers are switched on in series and in unidirectional way. They permit to obtain the regulated voltage at power capacitors. In order to optimize the capacitor charging process a two-circuit system of subordinate regulation of pulse generator parameters with external voltage control circuit and internal control – current capacitor charge. The model of the suggested generator is implemented in the "Matlab, Simulink" medium. The model is adequate to the real pulse generator used in SibSIU for investigation of electrostimulated plastic deformation of metals and alloys. The developed model permitted to improve the technical parameters and device operation regimes. The considerable mains power decreases as well as possibility of capacitor charge voltage control up to 600 V in the range of pulse repetition frequency 400 Hz are the advantages of updated generator in comparison with the analogues. The generator can be used in industry, in particular, rolling production for hard deformed steel wire drawing.

Keywords: pulse generator, charger, recharging device, current pulse, mathematical modeling, transient processes

INTRODUCTION

The interest to the investigation of peculiarities of pulse electric current (PEC) effect of high density on the behavior and properties of metallic materials is dictated by the prospects of their application in technology of metal-working [1, 2]. The effect of electric current pulses manifests itself at different structural levels and due to its diversity, versatility and unique possibilities can be used for modification of physico-mechanical properties, stimulation of relaxation processes and reduction of residual stresses in elements of structures.

For the first time the effect of electron action (electroplastic effect – EPE) on the process of metal deformation was experimentally studied and described in the research [3].

Intensive works in this direction have been carried out for more than 50 years, but there is no consensus of opinion among the researchers as to the nature of the discovered EPE [4–8].

In spite of the large number of experimental and theoretical investigations in the given direction, in connection with the deficient definiteness of physical mechanisms of action of PEC on metallic materials as well as the existing disagreement in interpretations of microscopic effects the further investigation of PEC effect on metals and alloys remains the topical and important scientific and practical task.

The solution of the problems of investigation of the developed electrostimulated deformation mechanisms and its practical application in plastic metal working is possible when using the sources of powerful short current pulses [9, 10]. Such sources whose principle of action consists in the discharge of prior charged capacitors to the low ohm load are also used in studying the changes in physical properties of metals under current effect [11]. The disadvantages of the generator preventing it from wide application in industry are:

– low efficiency and substantial energy expenditures of the charging unit in relation to the availability of the charge of capacitors of current-limiting resistance R_z in the circuit;

– impossibility of regulating the amplitude of power pulse.

The purpose of the research is development of circuit elements of generator of powerful current pulses eliminating these disadvantages contributing to the reduction in main power and introduction of generator in industry in plastic metal working.

THE RESULTS OF THE RESEARCH AND DISCUSSION

Figure 1 shows the oscillogram of transient processes of pulse current, the charging current of power capacitors and power capacitors' voltage. After the pulse passage the *C Br1* capacitor voltage takes the negative value ($-U_{z1}$), equal (0.85–0.95) to the initial voltage value U_z. The capacitor charge exchange from ($-U_{z1}$) to U_z occurs from the d.c. source with mains power consumption 3·380 V.

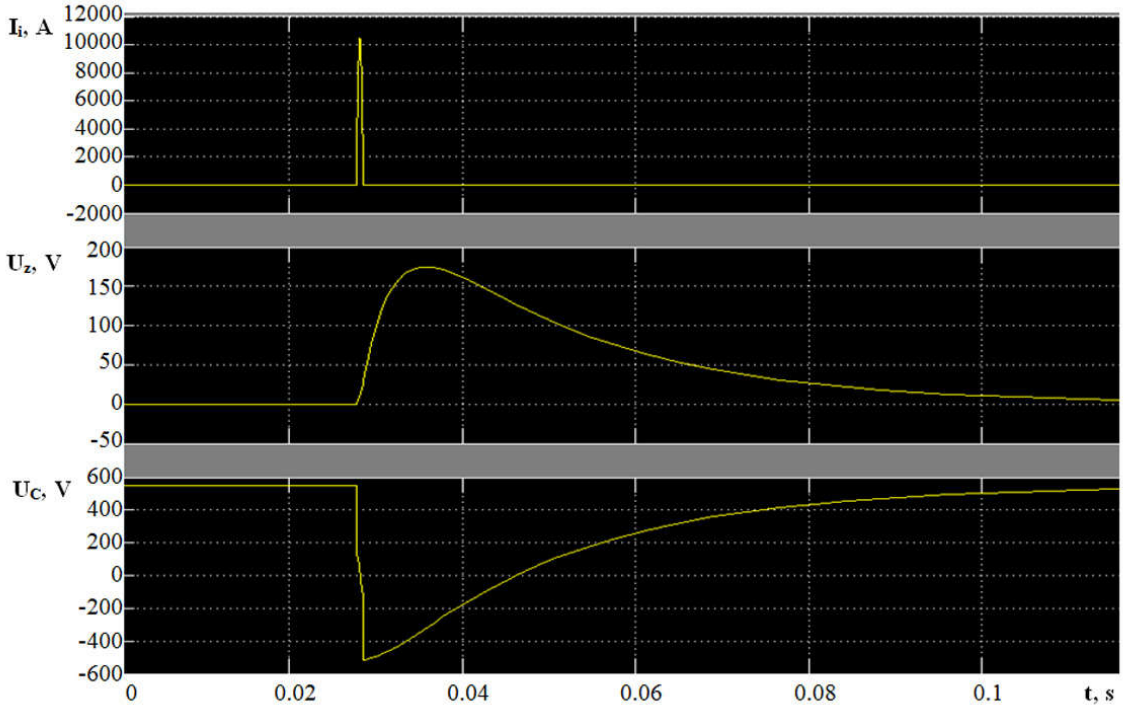

Figure 1. Oscillogram of transient processes of powerful pulse generator
(I_i – pulse current, U_z – charge voltage, U_C – capacitor voltage)

To limit the current rush between the rectifier bridge of the charger and power capacitors the current limiting resistance R_z where the considerable power (30 kW at pulse repetition frequency 100 Hz) dissipates is installed.

In order to decrease the main power the recharging unit *UP* consisting of current limiting inductance *RL Br4* connected in series and thyristor *Th1* connected in antiparallel with thyristor *Th* is introduced in the pulse generator circuit.

At the moment of time when after passage power pulse the current becomes equal to zero, the pulses of different polarity the value of which is proportional to the derivative value of power pulse *dI/dt* are formed in the instrument transformer *Three*. Diode *D* blocks the negative half-wave, and the positive signal is amplified to the required value and is fed to the control electrode of thyristor *Th1*. The latter switches on and capacitors *C Br1* recharge trough the circuit "thyristor *Th1*, inductance *RL Br4*" to the positive voltage value 0.8–0.9 U_z. In this case the charge unit carries out only the milking of capacitors from U_z. Thus, the application of recharge unit decreases the main power considerably.

The transient processes of current pulse and recharge voltage with application of thyristor *Th1* are shown in Fig. 2. For further decrease in charge unit power and possibility of adjusting the charge voltage value (pulse amplitude) the controlled thyristor transformers *Uni Br*, *Uni Br 1* connected in series, in this case one of the transformer is fed from transformer winding *Tr* connected in 'star' circuit and the other – in 'triangle' circuit are introduced in the circuit instead of non-controlled diode rectifier. Such an interconnection circuit firstly, increases the rectified voltage (value of power pulse, respectively) and secondly, decreases the transformer inertia (the pulses number m increase to 12 at the period of feeding voltage, and pulse duration decreases to 1.6 ms). When using the power supply mentioned above the generator is capable of generating the pulse with maximum repetition frequency to 400 Hz. The application of thyristor transformers permitted to remove the current-limiting resistor R_z from the circuit of charge unit and it also increased the efficiency and decreased the a.c. main power.

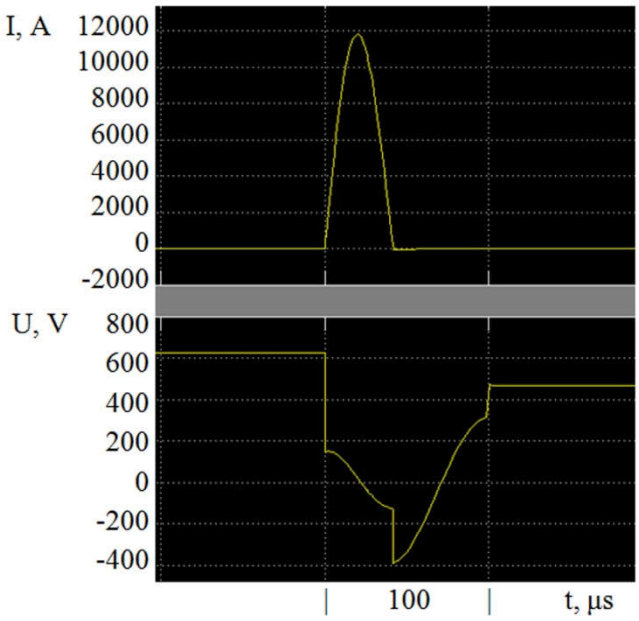

Figure 2. Parameters of capacitors' current pulse and voltage with recharge unit

For controlling the pulse amplitude value a two-circuit system of voltage adjustment is implemented (SVA). The internal circuit of automatic control system is organized like circuit of controlling the current of capacitors' charge and the external circuit – controlling the voltage of capacitors' charge. The circuit of current control consists of current regulator *G1* with block of limitation *S1*, thyristor transformers *Uni Br, Uni Br 1* consisting of inertia links with fast time constant 4 ms and object of control – power capacitors *C Br1*. The additional inductance *LBr3* is introduced into the circuit for stable operation. The active resistors of thyristor transformers and buses as well as power capacitor inductance are taken into account in power capacitor block *C Br1*. The negative current feedback is removed from the shunt *CM1* and is amplified by fast-responding amplifier *Tfcn*. The control circuit of capacitors' charge voltage consists of voltage regulator *G3* and optimized current circuit. The voltage feedback consists of divider and inertialess voltage gauge *Tfcn1*. The limitation of maximum charge current is done at the expense of voltage regulator limitation block *S2*. This block enables to limit the minimum and maximum angular value of thyristor transformer control. The voltage adjustment may be done either by hand or from the signal of technological programmed controller.

If it is necessary to reduce voltage very quickly the control system forms the assignment to the negative value of 'charge' current – discharge current. However, in connection with the fact that thyristor transformers are non-reversible they can reduce current only up to zero value. In this case, the reduction of capacitor voltage occurs strictly at the expense of active losses and has a long character. To increase the speed of system response the device blocking the operation of recharge device by blocking the control pulses to thyristor *Th1* for the time necessary to reduce the capacitor voltage is connected into the circuit. The blocking device contains the amplifier *G2* with block of limitation *S4*. At the negative current assignment the device forms the signal blocking the operation of *G* in the system of formation of control pulses to thyristor *Th1* of recharge.

Figure 3 shows the mathematical model of the updated generator made in medium "MatLab, Simulink" with recharger, controlled thyristor charger and SVA, and Figure 4 – oscillograms of transient processes in operation of the updated generator in the regime of stepwise change of voltage assignment to 600 V. The main power of upgraded generator in static regime at pulse repetition frequency 100 Hz reduced 5-fold (from 30 to 5.5 kW).

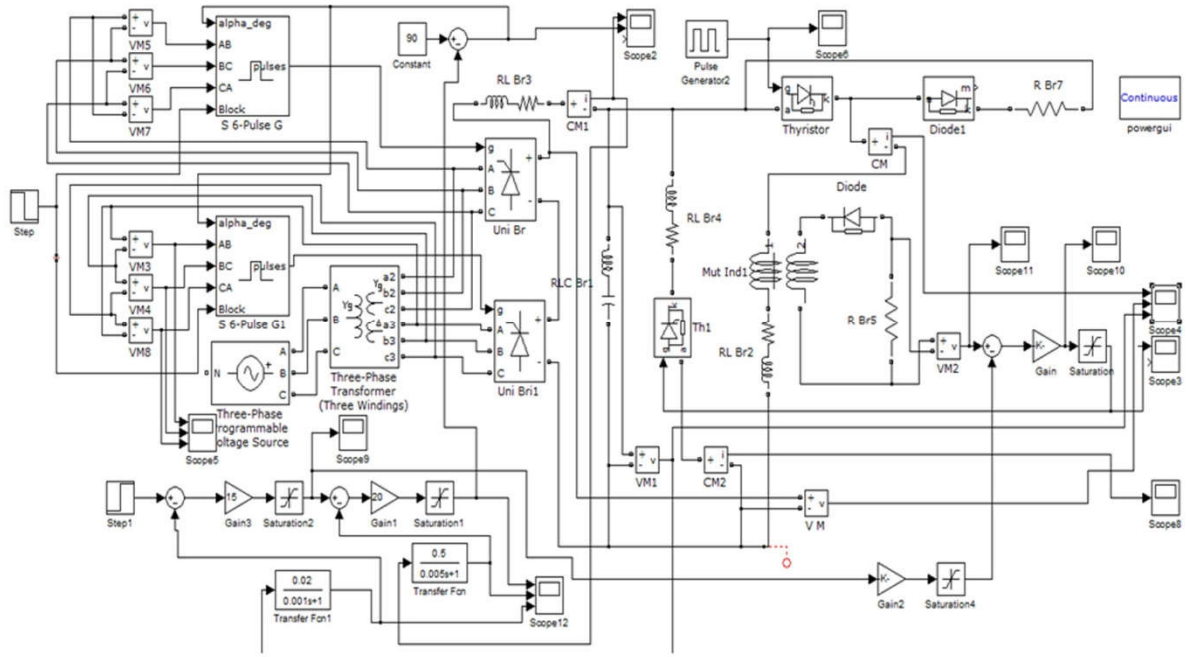

Figure 3. Simulation model of the modernized generator

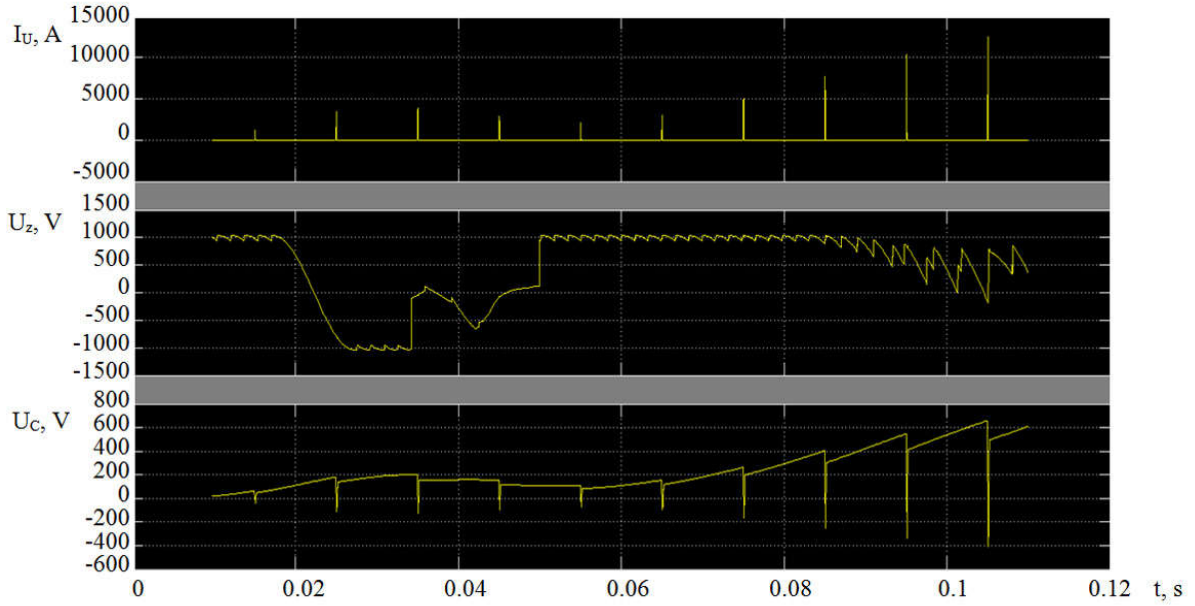

Figure 4. Transient processes in stepwise change of voltage adjustment of capacitors charge (I_u – pulse current, U_z – charge voltage, U_C – capacitor voltage)

CONCLUSION

1. The introduction of recharger and block of thyristor convertors connected in series in the circuit of pulse generator enabled to reduce the main power as well as to control smoothly the amplitude of power pulse with high speed response (not less than 50 ms) and wide control range (up to 600 V). It widens considerably the possibilities of the device application in industry.

2. The built model is adequate to the real unit which made it possible to use it for parameter refinement of the used elements and the system of obeyed control with the purpose of optimization of operation regimes (transient processes, in particular) and the increase in operational reliability.

ACKNOWLEDGMENT

The research is done at the expense of grants of RFFI (№16-32-60048 mol_a_dk).

REFERENCES

1. Stepanov, G. V., & Babutsky, A. I. (2014). *Effect of pulsed electric current of high density on strength metallic materials and the stressed-strained state of structure elements.* Kiev: Naukova dumka.
2. Strizhalo, V. A., Novogrudskiy, L. S., & Vorob'ev, E. V. (2008). *The strength of materials at cryogenic temperatures, taking into account the effects of electromagnetic fields.* Kiev: G.S. Pisarenko Institute of problem of strength NAN Ukraine.
3. Troitsky, O. A., & Likhtman, V. I. (1963). On anisotropy of electron and α-irradiation effect on deformation process of zinc monocrystals in brittle state. *Reports of the Academy of Sciences of the USSR. Technical Physics, 148*(2), 332–334.
4. Okazaki, K., Kagawa, M., & Conrad, H. (1978). A study of the electroplastic effect in metals. *Scripta Metallurgica, 12*(11), 1063–1068.
5. Okazaki, K., Kagawa, M., & Conrad, H. (1979). A study of the electroplastic effect in metals. *Scripta Metallurgica, 13*(4), 277–280.
6. Stepanov, G., Babutsky, A., & Krushka, L. (2003). Metals behavior under passage of impulse electric current. *J. Phys. IV France, 110*, 577–582.
7. Sprecher, A.F., Mannan, S.L., & Conrad, H. (1986). On mechanisms for the electroplastic effect in metals. *Acta Metallurgica, 34*(7), 1145–1162.
8. Stepanov, G. V., & Babutsky, A. I. (2006). Analysis of the effect of pulsed electric current of high density on the rate of plastic deformation of metals. *Problemy prochnosti [Problems of Strength], 2*, 105–113.
9. Beklemishev, N. N. (1984). Installation for the study of the deformation of the conductive material to the action of a high current density. *Zavodskaya laboratoriya [Factory Laboratory], 50*(9), 82–84.
10. Kuznetsov, V. A., & Gromov, V. E. (1986). Economical thyristor generator of powerful current pulses. *Izvestiya vuzov. Elektromechanics [Proceedings of the universities. Electromechanics], 6*, 122–124.
11. Zhmakin, Yu. D., Romanov, D. A., & Rybyanets, V. A. (2012). Economical means of energy consumption regulation with application of powerful current pulse generator. *Promyshlennaya energetika [Industrial power], 4*, 14–16.

Technique of Cluster Analysis Application in Semiconductor Elements Classification for Improving Product Quality and Reliability

R. O. Mishanov

Department of Design and Technology of Electronic Systems and Devices,
Samara National Research University named after academician S. P. Korolev (Samara University),
Samara, Russian Federation
E-mail: mishanov91@bk.ru

Received: 14.11.2016

Abstract. The text deals with the information about application of cluster analysis for the purpose of semiconductor elements classification. The technique of semiconductor elements classification on groups based on application of k-means clustering is offered. Using the offered technique the research of CMOS chips selection was conducted. A time delay on the leading edge of the signal and a critical voltage supply were used as informative parameters of the chips. The recommendations about application of this technique in case of large number of informative parameters are offered.

Keywords: cluster analysis, k-means clustering, cluster group, informative parameter, Euclidean distance, dendrogram

INTRODUCTION

Nowadays a problem of improving quality and reliability of the electronic devices relates to the priority areas of the technological development. The most actual aspect is looking for ways to improve quality of the electronic components to achieve an acceptable level of product reliability with minimum time and resource spends.

Predicting reliability is constantly being studied and widely distributed in electronics. At the same time, the main attention is paid to the analysis of elements failures, physics of failures application in electronics and statistical failure data. In [1] there is the information about multi-state and continuous-state system reliability with degradation analysis, maintenance models for large repairable systems. Authors [2] present the results of reliability analysis of MOS chips, bipolar transistors and diodes in stationary and mobile systems. At the same time, methods of predicting failures of complex systems are being developed. Authors [3] describe program HIRAP Honeywell (Honeywell In-Service Reliability Assessment Program), which takes into account design failure rates, manufacturing process failure rates and other causes for equipment removal.

A large number of works are devoted to the development of techniques for applying mathematical methods and finding forecasting models. The use of these methods is justified in terms of financial and labor costs to ensure the forecasting process, as well as in terms of the

results, that satisfy manufacturers and consumers. Statistical forecasting methods allow obtaining acceptable accuracy of short and medium-term forecasts. By use of statistical methods the long-term forecast accuracy, which satisfy the developers, is difficult to be obtained due to the necessity of large bulk of data processing, which entails the use of many resources. Also, there is no necessity in obtaining long-term forecasts because in many cases the operating term less than the forecast time. Authors [4] offer Monte Carlo simulation using "Excel" spreadsheet for forecasting reliability of a complex system.

The application of the theory of pattern recognition is of special interest. Authors [5] describe the developed system of principles and criteria of determining the relationship of a specified electronic product with one of the preliminary identified product classes. Authors [6] offer the forecasting models for the samples of CMOS chips and Zener diode by an extrapolation method. Thus, research into the application of the theory of pattern recognition to predict the reliability of electronic devices is relevant at this stage in the development of science and technology.

The cluster analysis is related to the theory of pattern recognition. Cluster analysis is a system of data processing algorithms for the distribution of the objects in the group of clusters (cluster groups), which are instantiated by homogeneous objects.

Use of cluster analysis in the practical solution of data analysis problems is often characterized by a known beforehand number of cluster groups. In this case, k-means clustering method got widespread. It involves a construction of k different cluster groups, which are located at the greatest possible distance from one another. Initially k randomly selected cluster groups are formed, then each object belonging to each group is examined. The criterion for such relationship is to minimize the variability within the cluster and to maximize variability between clusters.

This paper offers the technique of the microchips classification based on the k-means clustering method. The technique is comprised of 3 steps:

– Step 1. Analysis of the initial data. Measurement scale settings. Justification and a choice of proximity measures.

– Step 2. Conducting cluster analysis using method of hierarchical classification. Dendrogram analysis and clusters quantification.

– Step 3. Conducting cluster analysis by k-means clustering. Analysis of the results.

INITIAL DATA

CMOS chips 765LN2 sample was investigated. The integrated circuits are represented by six logic elements NAND. The sample includes 50 chips. Time delay on the leading edge of the signal x_1 (t^+_p, μs) and critical voltage supply x_2 (V_{sc}, V) are selected as the informative parameters. Table 1 presents the initial data for cluster analysis.

PROBLEM FORMULATION

The research objective is to split elements into cluster groups (classes). The elements in one group are characterized by a similar condition.

PROBLEM SOLUTION

Task solution by the cluster analysis performed using the program package STATISTICA 10.

The first step of the solution is to set a measurement scale, as cluster groups are characterized by assessing the distance between elements. But as the measurement scale of values x_1 and x_2 is different (x_1 is measured in microseconds, x_2 – in volts), the parameter values must be centered, i.e. lead to the scale when average value of the parameters equals 0 and standard deviation equals 1.

Table 1. The initial data for cluster analysis

The element number	X_1	X_2	The element number	X_1	X_2	The element number	X_1	X_2
1	4.30	1.30	19	3.80	1.20	37	3.80	1.40
2	7.20	2.90	20	3.70	1.20	38	6.40	2.50
3	3.20	1.10	21	4.40	1.30	39	6.00	2.50
4	6.60	2.10	22	7.10	2.60	40	6.90	2.81
5	5.30	1.72	23	5.10	1.60	41	7.10	1.74
6	4.70	1.60	24	5.00	1.50	42	5.00	1.72
7	6.70	1.80	25	15.60	3.50	43	7.30	2.90
8	6.20	1.73	26	5.00	2.80	44	8.10	2.80
9	6.60	2.40	27	4.40	1.71	45	5.20	2.30
10	3.90	1.30	28	4.50	1.80	46	7.10	2.81
11	4.50	1.40	29	3.00	1.00	47	10.80	3.20
12	4.30	1.40	30	4.20	1.56	48	3.50	1.50
13	4.60	1.50	31	4.90	1.60	49	4.00	1.63
14	5.80	1.70	32	7.50	2.80	50	5.10	1.90
15	9.20	2.90	33	4.50	1.62			
16	6.50	2.60	34	7.80	2.78			
17	7.00	2.80	35	8.90	2.96			
18	5.20	1.75	36	4.80	1.70			

Cluster analysis involves the use one of the ways to determine the proximity measure, the use of which depends on the final version of the partition of objects into clusters. Selection of the proximity measure depends on the research objectives, the nature of the probability distribution and other parameters. In this example, the ordinary Euclidean Distance is used as the proximity measure, because a sample is taken from a population with normal distribution, and informative parameters x_1 and x_2 are equally important for the classification.

Centered values of the informative parameters are shown in Table 2. Rounding made to the third decimal place.

The Euclidean Distance is calculated for each pair of elements by the formula:

$$\rho_E(a_i, a_j) = \sqrt{(x_{1ci} - x_{1cj})^2 + (x_{2ci} - x_{2cj})^2}, \quad (1)$$

where a_i and a_j – the ith and jth elements of the sample; x_{1ci} and x_{1cj} – centered characteristic value of parameter x_1 of the ith and jth elements of the sample; x_{2ci} and x_{2cj} – centered characteristic value of parameter x_2 of the ith and jth elements of the sample.

In the program package STATISTICA a cluster analysis using the hierarchical classification was selected, the rule of association "total communication method" was noted, the "Euclidean distance" was selected as a measure of proximity. The results of hierarchical classification are shown in Fig. 1. The vertical dendrogram of the cluster analysis using hierarchical classification is shown in Fig. 2.

Table 2. Centered values of the informative parameters

The element number	X_{1c}	X_{2c}	The element number	X_{1c}	X_{2c}	The element number	X_{1c}	X_{2c}
1	– 0.709	– 1.097	19	– 0.938	– 1.249	37	– 0.938	– 0.944
2	0.621	1.345	20	– 0.984	– 1.249	38	0.254	0.734
3	– 1.214	– 1.402	21	– 0.663	– 1.097	39	0.071	0.734
4	0.346	0.124	22	0.575	0.887	40	0.483	1.207
5	– 0.250	– 0.456	23	– 0.342	– 0.639	41	0.575	– 0.425
6	– 0.526	– 0.639	24	– 0.388	– 0.792	42	– 0.388	– 0.456
7	0.392	– 0.334	25	4.474	2.260	43	0.667	1.345
8	0.162	– 0.441	26	– 0.388	1.192	44	1.034	1.192
9	0.346	0.582	27	– 0.663	– 0.471	45	– 0.296	0.429
10	– 0.893	– 1.097	28	– 0.617	– 0.334	46	0.575	1.207
11	– 0.617	– 0.944	29	– 1.305	– 1.555	47	2.272	1.802
12	– 0.709	– 0.944	30	– 0.755	– 0.700	48	– 1.076	– 0.792
13	– 0.572	– 0.792	31	– 0.434	– 0.639	49	– 0.847	– 0.593
14	– 0.021	– 0.486	32	0.759	1.192	50	– 0.342	– 0.181
15	1.538	1.345	33	– 0.617	– 0.609			
16	0.300	0.887	34	0.896	1.162			
17	0.529	1.192	35	1.401	1.436			
18	– 0.296	– 0.410	36	– 0.480	– 0.486			

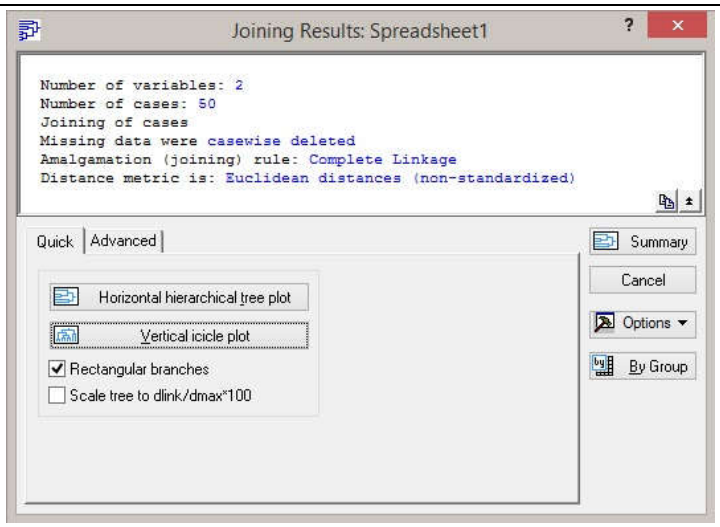

Figure 1. The results of hierarchical classification of clustering analysis

The meaning of the vertical dendrogram is as follows. The shorter a distance between the elements, the more similar in informative parameters they are, therefore they belong to the same cluster. With increasing a distance between the elements the differences become larger. Each node of the dendrogram indicates the union of two or more clusters. The distance, at which the clusters are combined, is indicated on the vertical axis. The horizontal axis shows the number of elements.

Analysis of the dendrogram demonstrates that on a distance of 6.924 the element No.25 combined with a large cluster, which is formed on a distance of 4.9065. It can be concluded that the optimal number of clusters is 2, one of which is formed on a distance of 2.9142, and the second - on a distance of 2.3456. The element No.25 can be considered as the outlier.

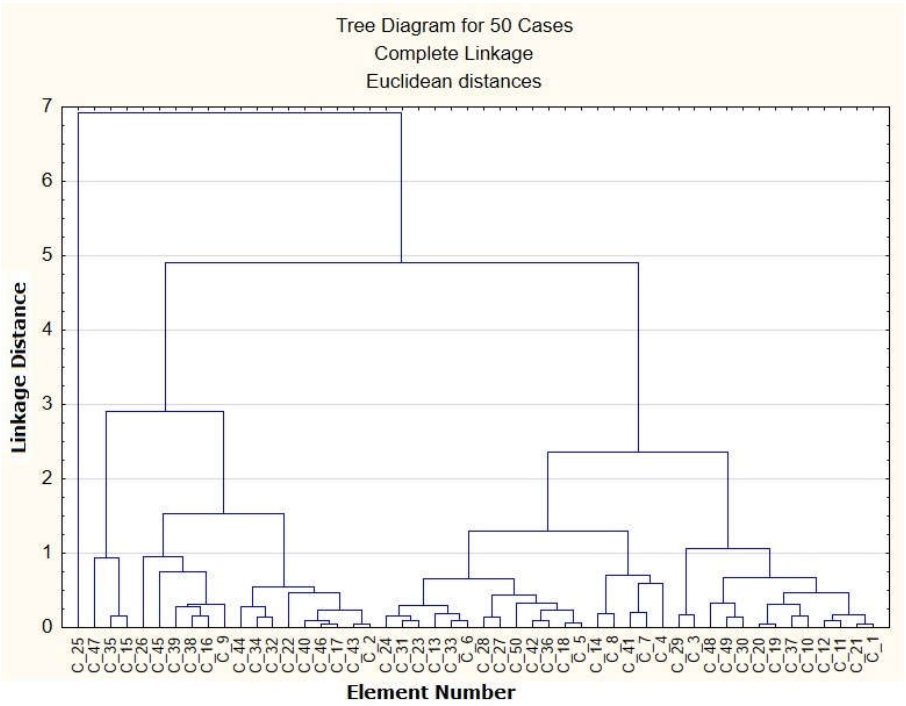

Figure 2. The vertical dendrogram of the cluster analysis using hierarchical classification

The next step is carrying out a cluster analysis of sample using k-means clustering for testing the significance of differences between groups of clusters. Using this method you can specify the initial number of clusters, which are the center of group elements with the most similar parameters. Thus at each iteration object composition of clusters varies. The optimality criterion is a minimization of variability in the cluster and maximization of variability between clusters.

Cluster analysis with clusterization by k-means clustering was carried out in the program package STATISTICA. Based on the analysis of the dendrogram shown in Fig. 2, take the number of clusters equals 2. The number of iterations is standard and equals 10. The results of the cluster analysis by k-means clustering are shown in Fig. 3.

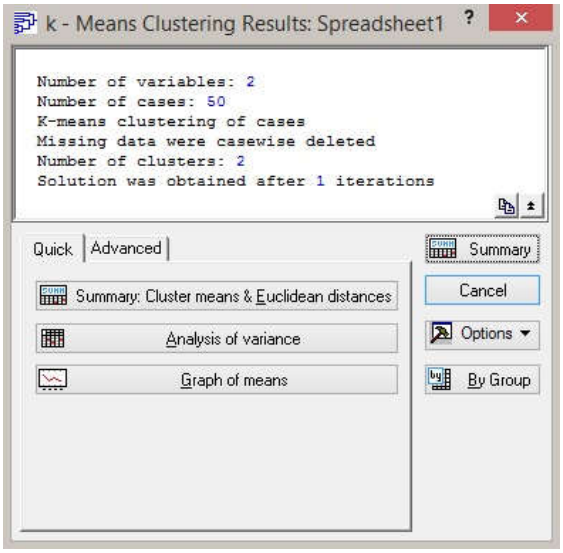

Figure 3. The results of the cluster analysis by k-means clustering

To determine the significance of differences between groups of clusters the dispersion analysis should be carried out. The results are shown in Fig. 4.

	Analysis of Variance (Spreadsheet1)					
Variable	**Between SS**	df	Within SS	df	F	signif. p
X1	23,82950	1	25,17050	48	45,4427	0,000000
X2	40,43696	1	8,56304	48	226,6688	0,000000

Figure 4. The results of the dispersion analysis

The significance level *p* of each informative parameter less than 0.05 (acceptable limit of error level). Thus, a significant difference in both parameters between clusters exists.

It is necessary to define the distance from each element included in the cluster to the cluster center. In the program the button "Summary: Cluster means & Euclidean distances" was selected (see Fig. 5).

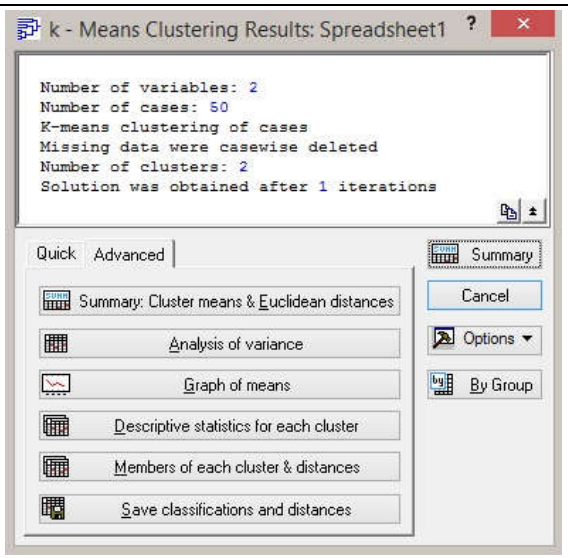

Figure 5. Selection of items for sample analysis

Fig. 6a, 6b show the composition of the clusters and the distances between elements to the clusters center calculated by the k-means clustering. The number of clusters specified in initial data for the k-means clustering, equals 2. The element No.25, which was considered as outlier, is contained in the cluster closest to him (cluster No.2). The distance between it and the center of the cluster is relatively longer than distances between other elements of the cluster and the cluster center.

Fig. 6b shows that the elements No.25, No.47 have a relatively long distance to the cluster center. In the future it will increase the field of standard deviations in the cluster No.2.

For each informative parameter form the table of average values (table is shown in Fig. 7). Fig. 8 shows a plot of means and confidence intervals for each parameter in each cluster.

According to the plot, which is shown in Fig. 8, it demonstrates that the informative parameter x_1 has a high standard deviation in the cluster No.1. It is explained by the influence of the parameter x_1 values of elements No.25 and No.47. To exclude such a case we could set the number of initial clusters to 3. Then elements No.25 and No.47 form another cluster, which can't be taken into account in further studies. Therefore, the standard deviation field of the parameter x_1 in the cluster No.2 is significantly reduced.

Case No.	Members of Cluster Number 1 (Spreadsheet1) and Distances from Respective Cluster Center Cluster contains 31 cases Distance
C_1	0,302286
C_3	0,685738
C_5	0,269869
C_6	0,047121
C_7	0,709229
C_8	0,530728
C_10	0,373040
C_11	0,178358
C_12	0,207554
C_13	0,065737
C_14	0,398170
C_18	0,270154
C_19	0,477439
C_20	0,497250
C_21	0,291017
C_23	0,147539
C_24	0,124308
C_27	0,186136
C_28	0,267342
C_29	0,808927
C_30	0,151737
C_31	0,088238
C_33	0,086717
C_36	0,159715
C_37	0,328735
C_41	0,813128
C_42	0,205884
C_45	0,819640
C_48	0,383790
C_49	0,230306
C_50	0,395344

(a)

Case No.	Members of Cluster Number 2 (Spreadsheet1) and Distances from Respective Cluster Center Cluster contains 19 cases Distance
C_2	0,230634
C_4	0,817758
C_9	0,551701
C_15	0,484567
C_16	0,451148
C_17	0,251116
C_22	0,285093
C_25	2,658986
C_26	0,898459
C_32	0,092305
C_34	0,013692
C_35	0,419575
C_38	0,531855
C_39	0,644105
C_40	0,284706
C_43	0,205632
C_44	0,111834
C_46	0,220730
C_47	1,086533

(b)

Figure 6. The distances to the cluster center of each element, which is part of: the cluster No.1 (a); the cluster No.2 (b)

Breakdown Table of Descriptive Statistics (Spreadsheet1)
N=50 (No missing data in dep. var. list)

CLUSTER	X1 Means	X1 N	X1 Std.Dev.	X1 Minimum	X1 Maximum	X2 Means	X2 N	X2 Std.Dev.	X2 Minimum	X2 Maximum
1	4,667742	31	0,927501	3,000000	7,10000	1,557419	31	0,263097	1,000000	2,300000
2	7,768421	19	2,283042	5,000000	15,60000	2,771579	19	0,298222	2,100000	3,500000
All Grps	5,846000	50	2,180078	3,000000	15,60000	2,018800	50	0,655329	1,000000	3,500000

Figure 7. Table of average values of each informative parameter

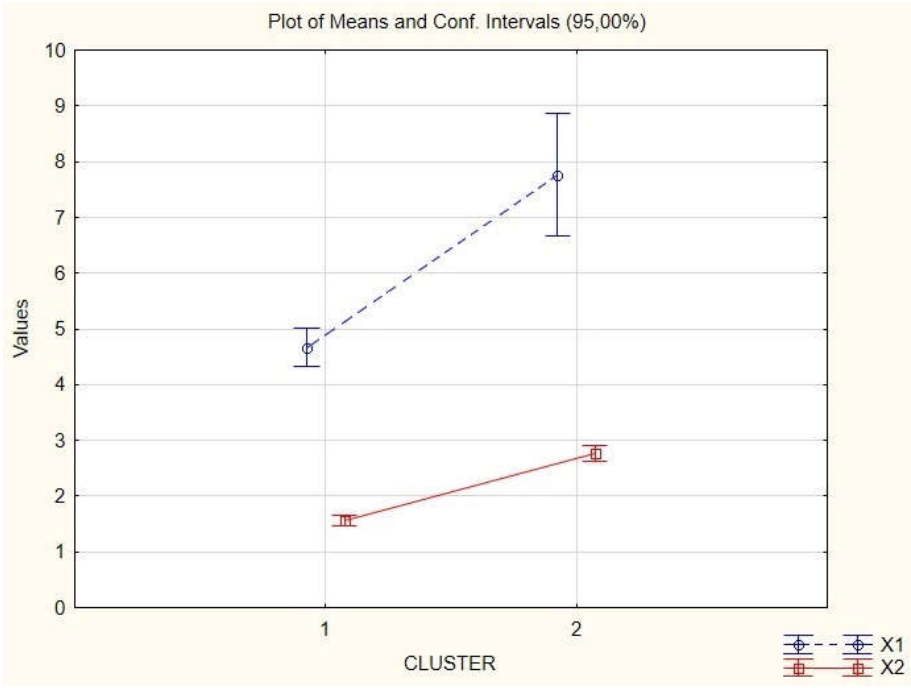

Figure 8. Plot of means and confidence intervals for each parameter in each cluster

CONCLUSION

Analyzing the results it is stated, that the use of cluster analysis for classification of semiconductor elements into classes have meaning when the element classes are well separated. Otherwise, the characteristic values of some elements can increase the standard deviation field that in the future will lead to the accuracy decrease of classification of the element from the party to a particular class.

Increasing number of informative parameters there is a problem to measure the effect of each particular parameter to the selected distance metric. In this case, it is advisable to use the Weighted Euclidean Distance as a distance metric. Thus, the "weight" is attributed to each of informative parameters. Therefore, the influence degree of each parameter on distance metric is taken into account. The difficulty lies in the evaluation of these "weights". One of the best options for the "weights" evaluation of each parameter is the expert evaluation method.

REFERENCES

1. Frenkel, I. B., Karagrigoriou, A., Lisnianski, A., & Kleyner, A. (Eds.) (2014). *Applied reliability engineering and risk analysis: Probabilistic models and statistical inference*. Chichester, UK: John Wiley & Sons Inc. doi:10.1002/9781118701881
2. Campbell, D. S., Hayes, J. A., Jones, J. A., & Schwarzenberger, A. P. (1992). Reliability behavior of electronic components as a function of time. *Quality and Reliability Engineering, 8*(3), 161–166. doi:10.1002/qre.4680080303
3. Johnson, B. G., & Gullo, L. (2000). Improvements in reliability assessment and prediction methodology. *Annual Reliability and Maintainability Symposium. 2000 Proceedings. International Symposium on Product Quality and Integrity (Cat. No.00CH37055)*. Los Angeles, USA. 181–187. doi:10.1109/rams.2000.816304
4. Gedam, S. G., & Beaudet, S. T. (2000). Monte Carlo simulation using Excel(R) spreadsheet for predicting reliability of a complex system. *Annual Reliability and Maintainability Symposium. 2000 Proceedings. International Symposium on Product Quality and Integrity (Cat. No.00CH37055)*. Los Angeles, USA. 188–193. doi:10.1109/rams.2000.816305
5. Georgiev, A., & Georgieva, N. (2002) Reliability prediction of the electronic products. *Proceedings of 37-th International Scientific Conference on Information, Communication and Energy Systems and Technologies – Session EL Electronics (ICEST 2002)*, Nis, Yugoslavia, *1,* 85–88.
6. Mishanov, R., & Piganov, M. (2015). Individual forecasting of quality characteristics by an extrapolation method for the samples of the stabilitrons and the integrated circuits. *13th International Conference The Experience of Designing and Application of CAD Systems in Microelectronics (CADSM)*. Lviv, Ukraine: IEEE. doi:10.1109/cadsm.2015.7230846

The Calculation Algorithm of the Informative Parameters of the Signal at Implementing the Method of Multiple Reflections

Yu. V. Myshkin, A. B. Efremov

Department of Instruments and Techniques for Measurement, Control, Diagnostics,
Kalashnikov Izhevsk State Technical University, Izhevsk, Russian Federation
E-mail: mubm@yandex.ru

Received: 30.11.2016

Abstract. The method of multiple reflections has several important informative parameters of the signal which allow to determine of the presence or the absence of defects in the testing object. Some parameters can be calculated using only numerical methods. In this article, the calculation algorithm of several key informative parameters of the signal is represented such as reflection coefficient on the interface "transducer – testing object", attenuation coefficient, probe pulse amplitude and position. Numerical values of informative parameters of the signal are obtained for pipes with diameter 18, 32, 57 and 73 mm by using developed algorithm and experimental data which are consistent with theoretical data. It is shown that the geometric dimensions of the pipe and the presence of the features such as electric welding seam or foreign inclusions in material of the testing object have a significant impact on the dependencies of informative parameters of the signal from the level of clamping force of piezoelectric transducer on the cylindrical surface of the pipe. The obtained results can be used at the improvement of ultrasonic inspection techniques and development of new approaches in material structure testing of the cylindrical long range objects.

Keywords: reflection coefficient, method of multiple reflections, calculation algorithm, attenuation coefficient, piezoelectric transducer, acoustic wave, clamping force, cylindrical long range objects, distant reflections, guided wave testing

INTRODUCTION

In modern industry the cylindrical long range objects such as rod rolling and pipelines for different purposes are widely used which is needed in mandatory inspection both at manufacturing company and during exploitation. For testing of such objects the active methods are basically used using torsional [1–3], rod [4–6], longitudinal [1–3, 7–9], or shear [2, 3, 10, 11] waves thus it is known cases of application of passive methods, in particular, the acoustic emission technique [12]. Among acoustic testing methods of cylindrical long range objects guided wave testing is widespread which have several advantages over classical ultrasound methods of nondestructive testing including an opportunity of rapid long range inspection, absence of necessity in scanning, and testing range of cylindrical long range objects up to 100 meters in the selected direction [13, 14]. Recently many authors are paid much attention to

modeling and experiments aimed at the investigation of the influence of external and internal viscoelastic media on the propagation of acoustic waves in pipes of different diameters [14–16].

The implementation of guided wave technique is available using piezoelectric dry coupled transducers [1, 3, 9, 17], magnetostrictive transducers [11, 18, 19] and electromagnetic acoustic (EMA) transducers [20-24] which have advantages: the possibility of testing without any contact with testing object at small gaps, generate any type of wave mode, absence of wear of element design and low absorption of acoustic wave energy by transducer [20, 21, 24, 25]. However, EMA transducers usually have low efficiency of EMA transformation in comparison with piezoelectric transducers and can not be used for testing of non-ferromagnetic materials [24–27].

Guided wave testing is predominantly used in the oil, gas and petroleum industry for the cylindrical long range objects and products from them such as sucker rods [5, 28], oil well tubing and pipes [24, 29, 30], metal cables [31–33], reinforcing bars [34, 35], workpieces for the steel springs [36], rock bolts [37, 38], and etc. Since the products represent the objects of the final length for such objects the technique has been developed and successfully used based on the method of multiple reflections (MMR) which have several advantages [4, 29, 39]:

– increases sensitivity and calculation accuracy of the wave speed and attenuation when analyzing the acoustic signals of distant reflections;

– has high informative value of testing through using additional characteristics of the acoustic signal;

– improves the distance resolution;

– decreases the dead zone through a low quality factor of the signal.

At the implementation of the MMR it is needed to consider the wave attenuation in the testing object and incomplete reflection of the signal on the interface between transducer and the surface of the testing object, called the reflection coefficient, which depend on several factors such as a clamping force of the transducer to the testing object, quality of acoustic coupling, roughness of the surface of the testing object, exact location of the transducer system on the cylindrical surface of the testing object. Reflection coefficient depend on the informative parameters of guided wave testing such as the reflection coefficient from the defects, attenuation of multiple reflection pulses, velocity of the wave propagation, efficiency of EMA and piezoelectric transformations [4–6, 29, 39]. As a rule, the reflection coefficient values may vary within the range from 0 to 1. Decreasing of this value to 0.7 and below there is the absence of growing defect amplitude effect at the distant reflections that leads to low efficiency of the MMR [39].

In this article, the algorithm and program implementation is represented and designed for increasing of the informative value of guided wave testing of the cylindrical long range objects using the MMR in real time during testing allowing, in particular, to compute the reflection coefficient and attenuation coefficient at the distant reflections, to determine probe pulse amplitude and position. There are the results of experiments confirming the efficiency of the algorithm operation on the real data.

APPROACHES USED

It is known, that at the implementation of the MMR a part of the acoustic wave energy is absorbed on the interface between transducer and the surface of the testing object and this physical phenomenon can be described by mathematical model taking into account of equipment parameters, geometric and elastic properties of the testing object, wave attenuation, and interaction with defects. The law of propagation of the rod and torsional waves in the cylin-

drical long range objects at the implementation of the MMR is known and a series of the multiple reflections is described by the expression [39]:

$$U_n = U_0 \cdot R_e{}^n \cdot e^{-\delta\cdot(x_n - x_0)}, \tag{1}$$

where U_n – echo pulse amplitude from the end of the testing object at the n-th reflection; U_0 – probe pulse amplitude; R_e – reflection coefficient on the interface between transducer and the surface of the testing object; δ – attenuation coefficient of acoustic wave; $x_n = 2\cdot L\cdot n + x_0$ – position of the n-th reflection, $2\ L\ n$ – traveled distance of acoustic wave at the n-th reflection; x_0 – probe pulse position, $L = C\cdot t$ – length of the testing object, C – propagation velocity of acoustic wave, t – propagation time of acoustic wave.

The problem is to find the reflection coefficient R_e for which the equation (1) on the reflection n at the reflection amplitude U_n and the distance to the reflection x_n has a unique solution. It also follows from the equation (1) that the variables R_e, U_0, and δ are interdependent, therefore, the calculation of their values should be carried out on the different reflections n.

THE CALCULATION ALGORITHM

The solution of the problem can be accomplished by using the bisection method based on the successive approximation to the desired value of the unknown quantity by dividing the search interval into two and calculation of interdependent unknown variables on each iteration.

Input data

As the input data, the peak coordinates of the two pulses reflected from the end of the testing object are used: U_n, U_m – amplitudes of the echo pulses from the end of the testing object at the n-th and m-th reflection respectively, x_n, x_m – propagation distance of acoustic wave to the n-th and m-th reflection respectively $x_n = 2\cdot L\cdot n + x_0$ and $x_m = 2\cdot L\cdot m + x_0$, when condition $m > n$ must be satisfied, where n and m – whole numbers.

It is calculated the distance which equal to double size of the length of pipe and corresponding to the space between the two pulses on the distance scale:

$$\Delta x = 2L = \frac{x_m - x_n}{m - n}. \tag{2}$$

Probe pulse position on the x-axis is determined as

$$x_0 = x_n - n\cdot\Delta x. \tag{3}$$

Initial value of attenuation coefficient is introduced and reflection coefficient is calculated for launching the calculation cycle

$$\delta = 0,\ \ R_{en} = 1,\ \ R_{em} = \left[\frac{U_m}{U_0}\right]^{\frac{1}{m}},\ \ R_e = \frac{R_{en} + R_{em}}{2}, \tag{4}$$

where R_{en} – reflection coefficient at the n-th reflection; R_{em} – reflection coefficient at the m-th reflection.

Probe pulse amplitude is calculated by using this data

$$U_0 = \frac{U_n}{R_e{}^n}. \tag{5}$$

Formulas (2)–(5) are used for the calculation one time only and they are needed for launching the main calculation cycle.

Main calculation cycle

The calculation algorithm of the informative parameters of the signal in the main calculation cycle at iteration step k looks as follows.

1. Computation R_e at the n-th reflection

$$R_{en} = \left[\frac{U_n}{U_0 \cdot e^{-\delta \cdot (x_n - x_0)}} \right]^{\frac{1}{n}}. \tag{6}$$

2. Computation R_e at the m-th reflection

$$R_{em} = \left[\frac{U_m}{U_0 \cdot e^{-\delta \cdot (x_m - x_0)}} \right]^{\frac{1}{m}}. \tag{7}$$

3. Calculation of the average value R_e

$$R_e = \frac{R_{en} + R_{em}}{2}. \tag{8}$$

4. Evaluation of the value ΔR_e

$$\Delta R_e = \left| (R_e)_k - (R_e)_{k-1} \right|. \tag{9}$$

5. Calculation of the attenuation coefficient with considering the calculated reflection coefficient R_e

$$\delta = -\frac{\ln\left(\frac{U_m}{U_0 \cdot {R_e}^m} \right)}{x_m - x_0}. \tag{10}$$

6. Calculation of the probe pulse amplitude with considering the calculated reflection coefficient R_e (formula 8) and attenuation coefficient δ (formula 10)

$$U_0 = \frac{U_n}{{R_e}^n \cdot e^{-\delta \cdot (x_n - x_0)}}. \tag{11}$$

The exit from the cycle body is carried out when the condition $\Delta R_e \le 10^{-6}$ is satisfied. Thus, the represented algorithm allows to obtain the values of reflection coefficient R_e, attenuation coefficient δ, probe pulse amplitude U_0 and position x_0 with a specified accuracy.

Implementation of algorithm

The algorithm is implemented as part of program in the software called Prince which is written using high level programming language Object Pascal and designed for equipment management, recording of acoustic signals and the output of main informative parameters of the signal in the real-time, including the values of reflection coefficient, attenuation coefficient, probe pulse amplitude and position on the monitor screen. A scheme of calculation algorithm of the reflection coefficient is provided in Fig. 1 and it includes a data input unit, pre-

liminary calculation unit, result output unit and main cycle body which contains the units of reflection coefficient calculation, error checking, computation of attenuation coefficient and probe pulse amplitude.

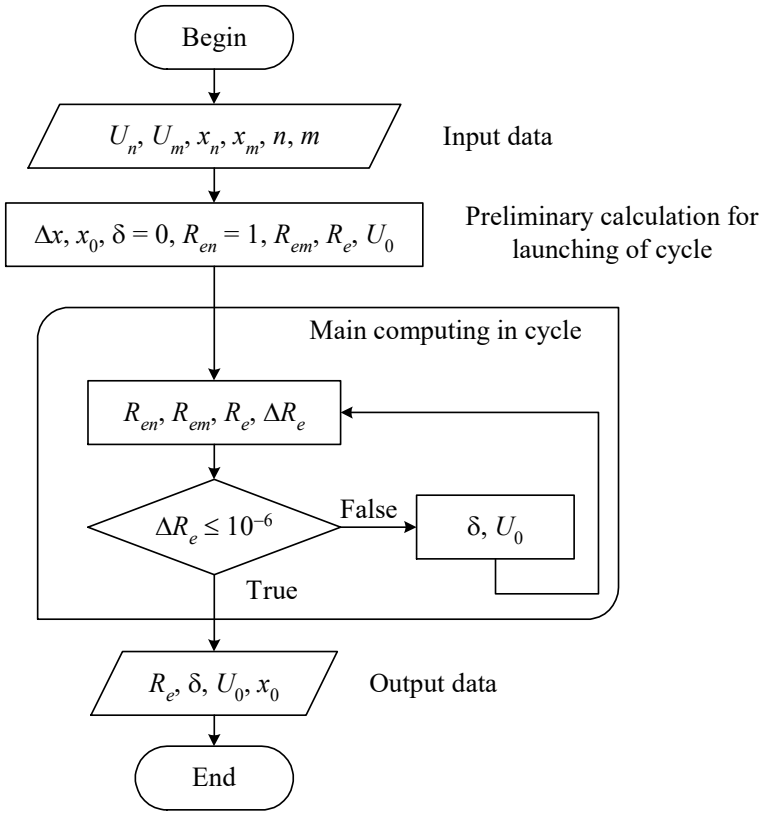

Figure 1. A scheme of the calculation algorithm of the informative parameters of the signal

For instance, the operation of the algorithm on the real data is represented in table 1. As the input data for calculating, the following data are used: $n = 1$, $m = 5$, $U_n = 931.091$ mV, $U_m = 711.914$ mV, $x_n = 2.018$ m, $x_m = 9.630$ m, $C = 3250$ m/s. The output data: $R_e = 0.954193$, $\delta = 0.010744$, $U_0 = 995.710785$ mV, $x_0 = 0.1144$ m.

Table 1. An example of the operation of the algorithm on each iteration

Iteration number k	Reflection coefficient at n-th reflection R_{en}	Reflection coefficient at m-th reflection R_{em}	Average value of reflection coefficient R_e	Attenuation coefficient δ	Probe pulse amplitude U_0 mV	Condition ΔR_e
1	1	0.9477353	0.9738677	0	956.0757988	-
2	0.9738677	0.9427294	0.9582985	0.0086066	987.6548819	0.0155692
3	0.9582985	0.9520905	0.9551945	0.0103168	994.0947786	0.0031040
4	0.955195	0.9539537	0.9545741	0.0106584	995.3877881	0.0006204
5	0.9545741	0.954326	0.9544501	0.0107267	995.6465917	0.0001240
6	0.9544501	0.9544004	0.9544253	0.0107404	995.6983605	0.0000248
7	0.9544253	0.9544153	0.9544203	0.0107431	995.7087146	0.0000050
8	0.9544203	0.9544183	0.9544193	0.0107437	995.7107855	0.0000010

As shown from table 1, for calculating with certain accuracy according to the condition $\Delta R_e \le 10^{-6}$ the eight iterations are enough to reach of satisfactory solution.

EXPERIMENTAL SETUP

The experiment for verifying the operation of the calculation algorithm of the informative parameters of the signal was prepared and performed. The experimental setup is represented in Fig. 2 described in [40] and consists of two EMA transducers, piezoelectric transducer, probe pulse generator, control block with preamplifier, analog-digital converter board embedded in personal computer. EMA transducers are located on the cylindrical surface of the pipe at the diametrically opposite sides near the pipe end and piezoelectric transducer is located in the middle between two EMA transducers on the cylindrical surface of pipe as well. The pipes with length 950 mm, diameter 18, 32, 57, 73 mm and wall thickness 3, 4.2, 5, 5.5 mm respectively are used in the experiment and pipe with diameter 18 mm has electric welding seam along the entire length of pipe.

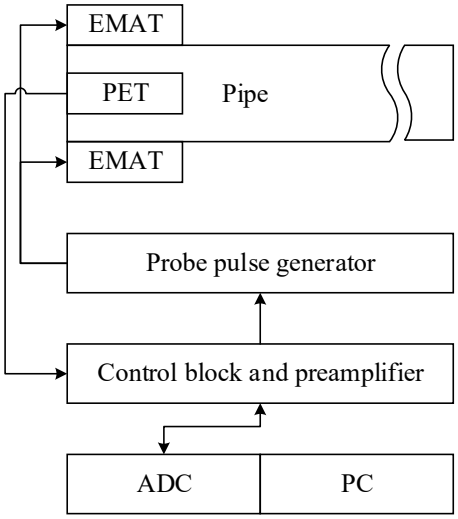

Figure 2. A scheme of the experimental setup, EMAT – electromagnetic-acoustic transducer, PET – piezoelectric transducer, ADC – analog-digital converter, PC – personal computer

The echo signal is the measurement result (Fig. 3) obtained by using the software Prince and represented the series of echo pulses of multiple reflections from the opposite ends of the pipe. For example, in figure 3 the echo signals are illustrated for pipe with diameter 18 mm under one of minimum clamping force and pipe with diameter 57 mm under maximum clamping force. From the presented echo signals it can be concluded that acoustic wave attenuation, acoustic noise level and amplitude of unwanted types of wave modes for pipe with diameter 18 mm is higher than for pipe with diameter 57 mm, it can be explained the presence of electric welding seam along the pipe.

RESULTS AND DISCUSSION

Calculated dependencies of reflection coefficient, attenuation coefficient and probe pulse amplitude from the wave propagation distance for the pipe with diameter 18 mm and 57 mm are given in Fig. 4. The following graphs for the pipe with diameter 18 mm (Fig. 4 a, c, e) demonstrate the insignificant nonlinear dependence of reflection coefficient (Fig. 4 a) from the wave propagation distance the cause of which can be high amplitudes of acoustic noise and unwanted types of wave modes due to structural and geometrical features of the pipe as well as the presence of electric welding seam along the testing object.

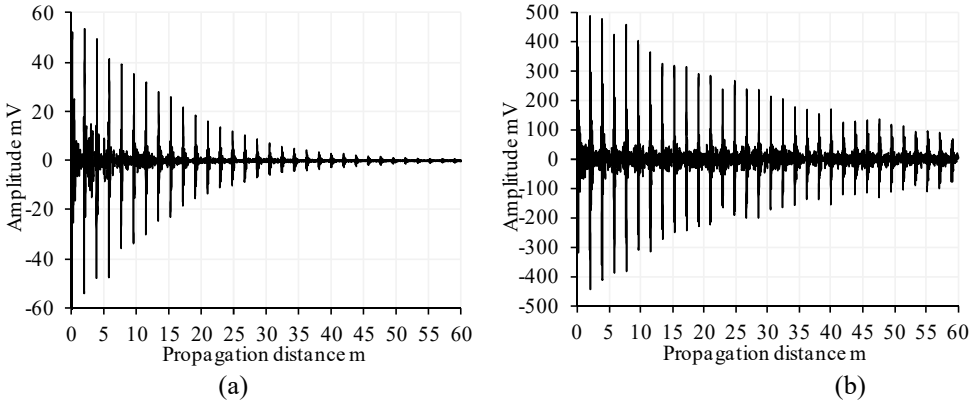

Figure 3. Experimental signals of the series of echo pulses of multiple reflections obtained on the pipes with diameter 18 mm (a) and 57 mm (b)

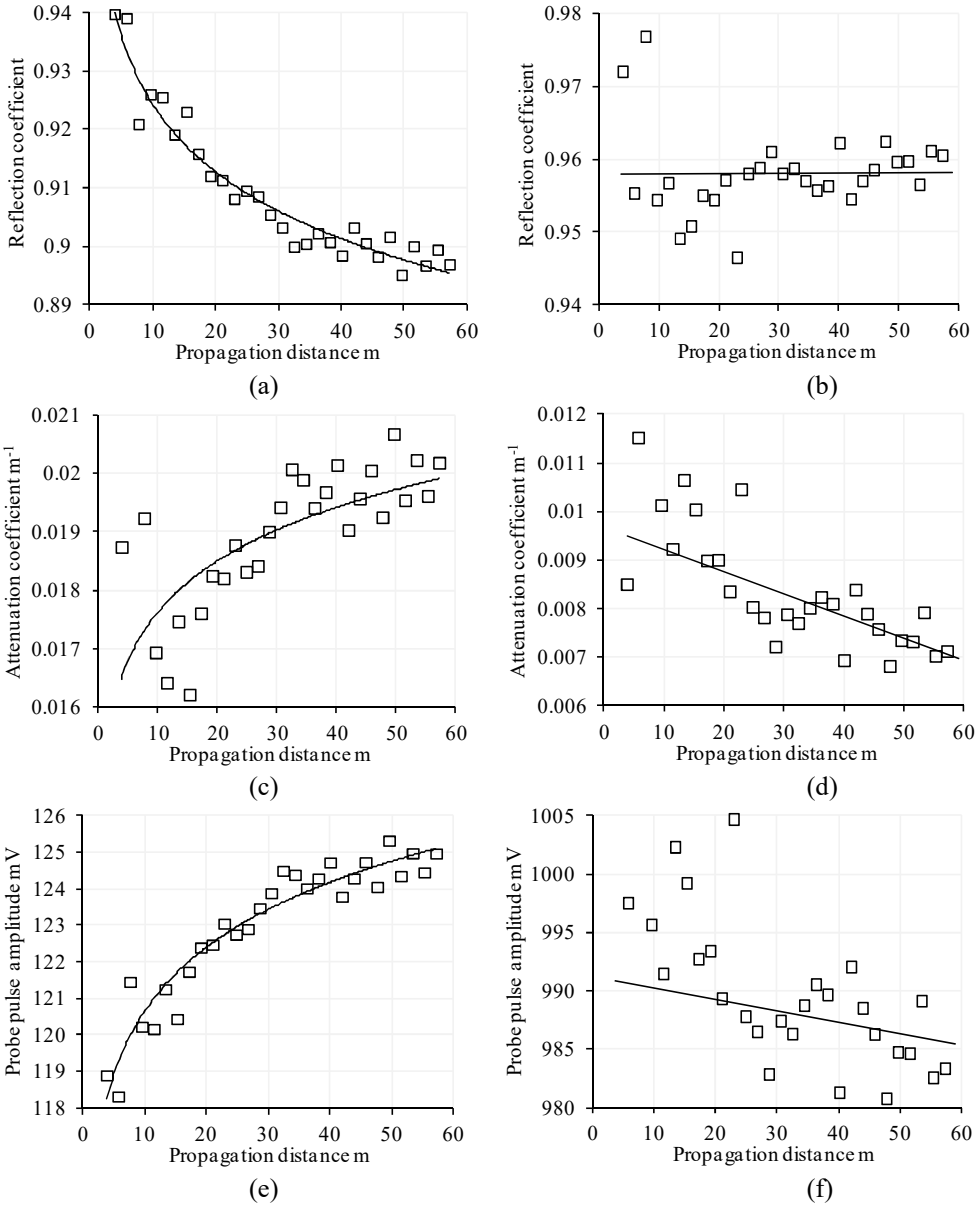

Figure 4. Dependencies of calculated reflection coefficient (a, b), attenuation coefficient (c, d), and probe pulse amplitude (e, f) from the wave propagation distance at the multiple reflections in pipe with diameter 32 mm (a, c, e) and 73 mm (b, d, e)

Main values of attenuation coefficient are within the range 0.016÷0.021 for pipe with diameter 18 mm (Fig. 4 c) and 0.006÷0.012 for pipe with diameter 57 mm (Fig. 4 d). Since the attenuation coefficient is a constant value in defined medium then the average value of attenuation coefficient at the $5^{th} – 8^{th}$ reflection is taken as a constant where unwanted types of wave modes and acoustic noise amplitudes have insignificant influence. Using such approach the calculated attenuation coefficient for pipe with diameter 18, 32, 57, 73 mm is amounted 0.018, 0.024, 0.009, 0.016 m^{-1} respectively.

For comparison of the calculated results the definitions of graphs are accepted on the evaluation of clamping force which carried out the amplitude of the first echo pulse from the opposite end of the pipe (first reflection). Generalized dependencies of average values of reflection coefficient from the first echo pulse amplitude from pipe end for different diameters are represented in Fig. 5. Reflection coefficient for pipe with the smallest diameter 18 mm varies widely from 0.78 to 0.93. However, the variation range of reflection coefficient for pipes with large diameters 32, 57, and 73 mm varies within a range 0.04÷0.08 (0.84÷0.92, 0.93÷0.97, 0.95÷1 for pipe with diameter 32, 73, and 57 mm respectively). Thus, reflection coefficient at the amplitude 500 mV of the first echo pulse from the opposite end of the pipe for pipes with diameters 18, 32, 57, and 73 mm is amounted 0.82, 0.86, 0.97, and 0.94 respectively.

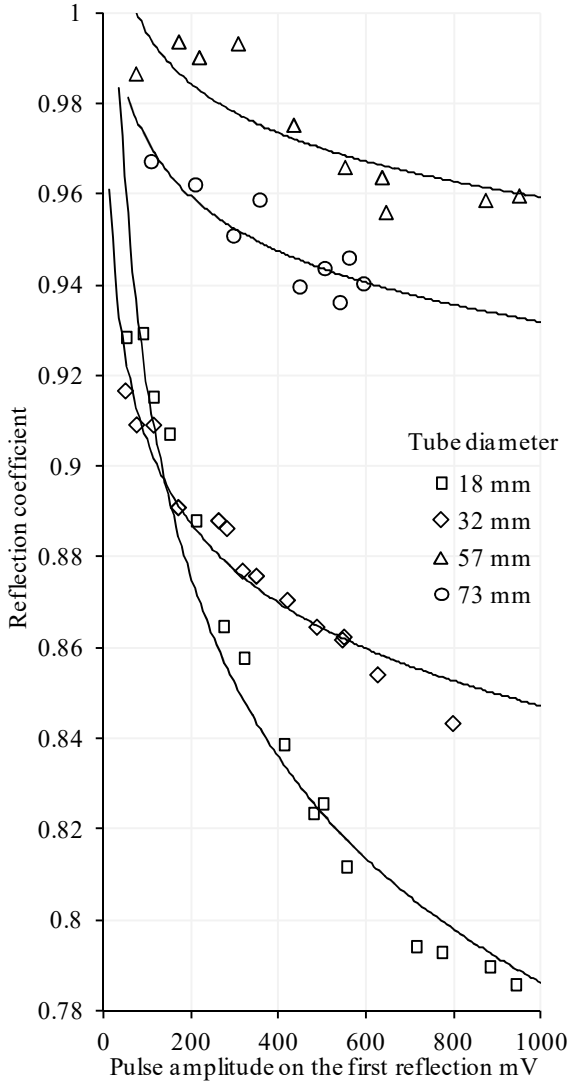

Figure 5. Dependence of average value of reflection coefficient from echo pulse amplitude on the first reflection for pipes of different diameter

General decreasing dependence of reflection coefficient from the first echo pulse amplitude from the opposite end of the pipe is observed on the graphs (Fig. 5). However, this dependence is most pronounced for pipe with diameter 18 mm that can be related with presence of electric welding seam which has a structure differing from main material structure of pipe. Therefore, it can be assumed that the presence of structural inhomogeneity of material in the testing object leads to significant changes of the reflection coefficient at the different clamping force of piezoelectric transducer to the cylindrical surface of pipe. Hence, this approach can be used for development of the technique of guided wave testing for the evaluation of the material structure and the presence of foreign inclusions in pipes with different diameters.

CONCLUSIONS

Thus, according to the results of the developed calculation algorithm of the informative parameters of the signal and experimental investigations at the implementation of the method of multiple reflections it is possible to make the following conclusions:

– presented algorithm allows to obtain with high accuracy in real-time of reflection coefficient (absolute error of the calculated values of reflection coefficient for pipe with diameter 57 mm and 73 mm is amounted 0.02), attenuation coefficient, probe pulse amplitude and position;

– calculated values of reflection coefficient (from 0.77 to 0.99) by using algorithm on the real testing object are consistent with the theoretical data;

– the presence of acoustic noise and unwanted types of wave modes does not have significant influence on the calculation results;

– with increasing the clamping force of piezoelectric transducer to the cylindrical surface of the pipe the reflection coefficient slightly decreases;

– the reflection coefficient has a nonlinear dependence in pipes of small diameters at the presence of foreign inclusions.

The results of the work can be used for the improvement of existing techniques of guided wave testing as well as for the development of approaches in the evaluation of material structure of cylindrical long range objects based on detection of dependence of reflection coefficient from clamping force of piezoelectric transducer on the pipe surface.

ACKNOWLEDGMENTS

This work was supported by the Russian Scientific Foundation, project no. 15-19-00051.

REFERENCES

1. Alleyne, D. N., Vogt, T., & Cawley, P. (2009). The choice of torsional or longitudinal excitation in guided wave pipe inspection. *Insight – Non-Destructive Testing and Condition Monitoring, 51*(7), 373–377. doi:10.1784/insi.2009.51.7.373
2. Mohr, W., & Holler, P. (1976). On inspection of thin-walled tubes for transverse and longitudinal flaws by guided ultrasonic waves. *IEEE Transactions on Sonics and Ultrasonics, 23*(5), 369–374. doi:10.1109/t-su.1976.30893
3. Silk, M., & Bainton, K. (1979). The propagation in metal tubing of ultrasonic wave modes equivalent to Lamb waves. *Ultrasonics, 17*(1), 11–19. doi:10.1016/0041-624x(79)90006-4
4. Budenkov, G. A., Nedzvetskaya, O. V., Budenkov, B. A., Lebedeva, T. N., & Zlobin, D. V. (2004). Acoustic nondestructive testing of rods using multiple reflections. *Russian Journal of Nondestructive Testing*, *40*(8), 541–544. doi:10.1007/s11181-005-0007-y

5. Budenkov, G. A., Nedzvetskaya, O. V., Zlobin, D. V., & Lebedeva, T. N. (2004). The application efficiency of rod and torsional waves for checking rod-shaped roll stock. *Russian Journal of Nondestructive Testing, 40*(3), 147–151. doi:10.1023/b:runt.0000040171.56679.6b
6. Budenkov, G. A., & Nedzvetskaya, O. V. (2004). Principal regularities of Pochhammer-wave interaction with defects. *Russian Journal of Nondestructive Testing, 40*(2), 99–108. doi:10.1023/b:runt.0000036552.46582.a0
7. Alleyne, D. N., & Cawley, P. (1996). The excitation of Lamb waves in pipes using dry-coupled piezoelectric transducers. *Journal of Nondestructive Evaluation, 15*(1), 11–20. doi:10.1007/bf00733822
8. Wang, T., Yang, C., Ye, L., Spray, D., & Xiang, Y. (2014). Evaluation of guided wave propagation in steel pipes. *Recent Advances in Structural Integrity Analysis – Proceedings of the International Congress (APCF/SIF-2014)*, 255–260. doi:10.1533/9780081002254.255
9. Lowe, P., Sanderson, R., Pedram, S., Boulgouris, N., & Mudge, P. (2015). Inspection of pipelines using the first longitudinal guided wave mode. *Physics Procedia, 70*, 338–342. doi:10.1016/j.phpro.2015.08.079
10. Fateri, S., Lowe, P. S., Engineer, B., & Boulgouris, N. V. (2015). Investigation of ultrasonic guided waves interacting with piezoelectric transducers. *IEEE Sensors Journal, 15*(8), 4319–4328. doi:10.1109/jsen.2015.2414874
11. Xu, J., Wu, X., Kong, D., & Sun, P. (2015). A guided wave sensor based on the inverse magnetostrictive effect for distinguishing symmetric from asymmetric features in pipes. *Sensors, 15*(3), 5151–5162. doi:10.3390/s150305151
12. Budenkov, G. A., Nedzvetskaya, O. V., Sergeev, V. N., & Zlobin, D. V. (2000). Potentialities of acoustic emission technique for inspection of main pipelines. *Russian Journal of Nondestructive Testing, 36*(2), 97–102. doi:10.1007/bf02759403
13. Cawley, P. (2003). Practical long range guided wave inspection – Managing Complexity. *AIP Conference Proceedings, 61*(1), 66–74. doi:10.1063/1.1570116
14. Leinov, E., Lowe, M. J., & Cawley, P. (2015). Investigation of guided wave propagation and attenuation in pipe buried in sand. *Journal of Sound and Vibration, 347*, 96–114. doi:10.1016/j.jsv.2015.02.036
15. Murav'eva, O. V., Len'kov, S. V., & Myshkin, Y. V. (2016). Factors affecting attenuation of torsional waves in pipes loaded on contact viscoelastic media. *Russian Journal of Nondestructive Testing, 52*(9), 485–491. doi:10.1134/s1061830916090035
16. Na, W., & Yoon, H. (2007). Wave-attenuation estimation in fluid-filled steel pipes: The first longitudinal guided wave mode. *Russian Journal of Nondestructive Testing, 43*(8), 549–554. doi:10.1134/s1061830907080074
17. Zhou, W., Yuan, F., & Shi, T. (2016). Guided torsional wave generation of a linear in-plane shear piezoelectric array in metallic pipes. *Ultrasonics, 65*, 69–77. doi:10.1016/j.ultras.2015.10.021
18. Cheong, Y. M., Kim, S., & Jung, H. K. (2007). Application of magnetostrictive transducer for the long-range guided wave inspection. *The Mechanical Behavior of Materials X, 345–346,* 1295–1298. doi:10.4028/www.scientific.net/KEM.345-346.1295
19. Guo, P., Li, H., Tian, Z., & Xu, H. (2015). Guided wave damage detection in power-plant-tubes by using magnetostrictive transducer arrays. *Pressure Vessels and Piping Conference. Volume 6A: Materials and Fabrication*. Boston, USA: ASME. doi:10.1115/pvp2015-45845
20. Huang, S., & Wang, S. (2016). The electromagnetic ultrasonic guided wave testing. In Huang, S., & Wang, S. (Eds.) *New Technologies in Electromagnetic Non-destructive Testing*. Singapore: Springer. doi:10.1007/978-981-10-0578-7_1
21. Murav'eva, O. V., Len'kov, S. V., & Murashov, S. A. (2016). Torsional waves excited by electromagnetic–acoustic transducers during guided-wave acoustic inspection of pipelines. *Acoustical Physics, 62*(1), 117–124. doi:10.1134/s1063771015060093
22. Murayama, R. (2016). A new guide wave inspection system using three polarized transverse wave EMATs without any couplant. *Journal of Sensor Technology, 6*(4), 110–121. doi:10.4236/jst.2016.64009

23. Furusawa, A., Kojima, F., & Morikawa, A. (2015). Mode control of guided wave in magnetic hollow cylinder using electromagnetic acoustic transducer array. *Nuclear Engineering and Technology, 47*(2), 196–203. doi:10.1016/j.net.2014.12.007

24. Hirao, M., & Ogi, H. (2003). EMATs for Science and Industry. Noncontacting Ultrasonic Measurements. Boston, USA: Springer. doi:10.1007/978-1-4757-3743-1

25. Cheng, J., & Bond, L. J. (2015). Assessment of ultrasonic NDT methods for high speed rail inspection. *AIP Conference Proceedings*, *1650*, 605–614. doi:10.1063/1.4914660

26. Mikhailov, A. V., Gobov, Y. L., Smorodinskii, Y. G., & Shcherbinin, S. V. (2015). An electromagnetic–acoustic transducer with pulsed biasing. *Russian Journal of Nondestructive Testing, 51*(8), 467–475. doi:10.1134/s1061830915080069

27. Thring, C., Fan, Y., & Edwards, R. (2016). Focused Rayleigh wave EMAT for characterisation of surface-breaking defects. *NDT & E International, 81*, 20–27. doi:10.1016/j.ndteint.2016.03.002

28. Brook, M. V., & Wiley InterScience (Online service). (2012). Technique development and probe design for cylindrical rod inspection. In *Ultrasonic inspection technology development and search unit design: Examples of practical applications* (pp. 135–162). Hoboken, USA: John Wiley & Sons, Inc. doi:10.1002/9781118104781.ch7

29. Budenkov, G. A., Nedzvetskaya, O. V., Zlobin, D. V., & Murashov, S. A. (2006). Interaction of torsion waves with longitudinal cracks in tubes. *Russian Journal of Nondestructive Testing, 42*(6), 392–397. doi:10.1134/s1061830906060064

30. Sabhnani, R. M., Humphrey, V., Zaghari, B., & Moshrefi-Torbati, M. (2015). Fault detection in small diameter pipes using ultrasonic guided wave technology. *Sensors and Smart Structures Technologies for Civil, Mechanical, and Aerospace Systems 2015, 9435*, 1–13. doi:10.1117/12.2085494

31. Baltazar, A., Hernandez-Salazar, C. D., & Manzanares-Martinez, B. (2010). Study of wave propagation in a multiwire cable to determine structural damage. *NDT & E International, 43*(8), 726–732. doi:10.1016/j.ndteint.2010.08.007

32. Farhidzadeh, A., & Salamone, S. (2015). Reference-free corrosion damage diagnosis in steel strands using guided ultrasonic waves. *Ultrasonics, 57*, 198–208. doi:10.1016/j.ultras.2014.11.011

33. Legg, M., Yücel, M. K., Kappatos, V., Selcuk, C., & Gan, T. (2015). Increased range of ultrasonic guided wave testing of overhead transmission line cables using dispersion compensation. *Ultrasonics, 62*, 35–45. doi:10.1016/j.ultras.2015.04.009

34. Karayannis, C. G., Chalioris, C. E., Angeli, G. M., Papadopoulos, N. A., Favvata, M. J., & Providakis, C. P. (2016). Experimental damage evaluation of reinforced concrete steel bars using piezoelectric sensors. *Construction and Building Materials, 105*, 227–244. doi:10.1016/j.conbuildmat.2015.12.019

35. Sharma, S., & Mukherjee, A. (2010). Longitudinal guided waves for monitoring chloride corrosion in reinforcing bars in concrete. *Structural Health Monitoring, 9*(6), 555–567. doi:10.1177/1475921710365415

36. Murav'ev, V. V., Murav'eva, O. V., Strizhak, V. A., Pryakhin, A. V., & Fokeeva, E. N. (2014). An analysis of the comparative reliability of acoustic testing methods of bar stock from spring steels. *Russian Journal of Nondestructive Testing, 50*(8), 435–442. doi:10.1134/s1061830914080063

37. Stepinski, T., & Mattson, K. (2015). Instrument for rock bolt inspection by means of ultrasound. *2015 IEEE International Ultrasonics Symposium (IUS)*. Taipei, Taiwan: IEEE. doi:10.1109/ultsym.2015.0343

38. Sun, B., Zeng, S., Guo, S., & Yang, C. (2015). Variation characteristics of stress wave speed for anchorage system under instantaneous excitation. *Geotechnical and Geological Engineering, 33*(3), 751–757. doi:10.1007/s10706-015-9846-z

39. Murav'eva, O. V., & Zlobin, D. V. (2013). The acoustic path in the method of multiple reflections during nondestructive testing of linearly extended objects. *Russian Journal of Nondestructive Testing, 49*(2), 93–99. doi:10.1134/s1061830913020058

40. Murav'eva, O. V., Len'kov, S. V., Murav'ev, V. V., Myshkin, Y. V., & Murashov, S. A. (2016). Factors that affect the excitation effectiveness of torsional waves during waveguide inspection of pipes. *Russian Journal of Nondestructive Testing, 52*(2), 78–84. doi:10.1134/s1061830916020066

Method for Calculating the Potential Distribution of Nonlinear Ion Mirror and Modeling a Dust-Impact Mass Spectrometer

I. Piyakov [1], D. Rodin [2], M. Rodina [1]

[1] Department of design and technology of electronic systems and devices, Samara University, Samara, Russia
E-mail: m.a.rodina@yandex.ru
[2] Department of radioengineering, Samara University, Samara, Russia
E-mail: rodin@ssau.ru

Received: 09.11.2016

Abstract. Dust-impact mass spectrometers are used to analyze the chemical composition of micrometeoroids and space debris particles. The focusing of charged particles packets produced by high-speed interaction is complicated because of their high energy spread. The focusing can be achieved by using high voltages, or using electrical fields with special distributions. The method of analytical calculation of such nonlinear distribution is given in this paper. The nonlinear electrostatic ion mirror with a given distribution of potential provides the temporal focusing of ions with an energy spread of up to 25% of the accelerating voltage. To verify the focusing ability of the resulting potential distribution the trajectories of ions with different coordinates of origin and different initial energy spread were calculated. The mass resolution is calculated on the basis of ions trajectories and times of flight. The results of trajectories simulation allow us to conclude that nonlinear ion mirror provides sufficient level of temporal focusing to resolve simple substances such as aluminium, ferrum, lithium and other metals that can be detected in the chemical composition of micrometeoroids and space debris particles.

Keywords: dust-impact mass spectrometer; time of flight mass spectrometer; mass analyzer; nonlinear ion mirror; reflectron

INTRODUCTION

Time of flight mass spectrometers are widely used not only in laboratory but also for carrying out *in-situ* space experiments [1, 2]. The latter includes the scope of the study of outer space, the chemical composition of cosmic dust particles of natural and artificial origin, micrometeoroids and space debris particles. For such analysis of the chemical composition a dust-impact time of flight mass spectrometers are used, which principle of operation is based on the mechanism of impact ionization [3]. The advantages of time of flight mass spectrometer as compared to other mass analyzing devices are: small size, high sensitivity, and the ability to determine the composition of cosmic dust particles having a random nature of the interaction of particles with the target of the device. The use of ion mirrors in the design of the device improves the performance of the mass spectrometer by increasing the ion path length in the fieldless areas, as well as realization of the space-time focusing of the ion packets in the

detector plane [4, 5]. However, with the increase of the initial energy spread of ions (e.g., resulting from high-speed interaction of micrometeorite and target) the temporal error in focusing of ion packets is also increased, which limits the performance of this type of analyzers and requires the use of high accelerating voltage [6] or nonlinear potential distribution in reflector [7].

Analytical Expression for Ideal Focusing

The authors of [8] propose a method for calculating the distribution of the nonlinear axial potential electrostatic ion mirror, providing total independence of the drift time of the ions from their initial energy. The method is based on the fact that ions with different initial energy meet their unique reflection equipotentials, which longitudinal coordinates monotonically increase with the energy of the corresponding ions. Thus, the ions with higher energy have a longer path within the ion mirror, which compensates the initial energy spread of the ions.

Expression describing the desired potential distribution in the reflector can be written as the integral equation:

$$\Delta t(\Delta U) = 2\sqrt{\frac{m}{2q}}\int_0^{z^*}\frac{dz}{\sqrt{\Delta U - U}}, \qquad (1)$$

where m, q – mass and charge of ion; z – current longitudinal coordinate in the reflection area; z^* – coordinate of the turning point of ions; $q\Delta U$ – the initial energy of ions; U – potential in the area of reflection (entry point in this area corresponds to the zero potential), $\Delta t(\Delta U)$ – the difference in time of flight for $q\Delta U$ initial energy, which should be compensated.

Consider this method of calculation applied to the design of dust-impact mass spectrometer.

Structure of the Device and Desired Reflector Potential Distribution

Figure 1 shows the structure of dust-impact time of flight mass spectrometer with a nonlinear reflector. Dust particles at the speed of V_0 hit the target 1 and form a plasma cloud. Initially, the target has a potential equal to the accelerating voltage, the accelerating field separates the charged particles, ions are accelerated and get into nonlinear reflector, electrons are deposited on the target and form a current pulse amplified by the amplifier 5. This pulse turns off controlled pulsed voltage source 6 to remove accelerating field. Controlled pulsed voltage source 6 forms impulse to start recording. Ions reflect in the ion mirror and, as the accelerating voltage is already turned off, pass through the target, reflect in a parabolic reflector, pass through a spherical corrector and hit the detector 4.

Here 1 – a target with holes, 2 – flat grid, 3 – parabolic reflector, 4 – detector, 5 – electron pulse amplifier, 6 – accelerating voltage generator.

Time of flight of the ion with mass m and charge q for the path inside of the device, except the nonlinear reflector, can be written as following:

$$t_\Sigma(\Delta U) = \left\{\frac{2L_1}{U_1}\left(\sqrt{U_1+\Delta U}-\sqrt{\Delta U}\right)+\frac{2L_{fl}}{\sqrt{U_1+\Delta U}}+\right.$$

$$+\frac{4L_3\sqrt{U_1+\Delta U}}{kU_1}+\frac{4L_5}{U_1}\left(\sqrt{U_1+\Delta U}-\sqrt{\Delta U}\right)\Bigg\}, \tag{2}$$

where L_1 – length of accelerating gap; L_{fl} – length of fieldless areas; L_3 – distance between parabolic electrodes; L_5 – length of decelerating gap; U_1 – accelerating potential; ΔU – initial kinetic energy of ion.

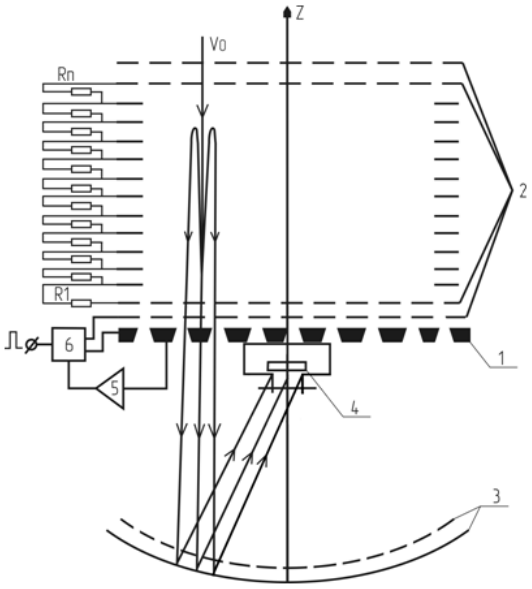

Figure 1. Structure of the device

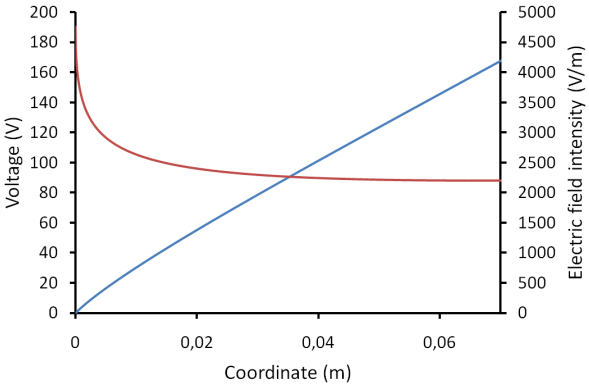

Figure 2. Desired distribution of potential (blue line) and field intensity (red line)

We can regroup summands in (2) to obtain coefficients for the different powers of ΔU:

$$C_0=\frac{t_\Sigma(0)}{\sqrt{m/2q}}=\frac{1}{\sqrt{U_1}}\left(2L_1+L_{fl}+\frac{4L_3}{k}+4L_5\right), \tag{3}$$

$$C_2=-\left(\frac{2L_1}{U_1}+\frac{4L_5}{U_1}\right), \tag{4}$$

$$C_2=\frac{2L_1}{U_1}+\frac{4L_3}{kU_1}+\frac{4L_5}{U_1}, \tag{5}$$

$$C_3=L_{fl}. \tag{6}$$

Thus, the expression describing time of flight difference will be the follows:

$$\Delta t_\Sigma(\Delta U)=\sqrt{\frac{m}{2q}}\left(C_0-C_1\sqrt{\Delta U}-C_2\sqrt{U_1+\Delta U}-C_3\frac{1}{\sqrt{U_1+\Delta U}}\right). \tag{7}$$

Solution of the equation (1) can be found trough integration:

$$z(U)=\frac{1}{2\pi}\int_0^U\frac{\Delta t_\Sigma(\Delta U)}{\sqrt{U-\Delta U}}d\Delta U. \tag{8}$$

Using expressions (3)–(6) and introducing:

$$u = \frac{U}{U_1}, \tag{9}$$

we can obtain inverse function, which describes dependence of longitudinal coordinates from potential inside the reflector:

$$z(u) = \frac{1}{2\pi}\left\{2C_0\sqrt{U_1 u} - \frac{\pi}{2}C_1 U_1 u - C_2 U_1\left(\sqrt{u} + (1+u)\arcsin\sqrt{\frac{u}{1+u}}\right) - \right.$$

$$\left. - 2C_3 U_1 \arcsin\sqrt{\frac{u}{1+u}}\right\}. \tag{10}$$

Resulting distributions of potential and electric field intensity are shown on Fig. 2, here the blue line is the potential distribution and the red line is the electric field intensity.

SYNTHESIS OF THE DESIRED REFLECTOR'S POTENTIAL DISTRIBUTION

Physical synthesis of the field with a given distribution of the axial potential by setting the potentials of the field defining elements according to the above expression is impossible. The larger inner diameter of the ring electrodes defining the field leads to greater difference of the field on the axis from the ideal distribution.

To solve the problem of the reflector field distribution synthesis, we have developed software for calculating potentials of field defining elements. This software uses genetic optimization algorithm and CUDA-accelerated library for Laplace equation solving. Each field distribution in population (a set of field defining potentials on electrodes) is being tested according to function of error minimization, the best specimens of the population are crossed and form a new generation. Functioning of the algorithm ends when the minimum error of the desired field structure synthesis is achieved.

Using the described software, we obtained the values of the field defining elements potentials, providing minimum synthesis error for the desired field distribution on the axis of the reflector. On the basis of the result set of potentials, two-dimensional distribution of the field inside the reflector was calculated, as well as the relative error of the synthesis on the axis and the periphery of the reflector. The two-dimensional potential distribution is shown in Fig. 3. The results of calculations are shown in Fig. 4.

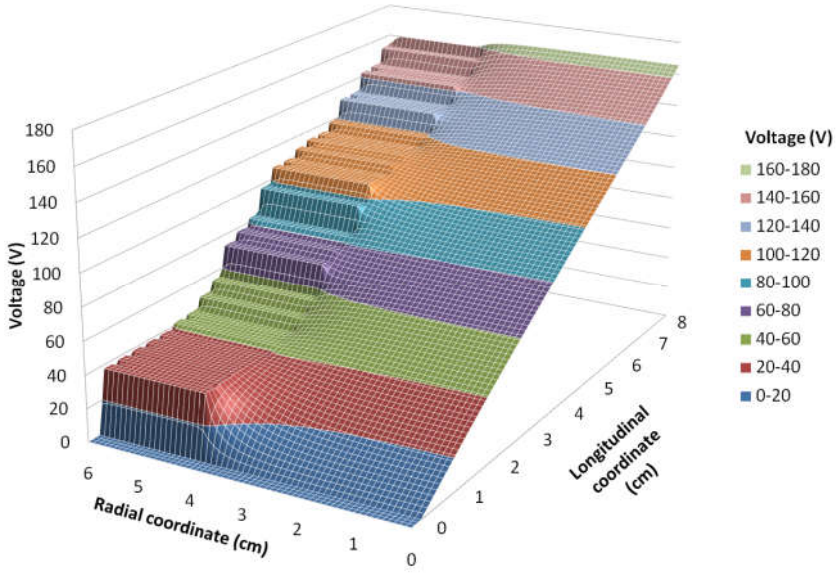

Figure 3. Potential distribution in the reflector

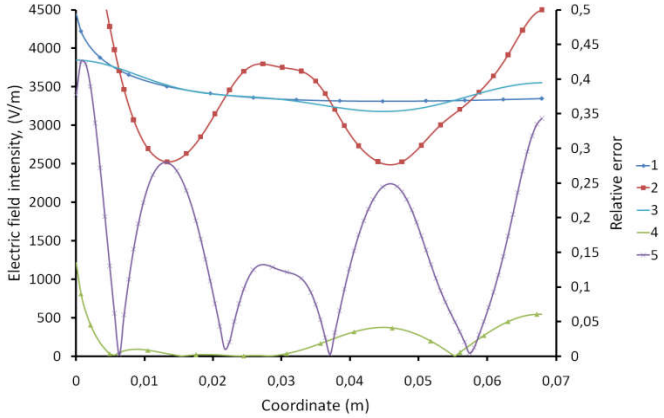

Figure 4. Electric field intensity and relative synthesis error: 1 – desired field, 2 – field on the axis of reflector, 3 – field on the periphery of the reflector, 4 – relative error on the axis of the reflector, 5 – relative error on the periphery of the reflector

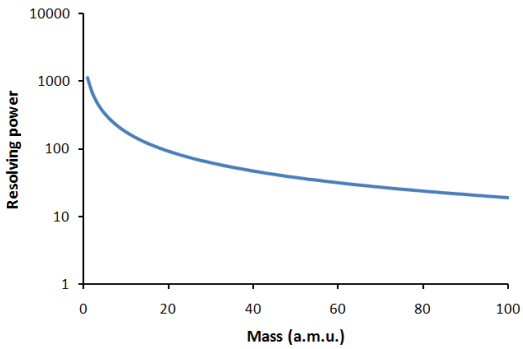

Figure 5. Dependency of the resolving power from the mass

IONS TRAJECTORIES SIMULATION AND DEVICE RESOLUTION

The ions trajectories were calculated using numerical Runge – Kutta integration method of fourth order. Maxwell velocity distribution in a given energy range is provided by using a special ion packets generator. The number of ions in the packet is selected based on the condition of smoothness of the velocities distribution. For each mass M_i mean time of flight was calculated:

$$T_{mean\ i} = \frac{1}{N}\sum_{j=1}^{N} T_j, \tag{11}$$

where T_j – individual ion in packet time of flight.

Root mean square deviation is determined according to the expression:

$$G_{T_i} = \sqrt{\frac{1}{N}\sum_{j=1}^{N}\left(T_j - T_{mean}\right)^2}. \quad (12)$$

And the resolution by sigma:

$$R_{G_i} = \frac{T_{mean\ i+1} - T_{mean\ i}}{2G_{T_i}}, \quad (13)$$

where G_{Ti} – root mean square deviation.

On the basis of the time of flight for the initial energy spread of 60 eV, the resolution from mass dependency was calculated, it is shown in Figure 5. Also dependence of resolving power from the radial coordinate of impact and initial energy spread of ions was calculated, which is shown in Table 1.

CONCLUSION

The results allow us to confirm the applicability of the described approach to the design of dust-impact time of flight mass spectrometers for space research with relatively high resolution (for a given accelerating voltage 250 V) in a wide range of initial energy spread of ions and impact coordinate. A further increase in resolution is possible by increasing the accelerating voltage (and thus reduce the relative energy spread of the ion packets), or by introduction to the design of the instrument of various modifications, such as additional compensating decelerating gaps and focusing ion lenses.

Table 1. Dependence of resolving power from the radial coordinate of impact and initial energy spread of ions

Radial coordinate of impact, mm	Initial energy spread, eV			
	15	**30**	**45**	**60**
0	1122	515	471	515
10	949	529	618	721
20	352	379	196	153
30	100	107	36	31

REFERENCES

1. Langevin, Y., Hilchenbach, M., Ligier, N., Merouhane, S., Hornung, K., & the COSIMA team (2015). Typology of dust particles collected by the COSIMA mass spectrometer in the inner coma of 67P/Churyumov Gerasimenko from Rendez-Vous to perihelion. *EPSC Abstracts, vol. 10*, 591–592.
2. Kempf, S., Altobelli, N., Briois, C., Grün, E., Horanyi, M., Postberg, F., Schmidt, J., Srama, R., Sternovsky, Z., Tobie, G., & Zolotov, M. (2014). SUDA: A dust mass spectrometer for compositional surface mapping for a mission to europa. *EPSC Abstracts, 9*, 229–230.
3. Hornung, K., Malama, Y. G., & Kestenboim, K. S. (2000). Impact vaporization and ionization of cosmic dust particles. *Astrophysics and Space Science, 274*(1–2), 355–363. doi:10.1023/A:102655350
4. Karataev, V. I., Mamyrin, B. A., & Shmikk, D. V. (1971). The new principle of ion packets focusing in time of flight mass spectrometry. *Zhurnal Tekhnicheskoi Fiziki, 41*(7), 1498–1501.
5. Kartaev, V. I., Mamyrin B. A., Shmikk, D. V., & Zagulin, V. A. (1973) The mass-reflectron, a new nonmagnetic time-of-flight mass spectrometer with high resolution. *Sov. Phys. – JETP, 37*(1), 45–48.
6. Sternovsky, Z., Amyx, K., Bano, G., Landgraf, M., Horanyi, M., Knappmiller, S., Robertson, S., Grün, E., Srama, R., & Auer, S. (2007). Large area mass analyzer instrument for the chemical analysis of interstellar dust particles. *Workshop on Dust in Planetary Systems*, September 26–30, 2005, Kauai, Hawaii, 205–208.

7. Austin, D. E., Ahrens, T. J., & Beauchamp, J. L. (2002). Dustbuster: a compact impact-ionization time-of-flight mass spectrometer for *in situ* analysis of cosmic dust. *Review of Scientific Instruments, 73*(1), 185–189. doi:10.1063/1.1427762

8. Rodin, D. V., Semkin, N. D., Piyakov, I. V., & Pomelnikov, R. A. (2012) Analytical method for computing the electrostatic field distribution in the reflector of the time-of-flight mass spectrometer. *Technical Physics, 57*(10), 1400–1405. doi:10.1134/S1063784212100192

Experimental Study of the Re-Emission During Thin Film Etching in the Outside the Electrodes Discharge Plasma

V. Podlipnov [1,2], V. Kolpakov [2]

[1] Image Processing Systems Institute of RAS – Branch of the FSRC "Crystallography and Photonics" RAS
E-mail: podlipnovvv@ya.ru
[2] Samara National Research University
Samara, Russia

Received: 28.11.2016

Abstract. The article presents the results of Cr-SiO_2 structure of the etching plasma high-voltage gas discharge in CF_4 + O_2 medium at a discharge current of 80 mA, voltage 1.2 kV and duration of the bombardment of the surface under study and 5-minutes. Detected sputtering deposition products within the windows in the mask in the chromium mode 1.2 kV, 80 mA. The deposited products formed a coating of vertically oriented pyramidal clusters. The images of scanning electron microscopy (SEM) are represented. Results of a study of the Raman spectra are presented. The results showed that the deposited film is a kind of compounds Cr_2NO_x.

Keywords: diffusion, ion-electron beam particles, annealing, pickling, reprecipitation, chromium, metal mask, chromium nitride, chromium oxide

INTRODUCTION

For a given topology semiconductor materials in microelectronics and micro-relief diffractive optical elements (DOE) plasma etching is widely used [1]. Previously, the authors in [2–4] has been shown to be promising application outside the electrods high-voltage gas discharge plasma in the process of etching processes.

As the masking layer during the formation of micro-relief methods of plasma chemical etching wide application of metal masking thin films [5] In the process of etching the metal mask is irradiated with plasma. Interaction of reactive plasma components with masking layers, can affect the quality of the structures formed. It is also known that the products of plasma-chemical reactions may be deposited on the treated surfaces that may have a positive effect on the result of [6], and is negative. Previous authors effect was observed plasma chemical deposition reactions to products treated surfaces. However, a detailed study of plasma-chemical reactions occurring in the etching of silicon dioxide in outside the electrode plasma using chrome mask was carried out. In this connection, in this paper, experimental studies of plasma-chemical deposition processes, and research products of plasma chemical reactions, resulting in a film of non-volatile compounds, deposited on the substrate surface.

EXPERIMENTAL TECHNIQUE

As the initial substrate were chosen fused silica, diameter of 25 mm and a thickness of 3 mm. The thin chromium film on the substrate was deposited by magnetron sputtering to a thickness of 40–60 nm. Test pattern formed electron beam lithography using a scanning electron microscope (SEM) Carl Zeiss Supra 25, with device lithography Xenos Xedraw 2. This technique of lithography is described in [7]. On the surface of the chromium formed microrelief of the electron resist ERP-40. To create test structures for experimentation deposition products of plasma chemical reactions, have been formed rectangular windows measuring 30x70 mm. Chemical etching in a solution of cerium sulphate through the resistive layer, the window data has been transferred to the chromium layer. (Fig. 1).

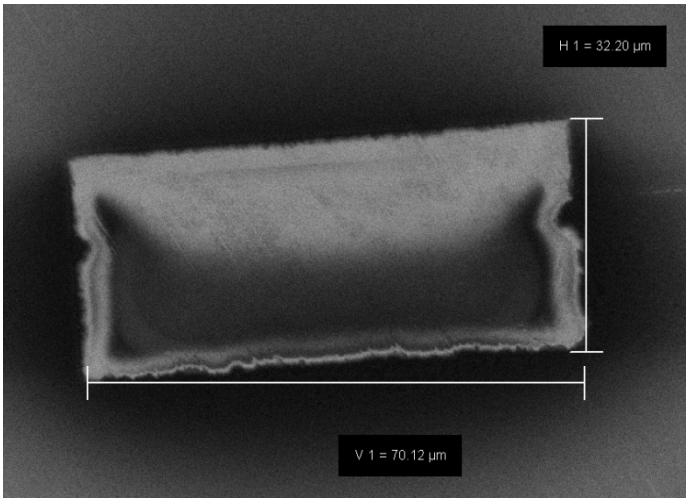

Figure 1. Cromium mask

Using this mask was carried out plasma etching of silicon dioxide on the outside of the electrode plasma modes: discharge current, I of = 50–80 mA, supply voltage U = 1200 V. As a generator electrode is used plasma source described in [8–9]. The experimental setup is shown in Fig. 2.

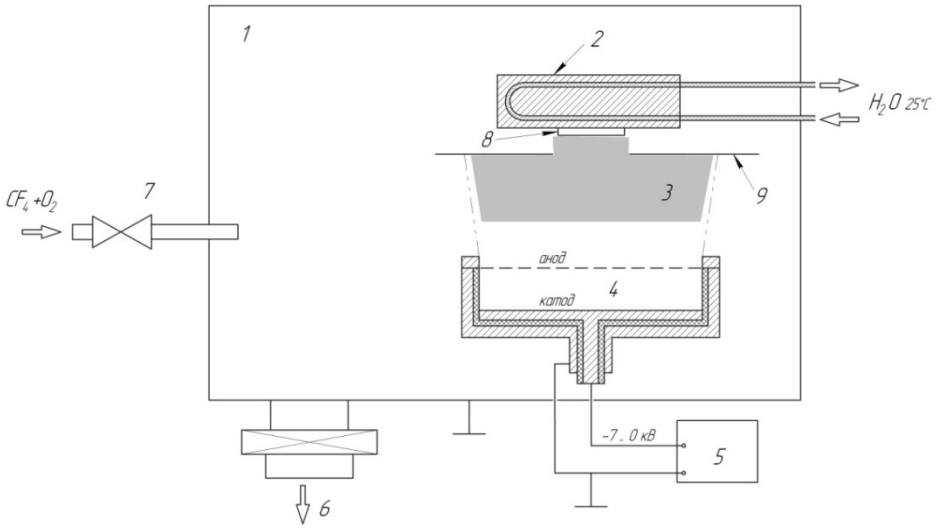

Figure 2. The experimental setup for the etching of microstructures: 1 – vacuum chamber; 2 – water-cooled substrate holder; 3 – the region of formation of low-temperature plasma; 4 – wide-source is an electrode of the plasma; 5 – high voltage power supply; 6 – redundant system pump; 7 – inlet system of working gas; 8 – substrate; 9 – screen.

Samples (position 8 in Fig. 2) were placed in a vacuum chamber 1, and a water-cooled substrate holder fixed in 2, the temperature in the etching process is maintained in the range 23–26 °C. The vacuum chamber was evacuated to a pressure source 10^{-4}–10^{-2} torr. The operation was performed 20–25 Pa inclusion of the plasma source 4, forming stream 3. To eliminate excessive heating of the substrate holder used the screen 9 from the window dimensions 35 × 35 mm. Large window sizes allowed to eliminate the edge effects and to obtain in the substrate plasma stream with a uniform particle distribution over its cross section is not less than 98 %. In the experiment using the plasma source anode mesh has a diameter of 110 mm, cell size of 1.8 mm, non-uniform flow field in the etching better than 2 %.

In operation, the mode used: I = 80 mA current, accelerating voltage U = 1.2 kV, duration of the bombardment of the sample surface 5 minutes.

The surface of the test sample was subjected to bombardment of negative plasma particles with an energy of 1.2–2 keV, 80 mA and a duration of 5 minutes. The composition of a mixture of $CF_4 + O_2$ in a ratio of 50 as the working gas: 1.

Control properties of thin films before and after plasma treatment was carried out using Ntegra Spectra Solaris NT-MDT in Raman spectroscopy mode using a laser with a wavelength of 532 nm, 10 mW. CCD is cooled to -50 °C Peltier temperature to reduce thermal noise when recording spectra. The accuracy of the range of ±2 cm^{-1}.

RESULTS AND DISCUSSION

Exploring the plasma etching, it was found that the deposition of plasma chemical etching products within the rectangular windows, the view of which is shown in Fig. 3.

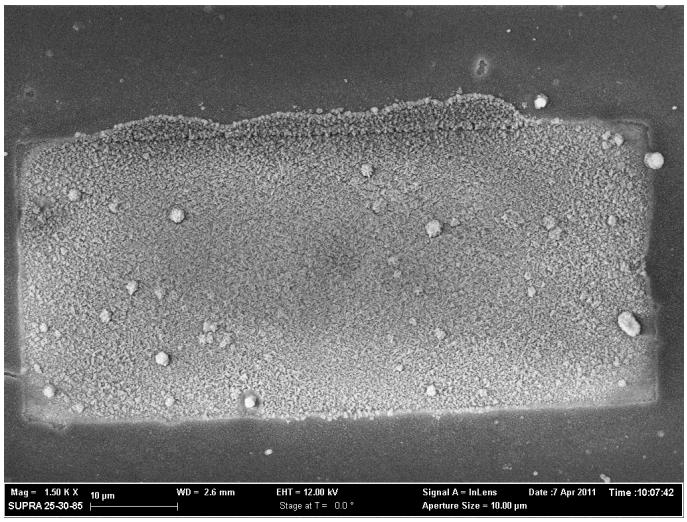

Figure 3. Deposition of etching products in the windows on the surface of the mask of silicon dioxide

Precipitated structure is a densely packed pyramidal crystallites whose shape is shown in Fig. 3. Furthermore, in the image (Fig. 3) can be seen on the long sides of the rectangle is "creeping" masking over chromium in the corners of the rectangle crystallite growth significantly smaller crystallite orientation that characterizes the process of growth in the center of the window towards the edges of the chrome. This configuration of the crystallite growth may be explained by the peculiarities of the distribution of the electric field generated as a result of treatment. The open surface of the quartz inside the open window is charged, and the metal film is removed effectively accumulating surface electric charge in the etching process. Negative surface charge in this case pushes or significantly reduces the kinetic energy of the plas-

ma of electronegative component. Thus, the physical sputtering mechanism in this area is greatly reduced, without hindering the deposition of neutral particles and positive plasma between the electrodes at a voltage of 1.2 kV plasma source. This assumption is consistent with the phenomena occurring in the process of electron beam processing, as described in [10].

Raman spectrum is shown in Fig. 4, c. On this spectrum can be identified characteristic broad band maxima correspond to the values of the wave number 152, 225, 278, 343, 619 cm^{-1}. A substantial width of the spectral bands of the spectrum indicates a high degree of structure, amorphous and non-uniformity of the film, due to the implementation of the deposition on a substrate fixed on a water-cooled substrate holder.

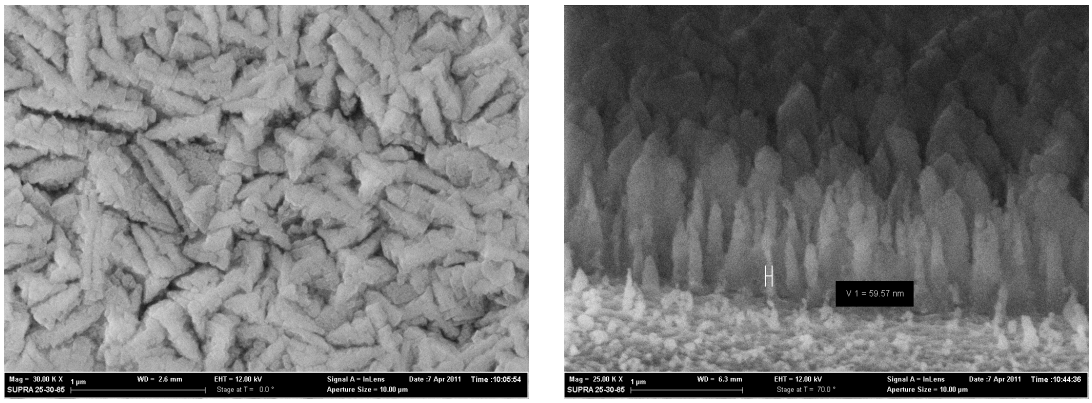

a b

c

Figure 4. The product crystallites deposited on the surface of silica reactions:
a – a top view, b – side view, c – Raman spectra of the deposited structure

A broad band with a maximum of 152 cm^{-1} is correlated with the corresponding peak in the spectrum of metallic chromium, the measured Raman spectrum is shown in Fig. 4.c. The wide bands with maxima 225, 278 cm^{-1} indicate the presence of compounds in the test Cr_2N film [11].

Maxima wide strips 619, 343 cm^{-1} correspond Cr_2O_3 weak maxima 615 and 350 cm^{-1} [12].

The form and nature of the location of spectral peaks as a whole allows us to say that the basis of the composition of the film lie kristallitovosazhdaemoy connection type Cr_2N, with minor amounts of nanocrystallites Cr_2O_3 [11]. Forming on the surface of larger globular structures (Fig. 3), it is also characteristic hexagonal Cr_2N chromium nitride lattice.

CONCLUSION

When the voltage to 1.2 kV in a metal mask windows is deposited reaction products. We studied the Raman spectra of the resultant structure, based on which it can be said that the main component of the crystallite deposited film is chromium nitride Cr_2NO_x.

ACKNOWLEDGMENT

The work was partially funded by Presidential grants for support of young Russian doctors of science (MD-5205.2016.9) and Russian Foundation of Basic Research Grants (project 16-07-00494 A).

REFERENCES

1. Donnelly, V. M., & Kornblit, A. (2013). Plasma etching: yesterday, today, and tomorrow. *Journal of Vacuum Science & Technology A: Vacuum, Surfaces, and Films, 31*(5), 050825. doi:10.1116/1.4819316
2. Kazanskiy, N. L., & Kolpakov, V. A. (2009). *Formirovanie opticheskogo mikrorel'efa vo vneelektrodnoy plazme vysokovol'tnogo gazovogo razryada [Study of optical microrelief formation in the plasma generated high-voltage gas discharge outside the electrode]* (220 p.). Moscow, Russia: Radio i Svyaz (in Russian).
3. Kolpakov, V. A., & Podlipnov, V. V. (2015). Mechanism of interaction between a directed beam of negative particles from a gas-discharge plasma and the melted nickel surface. *Technical Physics, 60*(1), 53–56. doi:10.1134/S1063784215010168
4. Kazanskiy, N. L., Kolpakov, V. A., Krichevskiy, S. V., Ivliev, N. A., & Markushin, M. A. (2017). A gas-discharge plasma focuser source of the document. *Instruments and Experimental Techniques, 60*(5), 748–751. doi:10.1134/S0020441217040157
5. Cheng, C. C., & Scherer, A. (1995) Fabrication of photonic band‐gap crystals. *Journal of Vacuum Science & Technology B: Microelectronics and Nanometer Structures Processing, Measurement, and Phenomena, 13*(6), 2696–2700. doi:10.1116/1.588051
6. Laerme, F., Schilp, A., Funk, K., & Offenberg, M. A. O. M. (1999). Bosch deep silicon etching: improving uniformity and etch rate for advanced MEMS applications. *Twelfth IEEE International Conference on Micro Electro Mechanical Systems (MEMS'99)*, Orlando, USA, 211–216. doi:10.1109/MEMSYS.1999.746812
7. Khonina, S. N., Nesterenko, D. V., Morozov, A. A., Skidanov, R. V., & Soifer, V. A. (2012). Narrowing of a light spot at diffraction of linearly-polarized beam on binary asymmetric axicons. *Optical Memory and Neural Networks, 21*(1), 17–26. doi:10.3103/S1060992X12010043
8. Kazanskiy, N. L., Kolpakov, V. A., & Podlipnov, V. V. (2014). Gas discharge devices generating the directed fluxes of off-electrode plasma. *Vacuum, 101*, 291–297. doi:10.1016/j.vacuum.2013.09.014
9. Kolpakov, V. A., Kolpakov, A. I., & Podlipnov, V. V. (2013). Formation of an out-of-electrode plasma in a high-voltage gas discharge. *Technical Physics, 58*(4), 505–510. doi:10.1134/S1063784213040130
10. Nikonorov, N. V., Sidorov, A. I., Tsekhomskii, V. A., Nashchekin, A. V., Usov, O. A., Podsvirov, O. A., & Poplevkin, S. V. (2009). Electron-beam modification of the near-surface layers of photosensitive glasses. *Technical Physics Letters, 35*(4), 309–311. doi:10.1134/S1063785009040063
11. Barata, A., Cunha, L., & Moura, C. (2001). Characterisation of chromium nitride films produced by PVD techniques. *Thin Solid Films, 398–399*, 501–506. doi:10.1016/S0040-6090(01)01498-5
12. Barshilia, H. C., & Rajam, K. S. (2004). Raman spectroscopy studies on the thermal stability of TiN, CrN, TiAlN coatings and nanolayered TiN/CrN, TiAlN/CrN multilayer coatings. *Journal of Materials Research, 19*(11), 3196–3205. doi:10.1557/JMR.2004.0444

The Electrical Schematic Diagram of Power Part and the Methods of Forming the Inverter Output Voltage

M. Pustovetov

Department of power management, automation and communications systems, Don State Technical University, Rostov-on-Don, Russia
E-mail: mgsn2006@rambler.ru

Received: 20.11.2016

Abstract. Author using computer simulation methods investigates characteristics of the device supply auxiliary circuits of dc electric locomotive in static mode. The electrical schematic diagram of power part of this device comprises a capacitive dc voltage divider, autonomous voltage source inverter, three-phase transformer with a particular connection scheme IIIy. Due to the use of construction of three-phase transformer with a single magnetic core must take into account the presence of strong electromagnetic coupling between the phases. To do this, used a mathematical model of three-phase transformer, allowing to get arbitrary schemes of winding connection, including all 12 standard phase displacement groups in a clockwise notation. The study presents results of a comparative review of the energy characteristics of the device at three methods to generate a regulated voltage at the output of the inverter. For example take into account the use of catenary voltage, efficiency, harmonic structure, the power factor. In the benefits of this study recommended control mode for transistors of the inverter.

Keywords: autonomous voltage source inverter; 3-phase transformer; mathematical model; phase displacement group; pulse-width modulation; efficiency

INTRODUCTION

Currently on a board of DC main electric locomotives are quite common electrical consumers feeding by three-phase and single-phase AC voltage. One of the problems to be solved in the development of devices for the needs of auxiliary circuits supply is to choose a method of catenary DC high voltage conversion in the low three-phase AC voltage. Some schematics for DC electric locomotives which based on two-level and three-level bridge-type circuits of autonomous voltage source inverter (VSI), including devices with a three-phase transformer, were published by experts from Europe and Japan [1, 2]. They have some of disadvantages. Usage the bridge-type two-level VSI with a minimum number of semiconductor switches (6 pieces) and the highest reliability is most common, but requires at a voltage of 3 kV catenary to use transistors with an operating voltage of 6.5 kV, which are expensive. Usage of three-level bridge VSI allows us to take advantage of more cheap power transistors with the value of the operating voltage of 3.3 kV, but at the cost of doubling their number and at more complicated control algorithms for VSI. The aim of this paper is to offer the device for feeding an auxiliary consumers onboard of DC electric locomotive which is based on three-phase

transformer and autonomous VSI, enabling use of a minimum number of relatively low-voltage power transistors with a simple wiring diagram.

THE ELECTRICAL SCHEMATIC DIAGRAM OF POWER PART OF DEVICE

Due to the best weight and size, it is advisable to use not three-phase group of single-phase transformers, but three-phase transformer with a single magnetic core, for example three-limb core. Offered scheme of the device involves independent (without electrical connection with each other, an open circuit) connection of phases of the primary winding of transformer to output terminals of inverter (see Fig. 1).

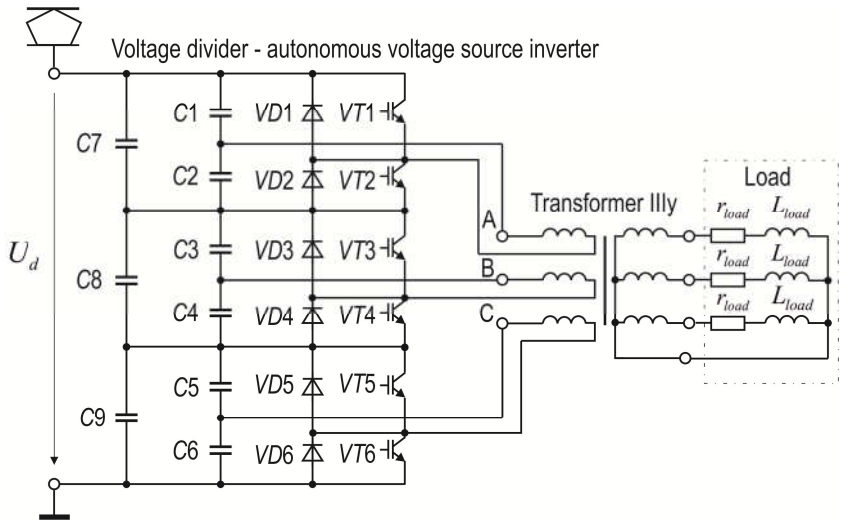

Figure 1. The electrical schematic diagram of power part
of the device supply auxiliary circuits of dc electric locomotive

The device in Fig. 1 converts DC voltage into three-phase alternating voltage, the frequency and magnitude of which can be adjusted. Each phase of the primary winding three-phase transformer is connected to the cell of converter. Each the cell is a single-phase half-bridge autonomous VSI. For example, phase A is connected to the cell that includes the transistor switches VT1 and VT2, diodes VD1 and VD2 and capacitors C1 and C2. Transistors VT1 and VT2 are opens alternately at equal time intervals, forming the alternating voltage on the phase A of primary winding of the transformer. Series-connected capacitors C7, C8 and C9 represent a capacitive divider that divides the input DC voltage of catenary in three equal parts (three is the number of phases of the transformer and number of cells of the converter). A pair of transistors in the other two phases work the same as in phase A, but shifted in time by 120° and 240°, forming on the windings of the transformer the three-phase symmetric system of supply voltages.

In accordance with [4] common connections for 3-phase transformers are recommended with vector groups 0, 1, 5, 6, 11 and additional connections with vector groups 2, 4, 7, 8, 10 (meaning the combination of the connection circuits of a D, Y, Z). Known three-phase transformer T-164 (Fig. 2) with the scheme and winding connection group Dyn7, wich designed for galvanic isolation and conversion of the channel of auxiliary circuit power supply unit voltage to voltage for auxiliary power consumers onboard of electric locomotive.

For the analysis of operation modes of the proposed device, it is expedient to use computer simulation tools. The simulator of a three phase transformer must be able to receive a standard group connection of windings in a clockwise notation [3], and use independent

connection of the windings to the voltage source and to take into account the strong magnetic connection between the phases of the transformer, assembled on a single magnetic core. The required properties of a simulator based on the equations given in [4]. These equations provide the ability to configure the model of transformer for any of 12 standard windings connection groups.

Figure 2. Three-phase transformer T-164 with the scheme and winding connection group Dyn7 for usage onboard of electric locomotive

For the analysis of operation modes of the proposed device, it is expedient to use computer simulation tools. The simulator of a three phase transformer must be able to receive a standard group connection of windings in a clockwise notation [3], and use independent connection of the windings to the voltage source and to take into account the strong magnetic connection between the phases of the transformer, assembled on a single magnetic core. The required properties of a simulator based on the equations given in [4]. These equations provide the ability to configure the model of transformer for any of 12 standard windings connection groups.

THE MATHEMATICAL MODEL OF THREE-PHASE TRANSFORMER WITH SINGLE MAGNETIC CORE

In compact form we can write the equations of the mathematical model of three-phase transformer as:

$$\begin{cases} v_{j1} - r_{j1} i_{j1} - L_{\sigma j1} \dfrac{di_{j1}}{dt} = v_{j01} \\ e_{j2} - r_{j2} i_{j2} = v_{j2}. \end{cases} \tag{1}$$

The system (1) is written for each phase of transformer. We denote the belonging to a certain phase as follows: $j = a, b, c.$ Additionally, we introduce the notation for the possible permutations of the phase indexes: $j-1 = c, a, b;\ \ j+1 = b, c, a.$

Let us describe the components of equations (1). EMF of primary winding and secondary windings of transformer, respectively.

$$e_{j1} = -\left(v_{j01} + L_{\sigma j1} \frac{di_{j1}}{dt} \right), \tag{2}$$

$$e_{j2} = \mp\left(\frac{w_2}{w_1} v_{j01} + L_{\sigma j2} \frac{di_{j2}}{dt} \right). \tag{3}$$

Here: v – phase voltage, V; i – phase current, A; L_σ – inductance of phase winding, H; r – active resistance of the phase winding, Ohm; w – number of turns in the phase winding. The index 1 indicates belonging to a primary winding of transformer, and index 2 – to the secondary.

For each phase, the voltage drop in the branches of the magnetization of the primary winding in a series connection in the branch of the main inductance L_m and resistance r_m, on which stand the iron losses is described by the expression:

$$v_{j01} = L_m(i_{\mu j}) \frac{2}{3} \left[\left(\frac{di_{j1}}{dt} + \frac{w_2}{w_1} \frac{di_{j2}}{dt} \right) - \frac{1}{2} \left(\left(\frac{di_{(j+1)1}}{dt} + \frac{w_2}{w_1} \frac{di_{(j+1)2}}{dt} \right) + \left(\frac{di_{(j-1)1}}{dt} + \frac{w_2}{w_1} \frac{di_{(j-1)2}}{dt} \right) \right) \right] +$$

$$+ r_m \frac{2}{3} \left[\left(i_{j1} + \frac{w_2}{w_1} i_{j2} \right) - \frac{1}{2} \left(\left(i_{(j+1)1} + \frac{w_2}{w_1} i_{(j+1)2} \right) + \left(i_{(j-1)1} + \frac{w_2}{w_1} i_{(j-1)2} \right) \right) \right] =$$

$$= L_m(i_{\mu j}) \frac{di_{\mu j}}{dt} + r_m i_{\mu j}, \tag{4}$$

where i_μ is the current in the branches of the magnetization phase of the transformer.

The "+" sign in the expression (3) corresponds to the case when the primary and the secondary coils which are located on the same one limb have the same direction of winding and similar location of the beginnings and the ends – inductors coupled positively. The sign "–" is used for the case of opposite direction of winding of the coils or change the beginning and end of one winding relative to another – inductors coupled negatively.

Using permutations of the phase indexes, we can write (4) as (5), and (3) as (6):

$$v_{j01} = L_m(i_{\mu j}) \frac{2}{3} \left[\left(\frac{di_{j1}}{dt} + \frac{w_2}{w_1} \frac{di_{(j+1)2}}{dt} \right) - \frac{1}{2} \left(\left(\frac{di_{(j+1)1}}{dt} + \frac{w_2}{w_1} \frac{di_{(j-1)2}}{dt} \right) + \left(\frac{di_{(j-1)1}}{dt} + \frac{w_2}{w_1} \frac{di_{j2}}{dt} \right) \right) \right] +$$

$$+ r_m \frac{2}{3} \left[\left(i_{j1} + \frac{w_2}{w_1} i_{(j+1)2} \right) - \frac{1}{2} \left(\left(i_{(j+1)1} + \frac{w_2}{w_1} i_{(j-1)2} \right) + \left(i_{(j-1)1} + \frac{w_2}{w_1} i_{j2} \right) \right) \right]; \tag{5}$$

$$e_{j2} = \mp\left(\frac{w_2}{w_1} v_{(j-1)01} + L_{\sigma j2} \frac{di_{j2}}{dt} \right). \tag{6}$$

Through the use of other permutations of the indices of the phases can also be written (4) to (7), and (3) to (8):

$$v_{j01} = L_m(i_{\mu j})\frac{2}{3}\left[\left(\frac{di_{j1}}{dt}+\frac{w_2}{w_1}\frac{di_{(j-1)2}}{dt}\right)-\frac{1}{2}\left(\left(\frac{di_{(j+1)1}}{dt}+\frac{w_2}{w_1}\frac{di_{j2}}{dt}\right)+\left(\frac{di_{(j-1)1}}{dt}+\frac{w_2}{w_1}\frac{di_{(j+1)2}}{dt}\right)\right)\right]+$$

$$+ r_m\frac{2}{3}\left[\left(i_{j1}+\frac{w_2}{w_1}i_{(j-1)2}\right)-\frac{1}{2}\left(\left(i_{(j+1)1}+\frac{w_2}{w_1}i_{j2}\right)+\left(i_{(j-1)1}+\frac{w_2}{w_1}i_{(j+1)2}\right)\right)\right]; \quad (7)$$

$$e_{j2} = \mp\left(\frac{w_2}{w_1}v_{(j+1)01}+L_{\sigma j2}\frac{di_{j2}}{dt}\right). \quad (8)$$

Matching equations, wiring diagrams, signs in front of the right part of the expression for the EMF of the secondary winding and vector group in the mathematical model of three-phase transformer summarized in table 1. Computer implementation the above-described mathematical model of three-phase transformer by means of PSpice [6] provides twelve terminals of the windings, thus achieving the possibility of its use in any connection diagram.

Table 1. Compliance in the mathematical model of three-phase transformer for various vector groups

Connection scheme of windings	**Yd, Dy**		**Yy, Dd**		**Yd, Dy**		**Yy, Dd**		**Yd, Dy**		**Yy, Dd**	
Rooms of expressions, describe the mathematical model	– (4)				(1), (2), (5), (6)				(1), (2), (7), (8)			
The sign in front of the right part of the expression for the EMF of the secondary winding	+	–	+	–	+	–	+	–	+	–	+	–
Winding vector group clockwise notation	11	5	0	6	7	1	8	2	3	9	4	10

METHODS OF FORMING OUTPUT VOLTAGE OF THE INVERTER

With the aim of making better use of the input DC voltage should be used the angle of conduction of the transistors $\Theta = 180°$ for the formation of the largest voltage across the primary winding of transformer. Thus, obtain the output voltage curve in the form of a meander. For regulation of the magnitude of alternating voltage is possible in this case to use the rectangular-triangular pulse width modulation (PWM): triangular bipolar carrier frequency voltage and the modulation voltage in the form of a meander (we shall call this "Method 1", see Fig. 3).

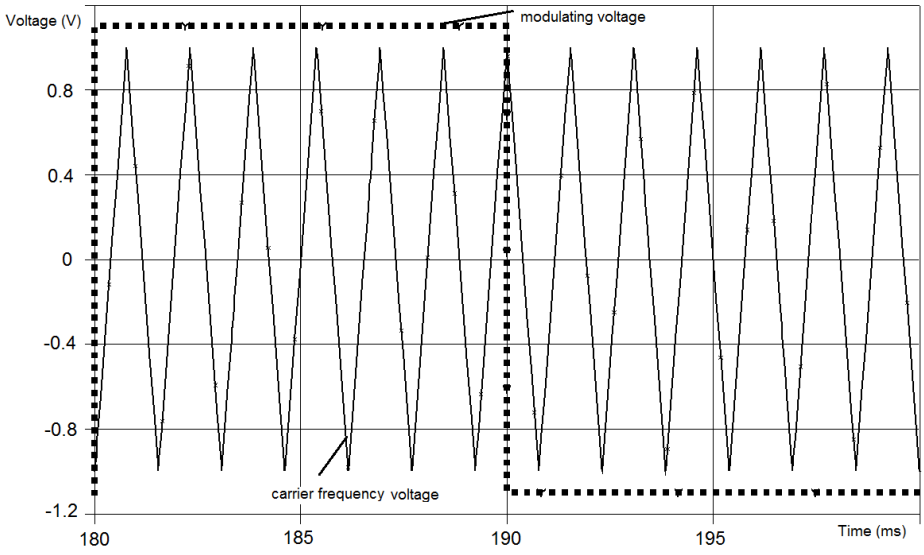

Figure 3. PWM in accordance with Method 1

The main disadvantage of the above mentioned method of forming the voltages (control method of the converter) follows from the harmonic composition of the signal shape of a meander: contains all the odd-order harmonic components, the relative amplitude of harmonics decrease inversely proportional to its number (relative amplitude of the 1st harmonic equals 1, the 3rd harmonic is 1/3, 5-th – 1/5). Third harmonic voltage is very high, which determines the magnitude of the third harmonic current of the primary winding of transformer (2.13 times higher than the 1st harmonic) and the significance of additional losses from its occurrence.

To overcome this drawback is proposed as a modulating voltage to use the signal form "meander with a pause" when the pulse width 120° (we shall call this "Method 2", see Fig. 4).

For comparison as the "Method 3" we'll use an algorithm of sine-triangle PWM with third harmonic having 0.167 relative magnitude from the first harmonic injection and the first harmonic overmodulation (see Fig. 5). The injected third harmonic is in-phase with the first.

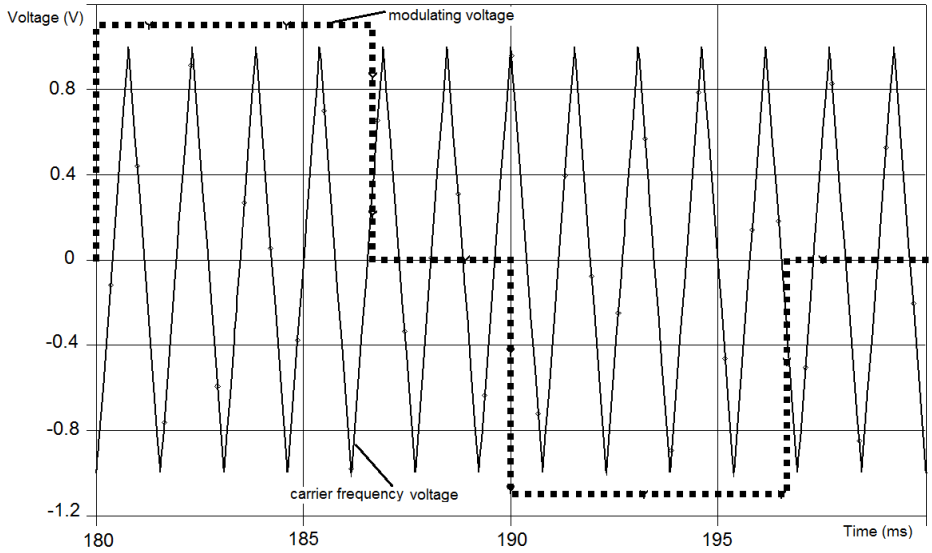

Figure 4. PWM in accordance with Method 2

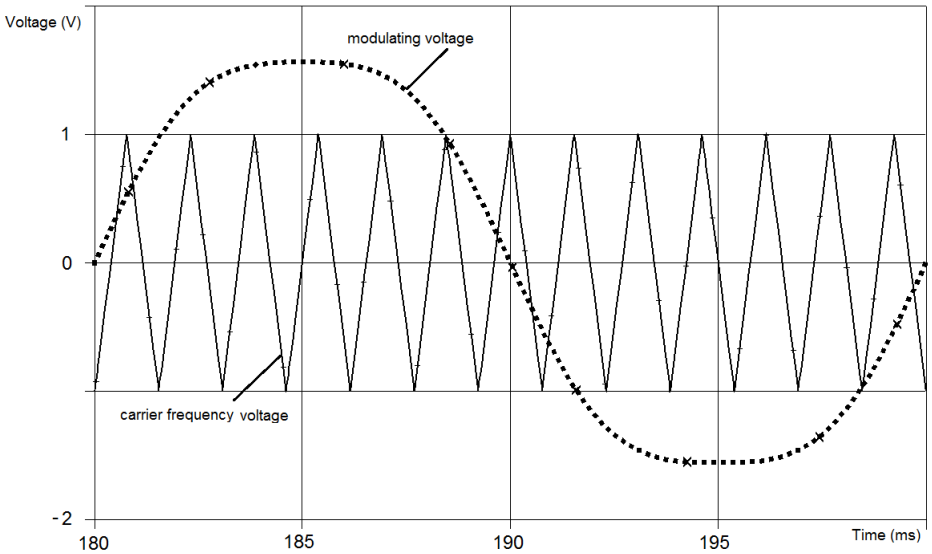

Figure 5. PWM in accordance with Method 3

The results of simulations for comparison of three methods of forming output voltage of the VSI are summarized in table 2. In all cases, the parameters of transformer and load are the same. The load is symmetrical. The frequency of the modulating voltage of 50 Hz, the carrier frequency of 650 Hz. All values in table 2 are presented in relative units.

If any of the considered methods do not exist or quite small the harmonics with order multiple of three in phase and phase-to-phase voltages of the secondary winding of transformer. This has a positive effect on the harmonic composition of the current in the secondary winding. The potential of the neutral point of the load (Fig. 1) is close to zero.

From the point of view the harmonic composition of currents and voltages generated by the converter, preferably, when the period of the modulating voltage is placed an odd number of periods of the voltage of the carrier frequency. Otherwise the currents and voltages will contain even harmonics (according to table 2 it has little effect on the energy characteristics of the electrical system).

Method 2 allows to drastically reduce the amount of current of the 3rd harmonic in the primary winding T (to 11.09 % from 1st harmonic).

In Method 3, the 3rd harmonic current in the primary winding of transformer is 150.62 % from 1st harmonic, which is lower than with Method 1, where 212.76 %.

The simulated curves of voltages and currents of the transformer are shown for Method 1 in Fig. 5, for Method 2 in Fig. 6 and for Method 3. – in Fig. 7, where the curves: 1 – phase voltage of the primary winding, 2 – phase current of the primary winding, 3 – phase current of the secondary winding, 4 – phase voltage of the secondary winding, 5 – inverted in sign phase-to-phase voltage of the secondary winding.

From table 2 it is seen that the highest value of the $\eta_T \cdot \cos\varphi_1$ demonstrates the Method 2. However, it is noticeably inferior to the other two methods by using the input voltage and, as a consequence, the active power at the load. Out on the set of power characteristics, that is, the value of the product $\eta_T \cdot \cos\varphi_1 \cdot \overset{*}{V}_{1phase}$ is preferable to Method 3.

Table 2. Comparative results of calculation of characteristics of the device for supply of three-phase and single-phase auxiliary circuits of DC electric locomotive with different methods of forming output voltage of the VSI

Name of characteristics	**1st harmonic of the phase voltage of primary winding of the transformer**	**Active power at output of the transformer**	**Power factor at input of the transformer**	**Efficiency of the transformer**	$\eta_T \cdot \cos\varphi_1$	–
The symbol	$\overset{*}{V}_{1phase}$	$\overset{*}{P}_2$	$\cos\varphi_1$	η_T	K_E	$\overset{*}{K_E \cdot V}_{1phase}$
When the carrier frequency is 650 Hz (voltage PWM based on 13 periods of carrier frequency for one period of the modulating)						
Method 1	1.000 (520.9 V)	1.000 (73.2 kW)	0.845	0.917	0.775	0.775
Method 2	0.859	0.759	0.829	0.970	0.804	0.691
Method 3	0.969	0.925	0.833	0.939	0.782	0.758
When the carrier frequency is 600 Hz (voltage PWM based on 12 periods of carrier frequency for one period of the modulating)						
Method 1	1.000 (518.7 V)	1.000 (73.0 kW)	0.847	0.910	0.771	0.771
Method 2	0.873	0.761	0.834	0.966	0.806	0.704
Method 3	0.966	0.925	0.825	0.961	0.793	0.766

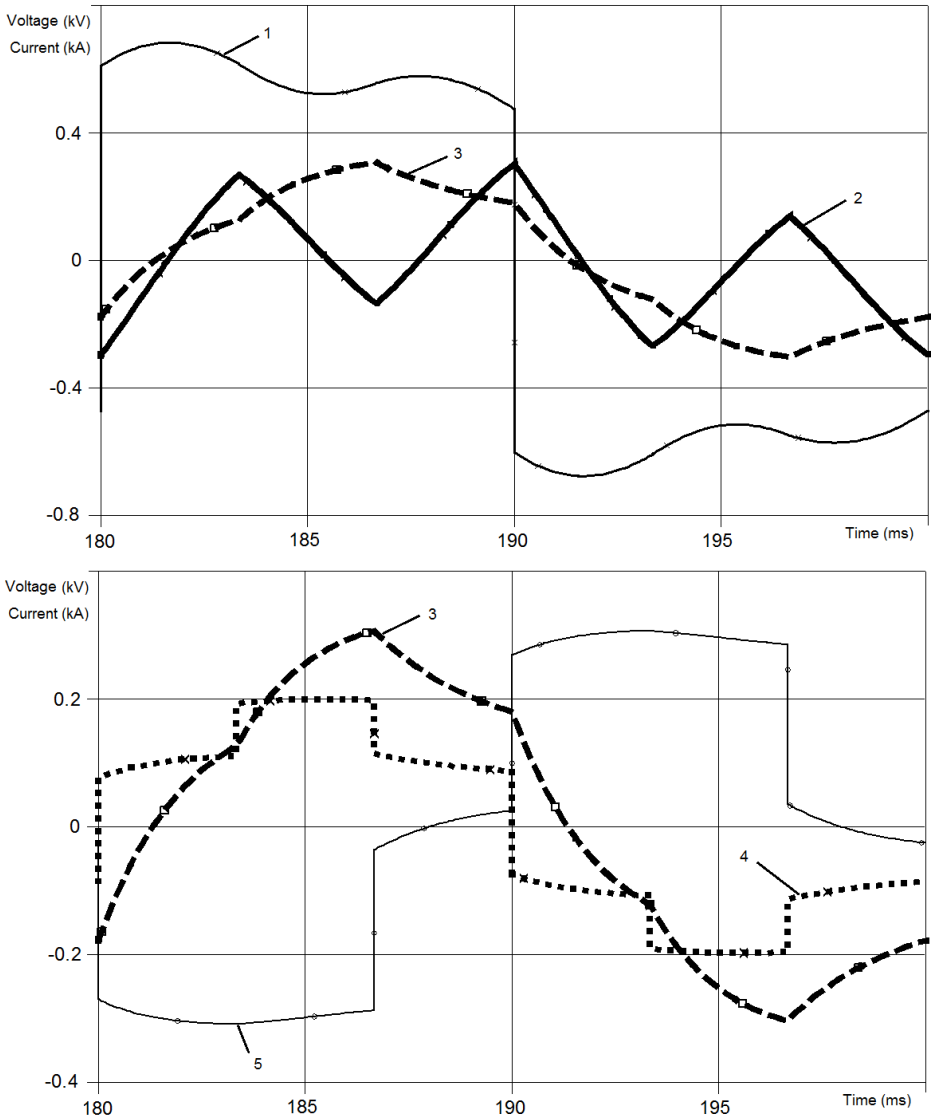

Figure 6. Voltages and currents of the transformer in case of control of the VSI according to the Method 1

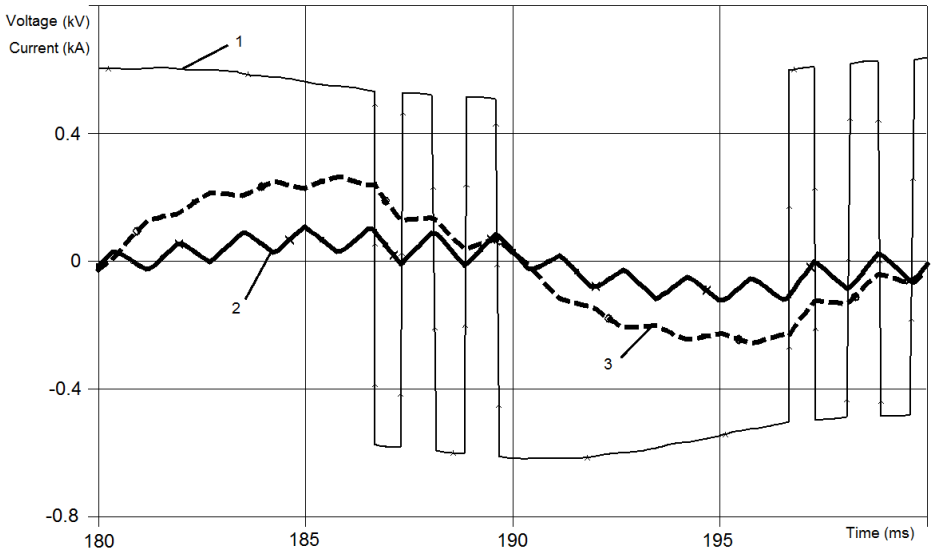

Figure 7. Voltages and currents of the transformer in case of control of the VSI according to the Method 2

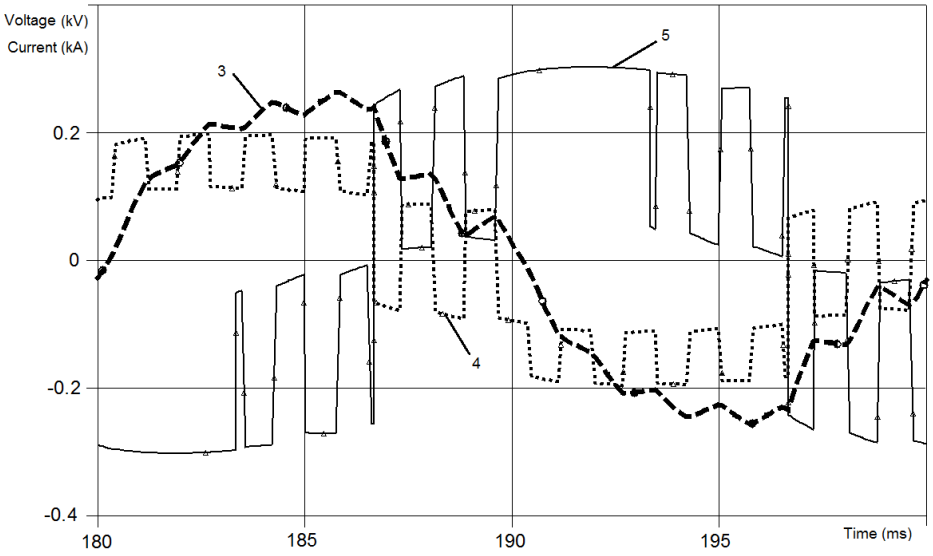

Figure 7 (continued)**.** Voltages and currents of the transformer in case of control of the VSI according to the Method 2

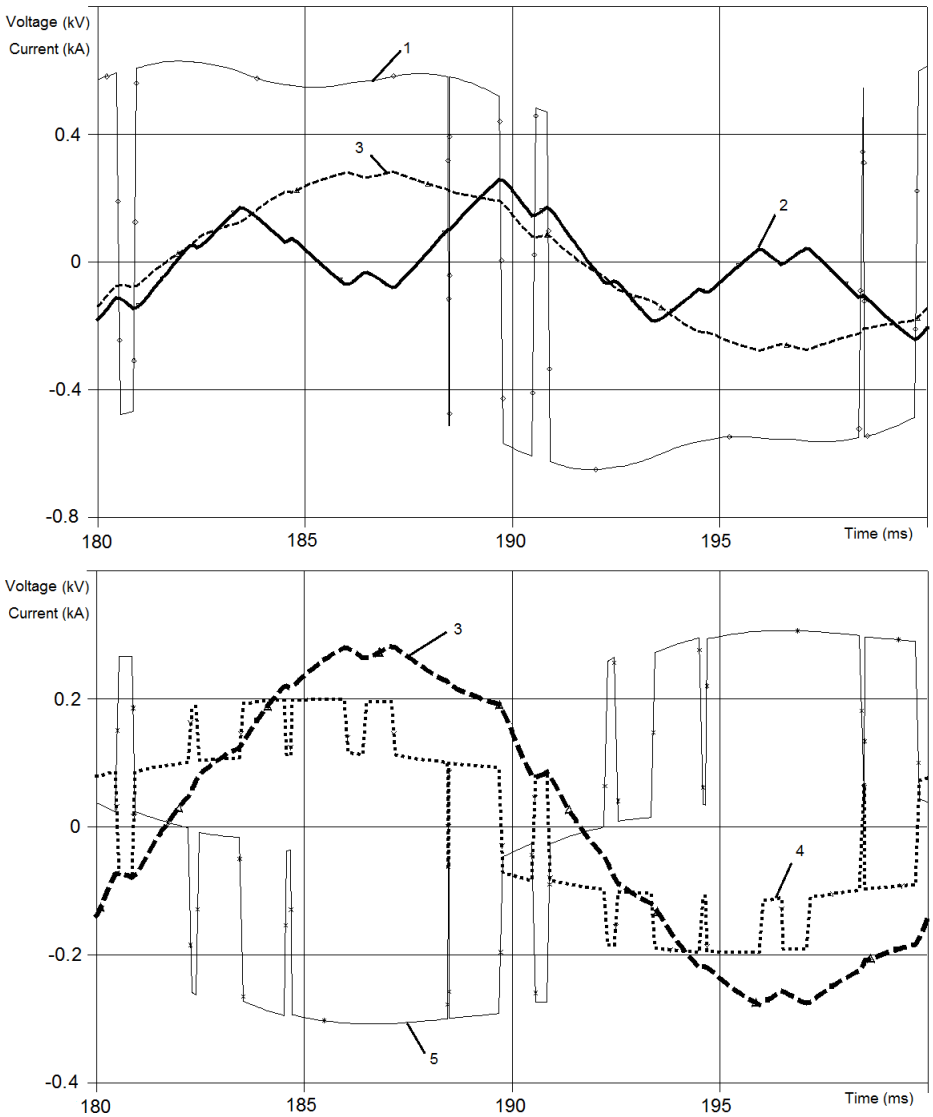

Figure 8. Voltages and currents of the transformer in case of control of the VSI according to the Method 3

CONCLUSION

The suggested scheme of power supply of auxiliary circuits of DC electric locomotive on the basis of the three-phase half-bridge autonomous VSI and three-phase transformer with winding connection scheme IIIy, with the following advantages: the number of power transistors is minimal, transistors with relatively low operating voltage, which reduces the device cost. The cost of the set of semiconductor switches can be reduced to 1.5–2.0 times in comparison with the known technical solutions.

Through a simulation using the original mathematical model of three-phase transformer is analyzed the methods of control of power switches. The best method for the totality of the energy characteristics and aspects of electromagnetic compatibility of suggested device recommended. Methods of forming output voltage of the proposed inverter does not differ from that used in known circuits. This allows to use technology of digital space vector PWM to control this VSI.

REFERENCES

1. Umezawa, K. (2012). Power electronic devices for railway vehicles. *Fuji Electric Review, 58*(4), 175–181.
2. Macan, M., Bahun, I., & Jakopovic, Z. (2011). Output DC voltage elimination in PWM converters for railway applications. *17th Int. Conference on Electrical Drives and Power Electronics (EDPE 2011)*, Stará Lesná, The High Tatras, Slovakia, 49–54.
3. Power Transformers – Part 1: General, IEC 60076-1.
4. Pustovetov, M. Yu. (2015). A universal mathematical model of a three-phase transformer with a single magnetic core. *Russian Electrical Engineering, 86*(2), 98–101. doi:10.3103/S106837121502011X
5. Keown, J. (2011). OrCAD PSpice and Circuit Analysis, 4th ed., New Jersey: Prentice-Hall Inc.

Application of a New Device for Diagnosing the Degree of Structure Degradation of Details from Nickel-Based Superalloy

M. Rigmant, N. Kazantseva, D. Davidov, D. Shishkin, V. Scherbinin

M. N. Miheev Institute of Metal Physics of Ural Branch of Russian Academy of Sciences,
Ekaterinburg, Russia
E-mail: davidov@imp.uran.ru; rigmant@bk.ru

Received: 17.11.2016

Abstract. The possibility of applying the magnetic methods of non-destructive testing discussed with regard to details from Nickel-based superalloys. The tests based of measurement of magnetic susceptibility performed with use of the new device with improved sensitivity. The severe deformation in turbine blade after exploitation led to the appearance of a strain-induced magnetism in initially paramagnetic alloy. The strain-induced magnetism associated with formation of ferromagnetic clusters inside of the particles of intermetallic phase. The obtained magnetic effect correlated with the dynamic stress level and the number of lattice defects in various parts of the blade.

Keywords: non-destructive test, magnetic properties, deformation, Nickel-based superalloy

INTRODUCTION

Superalloy EP-800 widely used in Russian power industry [1]. Structure of this alloy consists of the nickel solid solution, 40 % of the strengthening γ′-phase (intermetallic compound Ni_3Al) and a small amount of carbides (2 %). The intermetallic compound Ni_3Al is a weak ferromagnetic with a Curie temperature T_c = 41 K [2]. A deviation from stoichiometry or alloying lead to increases of Curie temperature [3], but at room temperature the Ni_3Al is paramagnetic. As a result, all phases of the alloy is paramagnetic at room temperature and retain this state during its further increase. For blades of the EP-800 alloy, whose upper level is 900°C, the working temperature, as a rule, is 800°C (*standard* regime) with operation time 27000 h. In the literature, there is no information that any superalloy changed its magnetic properties after the operation on the *standard* regime during the warranty period. Magnetic methods of nondestructive testing were not in demand for Nickel-based superalloys to date.

On the other hand, some intermetallic compounds, including Ni_3Al, known to exhibit strain-induced ferromagnetism, the phenomenon in which a paramagnetic intermetallic compound becomes ferromagnetic in part upon heavy deformation [4]. Practically superparamagnetic state observed. Since it revealed no formation of any new phases, the description of the strain-induced ferromagnetism performed using the term "magnetic cluster". Note that the above results obtained under cold deformation (for example, cold rolling). The only

observation of this effect in Nickel-based superalloy ChS-70 after high-temperature deformation is [5].

The appearance of ferromagnetic ordering in the initially paramagnetic alloy results from the formation of magnetic clusters inside the cuboids of the strengthening intermetallic phase (Ni_3Al). Changing magnetic susceptibility values can be detected by an original device for the magnetic susceptibility measurements named FERROCOMPAS which was developed by the authors. The previous device IMPAS developed in this research group is currently used in industry [6–7]. New device is compact, portable, has an improved sensitivity ($\pm 1 \cdot 10^{-4}$) and working with computer for processing the measurement results. It suitable to work with low magnetic (austenitic) materials, such as stainless steel [8]. The possibility of applying this device to a three-phase material was considered in [9]. In this article, the device FERROCOMPAS applies for another class of low magnetic materials, to Nickel-based superalloys.

In this article, the degree of structure degradation of the turbine blades made from Nickel superalloy EP-800 studied by structural and magnetic methods after long-time operation with increased temperature and level of dynamic stress.

EXPERIMENT

The study of structure and magnetic properties was carried out on as-cast polycrystalline blade from the superalloy EP-800 after operation at the stationary gas turbine of an industrial type with increased temperature from 800°C in *standard* regime up to 880 °C. Operation time was 9000 h with 17 turbine starts. The purpose of the experiment was to enhance the thermal efficiency and output capability of the power generation gas turbines (GTs). The main way of increasing power is to increase the operating temperatures and rotation speed [10-11].

The chemical composition of the investigated Ni-base superalloy given in Table 1.

Magnetic tests performed at room temperature using the FERROCOMPAS device for the magnetic susceptibility measurements. Processing of results performed using calibration samples. The vibrating magnetometer Lake Shore 7407 also used for measurements of the magnetization of the samples. Measurements performed at the frequency of 82 Hz. The amplitude of vibration was 1.5 mm; the relative error of measurement was not more than 1 %.

Studies of the fine structure made in the Test center of nanotechnology and advanced materials, Institute of metal physics UB RAS using a transmission electron microscope JEM-200CX, for X-rays microanalysis was used scanning electron microscope JSM 6490.

RESULTS AND DISCUSSION

After operating during 9000 h at the *experimental* regime (880°C), an increase in the magnetic susceptibility χ of blades material observed. The distribution of the magnetic susceptibility values on the surface of the turbine blade shown in Fig. 1.

The initial values of the magnetic susceptibility of superalloy EP-800 (before high-temperature deformation) was low: $\chi = 4 \cdot 10^{-4}$. The increase χ was different in different parts of the blade.

The maximum magnitudes were obtained for the convex feather part on its "back", in area where, as well known, temperature and the dynamic stress level were maximal [12]. The back of the feather is a narrow zone running along the axis of the feather on its convex side at the place of maximum curvature. Another critical place is the leading edge of the feather.

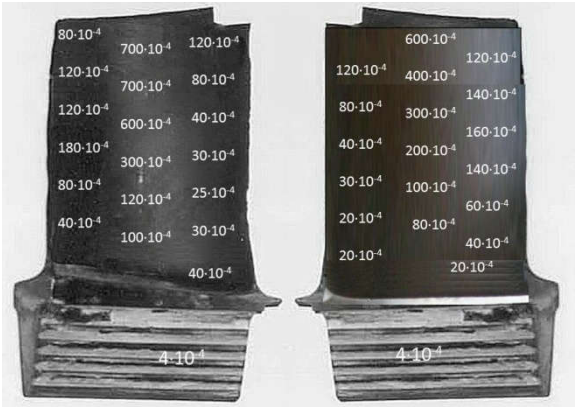

a b

Figure 1. Results of the magnetic susceptibility Measurement superimposed on the Photograph of the Blade from the both Sides: a – convex part; b – the concave part

In this case, we observe the phenomenon of deformation-induced magnetism after high-temperature deformation. This phenomenon is associated with intermetallic strengthening phase Ni_3Al, or rather with the formation of the stable defects complexes inside the γ′-phase particles. In the samples, which were cut from the convex part of the feather, the studies revealed a large number of defects in both the solid solution and in the intermetallic particles of γ′-phase (Ni_3Al) (Figure 2, a–b). The main defects were stacking fault defects within the deformed particles of intrermetallic γ′-phase (Fig. 2, c–d). The stacking faults were visible on the dark-field images. It proved that they belong to the strengthening intermetallic phase (superstructure stacking faults).

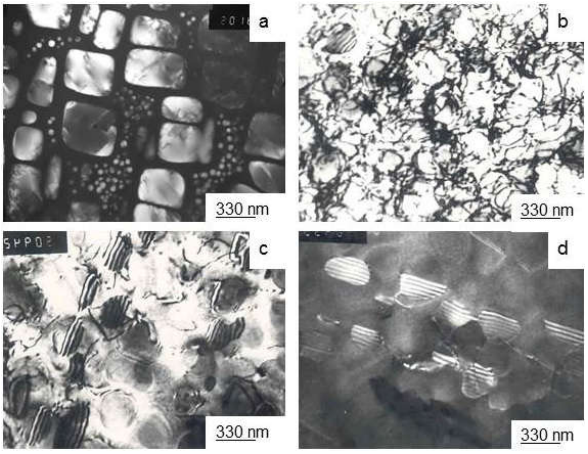

Figure 2. Structure of the different Parts of the turbine Blade after operation at 880°C for 9000 h: a – particles of intermetallic phases in the feather, dark-field image in the reflex of γ′-phase; b – high density of defects in the convex feather part on its back, the bright-field image; c, d – stacking faults inside the particles of intermetallic γ′-phase in the convex feather part on its back

In the locking turbine part, there were no defects inside γ′-particles and the only structural effect was a coagulation of intermetallic phase under heating (Fig. 3, a). The annealing of the deformed samples in a stepwise mode led to the restoration of defect-free state inside γ′-phase particles (Fig. 3, b).

Note that the electron microscopic analysis did not revealed formation of any new phase. The only phase transformation is carbide reaction when the carbide NbC replaced by carbide $(Cr, Mo, W)_{23}C_6$. These carbides are paramagnetic.

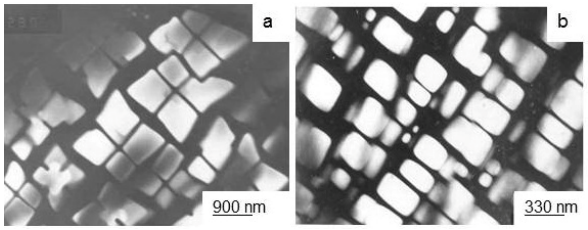

Figure 3. Intremetallic Phase, Dark-field Images in the Reflex of γ′-phase: a – locking part;
b – sample cut from the turbine blade after operation 880°C, 9900 h and reductive annealing in a stepwise mode

Thus, we see the correspondence between the number of the crystal structure defects in the various parts of the blade and the values of the magnetic susceptibility. Note the long-time operation of turbine blades from superalloys in the *standard* regime did not lead to the formation of stable defects complexes inside particles of the strengthening intermetallic phase. The defects located preferably in the solid solution. Such type of structure did not lead to the appearance of ferromagnetic properties of the paramagnetic alloy. Thus, magnetic cluster can be thought of as a complex of defects inside the intermetallic phase.

The formation of the stable defect complex inside the γ'-phase testifies of its softening. The properties of the intermetallic phase approach those of a solid solution, and the γ'-phase ceases to be strengthening component.

In this study magnetic susceptibility measurement performed directly on the blades without preliminary preparation of the surface that corresponds to the method of non-destructive magnetic testing.

The surface of blade was oxidized therefor it was necessary to trace the role of oxidation in the magnetic properties change. The high concentration of chromium (12.2 %) leads to the formation of the oxide Cr_2O_3 layer on the surface. This oxide is antiferromagnetic with low value of magnetic susceptibility. This is a protective oxide.

At first, it is necessary to establish whether there was a diffusion redistribution of alloying elements. The greatest interest to us is the area of the feather back, the place where the dynamic stress is maximal.

This zone is shown by hatching in Fig. 4 and this zone was used also for X-rays microanalysis of the alloy chemical composition. Statistical processing of data carried out according to results of measurements obtained in 12–16 points along lines marked as 1–3 at the scheme**.**

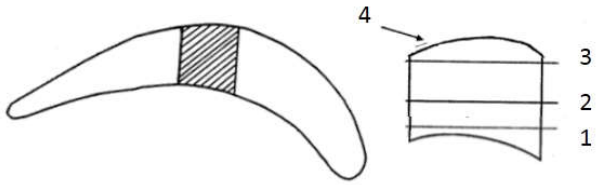

Figure 4. Scheme of X-rays microanalysis Zone on the feather cross Section

Table 1 shows the results of a study of possible redistribution of alloying elements in the alloy under the action of temperature and stress. It can conclude that the diffusion redistribution of chemical elements significantly suppressed with alloying. Our results obtained by X-rays microanalysis revealed of the redistribution of chemical elements only in two areas of the feather surface (4 at the scheme): near its back and leading edge.

Table 1. Chemical Composition of Alloy EP-800 according to the Specification and the average Composition as determined on Specimen cut from the Feather (wt. %), Carbon ≤ 0.05 wt. %

Alloying element	Cr	Mo	W	Al	Co	Nв	Ni	Fe
Specification	12.0–13.5	5.0-7.0	6.0-8.0	4.2-5.0	8.5-10.5	1.5-2.0	54.0-60.0	≤1
1	12.2	6.0	7.1	4.5	9.5	2.2	57.6	1.1
2	11.9	6.8	7.7	4.2	9.1	2.3	56.7	1.0
3	12.3	6.4	7.4	4.4	9.6	2.2	56.5	1.0

Table 2. Chemical Composition of the oxide Layer on the external Surface (4 at the Scheme)

Alloying element	Cr	Mo	W	Al	Co	Nв	Ni	Fe	O	C
Oxide layer on the feather	12.6	3.7	6.5	4.1	3.3	2.2	51.1	5.6	5.2	7.9
Oxide layer on the back of the feather	4.6	3.6	1.3	7.2	3.2	2.3	43.6	6.2	13.5	16.8

It the oxide layer there was an increase in the iron concentration from 1 % up to 6 % (iron was not an alloying element and presented as an impurity) together with the decrease in the chromium content from 12.2 % down to 4.6 %. It led to the formation of ferromagnetic iron oxides. As a result, places of the blade the most prone to stress were a subject to surface corrosion. The formation of ferromagnetic iron oxide is both a contribution to the increase of the magnetic susceptibility, and the evidence of the degradation of the structure as a demonstration of diffusion under stress.

The structure degradation is real because the increases in operating time at the *experimental* regime led to the emergency destroy of the blade after 9390 h (13 months).

The independent magnetic measurements held using a vibrating magnetometer Lake Shore 7407. The measurement by vibrating magnetometer conducted by certified methods on verified device, but this method of study was destructive. The experiment carried out on the samples in the form of thin plates (0.3 mm). They were the workpiece parts of foils for the electron microscopy described above. Samples cut in such a way that they do not include oxidized surface.

Field dependence of the specific magnetization $M(H)$ is representing in Fig. 5. The results were consistent with a previous experiment: the values of magnetic susceptibility increased in the convex feather part of the blade after operation 880 °C, 9000 h and the field dependence of magnetization represents a curve with saturation for the same sample.

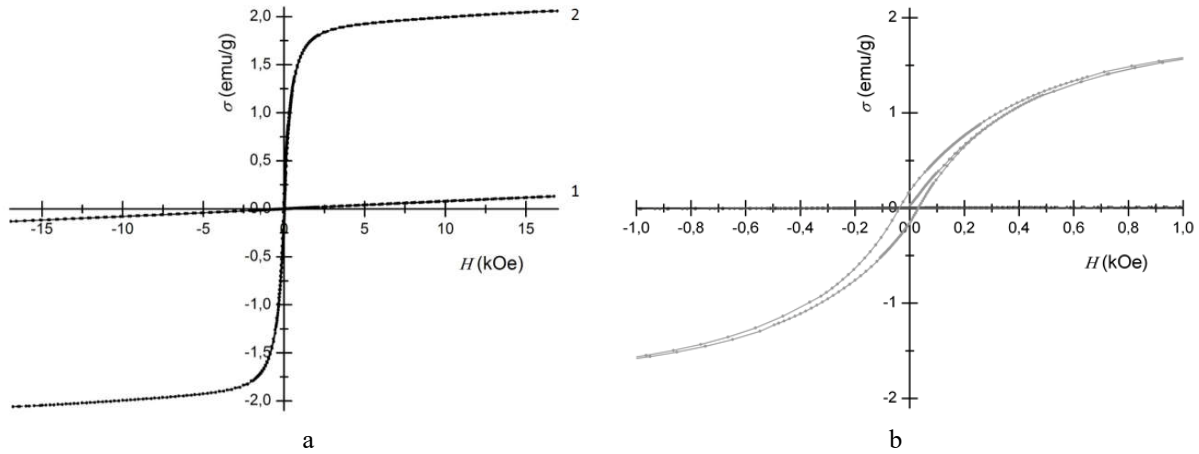

Figure 5. for Samples cut from different Parts of the turbine Blade after operation 880 °C, 9000 h: a – field dependence of the specific magnetization $M(H)$: 1 – locking part; 2 – convex feather part on its back; b – the same curve $M(H)$ on a larger scale

Hysteresis also observed, but the hysteresis loop is very narrow, suggesting the formation of super-paramagnetic state. In Fig. 5, b hysteresis loop shown for the sample cut from the blade on a different scale.

CONCLUSIONS

It is found that the initially paramagnet superalloy EP-800 acquires some ferromagnetic properties after long-time exploitation with increased operation temperature and rotation speed. The obtained magnetic tests results correlate with the dynamic stress level and the number of lattice defects in various parts of the blade.

The surface oxidation can be an additional factor of the magnetic susceptibility increase due to iron oxide formation by the diffusion under stress.

Both of these factors, and the formation of defects inside the particles of the strengthening intermetallic phase, and the formation of ferromagnetic oxides on the surface of the feather, at the same time indicate degradation of the structure.

A measurements of the magnetic susceptibility by the improved sensitivity device allow detecting the structure degradation and lead to use the magnetic nondestructive testing methods for evaluating the output capacity of turbine blades.

ACKNOWLEDGMENT

The research supported by the grant from the Russian Science Foundation No. 15-12-00001.

REFERENCES

1. Maslenkov, S. B. (1983). *Heat-resistant steels and alloys. Reference book of Technical regulations* (192 p.) Moscow: Metallurgy Press.
2. De Boer, F. R., Schinkel, C. J., Biesterbos, J., & Proost, S. (1969). Exchange-enchanced paramagnetism and weak ferromagnetism in the Ni_3Al and Ni_3Ga phase; Giant Moment Inducement in Fe-Doped Ni_3Ga. *J. Appl. Phys., 40*, 1049–1055. doi:10.1063/1.1657528
3. Abhyankar, A. C., Semwal, A., & Kaul, S. N. (2008). Effect of off-stoichiometry and site disorder on the properties of Ni_3Al: II. Magnetics. *J. Phys.: Condens. Matter., 20*, 445228. doi:10.1088/0953-8984/20/44/445228
4. Zeng, Q., & Baker, I. (2007). The effect of local versus bulk disorder on the magnetic behavior of stoichiometric Ni_3Al. *Intermetallics, 15*, 419–427. doi:10.1016/j.intermet.2006.08.010
5. Stepanova, N. N., Davidov, D. I., Nichipuruk, A. N., Rigmant, M. B., Kazantseva, N. V., & Vinogradova, N. I. (2011). The structure and magnetic properties of a heat-resistant nickel-base alloy after a high-temperature deformation. *The Physics of Metals and Metallography, 112*(3), 311–317. doi:10.1134/S0031918X11030288
6. Rigmant, M. B., Gorkunov, V. S., & Pudov, V. I. (2000). *A method of measuring ferromagnetic phase in the austenitic steels.* The patent for the invention No. 2166191, bull. 5(I), 23.
7. Rigmant, M. B., Nichipuruk, A. P., Khudyakov, B. A., Ponomarev, V. S., Tereshchenko, N. A., & Korkh, M. K. (2005). Instruments for magnetic phase analysis of articles made of austenitic corrosion-resistant steels. *Russian Journal of Nondestructive Testing, 41*(11), 701–709. doi:10.1007/s11181-006-0021-8
8. Rigmant, M. B., Korkh, M. K., Davydov, D. I., Shishkin, D. A., Korkh, Yu. V., Nichipuruk, A. P., & Kazantseva N. V. (2015). Methods for revealing deformation martensite in austenitic–ferritic steels. *Russian Journal of Nondestructive Testing, 51*(11), 680–691. doi:10.1134/S1061830915110030
9. Korkh, M. K., Rigmant, M. B., Davydov, D. I., Shishkin, D. A., Nichipuruk, A. P., & Korkh Yu. V. (2015). Determination of the phase composition of three-phase chromium–nickel steels from their magnetic properties. *Russian Journal of Nondestructive Testing, 51*(12), 727–737. doi:10.1134/S1061830915120049

10. Scobie, J. A., Teuber, R., Sheng Li, Y., Sangan, C. M., Wilson, M., & Lock, G. D. (2015). Design of an improved turbine Rim-Seal. *J. Eng. Gas Turbines Power, 138*(2), 022503. doi:10.1115/1.4031241

11. Tsukagoshi, K., Muyama, A., Masada, J., Iwasaki, Y. & Ito, E. (2007). Operating status of uprating gas turbines and future trend of gas turbine development. *Mitsubishi Heavy Industries. Technical Review, 44*(4), 1–6.

12. Sun, F., Tong, J., Feng, Q., & Zhang, J. (2015). Microstructural evolution and deformation features in gas turbine blades operated in-service. *Journal of Alloys and Compounds, 618*, 728–733. doi:10.1016/j.jallcom.2014.08.246

The Results of Testing of Lossless Compression Algorithm Based on Cascade Fragmentation Method and Ordering Pixels Sequence

V. Smirnov [1], A. Korobeynikov [2]

[1]Dept. Software, Kalashnikov Izhevsk State Technical University, Izhevsk, Russia
E-mail: drolbs@gmail.com
[2] Dept. Software, Kalashnikov Izhevsk State Technical University, Izhevsk, Russia
E-mail: kav33@inbox.ru

Received: 25.11.2016

Abstract. The present paper describes testing the algorithm based on methods of cascade fragmentation and ordering pixels sequence. The test images were borrowed from the sample images database available on University of Southern California site. All images were divided into 4 groups. Each group featured images of certain class and size. Testing was done at the following algorithm parameters: with variable sizes of image fragments (5×5, 6×6, 16×16); with variable number of ordering methods (bypass methods) applied to fragment's pixels (16, 32, 64, 128, 256). Test results were represented as average, minimum, maximum and variance compression ratio. It was shown that average compression ratio can be increased by 4.7 % for some groups of images and compression algorithm parameters. Moreover, cascade fragmentation was found to have other advantages over "snake" image bypass.

Keywords: lossless image compression, compression algorithms testing, cascade fragmentation, ordering pixels sequence, optimal bypass, code book

INTRODUCTION

All of image compression algorithms can be classified into two groups: 1) the bypass of image pixels matrix and obtaining the ordered pixels sequence (array); 2) the transformation of image matrix; transformation results are bypassed subsequently.

The methods of image bypass [1–4] generally come down to simple bypass methods; in particular, "snake" bypass is applied to JPEG images. At this bypass, the value of each subsequent pixel is predicted from previous values. Regardless of complex predictors, a simple method of pixels matrix bypass is used. In most cases delta-coding (the first finite difference) is applied as predictor. For transformation purposes, Fourier discrete transform [5] as well as wavelet transform is commonly employed [6].

In the previous paper [7] the authors proposed cascade splitting of an image into multiple fragments of fixed size. Then, finding optimal bypass trajectory was considered which was

thought to result in greater compression ratio compared to traditional "snake" bypass. A more detailed theoretical description of the tested algorithm can be found in papers [7–9].

ORDER AND RESULTS OF TESTING

The present research was aimed at developing a beta software version for image compression and comparing the results of compression with and without the use of cascade fragmentation and bypass optimization. The following parameters are assumed variable at testing: image fragment size; the number of ordering methods (bypasses) applied to fragment's pixels. Delta-coding is used as predictor. To compress the prediction error (modulo) Huffman's method is applied [1].

The developed method was tested on sample test images [10] taken from the site of *University of Southern California* on their *Signal and Image Processing Institute* page. The following images were tested: 2.1.01...2.1.12, 2.2.01...2.2.24, 4.1.01...4.1.08, 4.2.01...4.2.07.

In order to understand the efficiency of this or that compression mode, the tested images were divided into 4 groups based on the following criteria: size and class of an image. Thus, the first «2.1.*.*tiff*» and the second «2.2.*.*tiff*» groups represent aerial photographs of 512×512 and 1024×1024 pixels size respectively. The third «4.1.*.*tiff*» and the fourth «4.2.*.*tiff*» groups are photographs of 256×256 and 512×512 size respectively. Additionally, the general result for all images was provided. Each group was tested at the following bypass parameters: without cascade fragmentation and optimization ("snake" bypass) and with cascade fragmentation and bypass optimization [7]. The examples of free parameters of compression algorithm included fragment sizes at *nxn* splitting and the number of fragment bypasses *{k}*: 5×5 {824}, 6×6 {22144}, 16×16 {16}, 16×16 {32}, 16×16 {64}, 16×16 {128}, 16×16 {256}. The 16×16 fragment was limited reagrding the number of its bypasses with the view of saving on compression time and the expenses of coding the bypass number.

Test results are shown in tables 1…4 with average, minimum, maximum, and variance compression ratio represented by groups of images and compression types respectively. Similarly, the test results by compression time are given in tables 5…8.

Table 1. Average compression ratio of images

Groups of images	Average compression ratio							
	"Snake" bypass	**5×5 {824}**	**6×6 {22144}**	**16×16 {16}**	**16×16 {32}**	**16×16 {64}**	**16×16 {128}**	**16×16 {256}**
2.1.*.*tiff* 512×512	1.424	1.414	1.424	1.426	1.426	1.426	1.426	1.426
2.2.*.*tiff* 1024×1024	1.547	1.536	1.546	1.548	1.548	1.548	1.548	1.547
4.1.*.*tiff* 256×256	1.618	1.627	1.644	1.622	1.622	1.622	1.622	1.622
4.2.*.*tiff* 512×512	1.549	1.556	1.569	1.553	1.553	1.553	1.552	1.552
All images	1.539	1.531	1.542	1.540	1.540	1.540	1.540	1.540

Table 2. Minimum compression ratio

Groups of images	Minimum compression ratio							
	"Snake" bypass	**5×5 {824}**	**6×6 {22144}**	**16×16 {16}**	**16×16 {32}**	**16×16 {64}**	**16×16 {128}**	**16×16 {256}**
2.1.*.*tiff* 512×512	1.219	1.212	1.220	1.219	1.219	1.219	1.219	1.219
2.2.*.*tiff* 1024×1024	1.284	1.271	1.275	1.283	1.283	1.283	1.283	1.283
4.1.*.*tiff* 256×256	1.222	1.197	1.203	1.218	1.218	1.218	1.218	1.217
4.2.*. *tiff* 512×512	1.222	1.197	1.203	1.218	1.218	1.218	1.218	1.217
All images	1.219	1.197	1.203	1.218	1.218	1.218	1.218	1.217

Table 3. Maximum compression ratio

Groups of images	Maximum compression ratio							
	"Snake" bypass	5×5 {824}	6×6 {22144}	16×16 {16}	16×16 {32}	16×16 {64}	16×16 {128}	16×16 {256}
2.1.*.*tiff* 512×512	1.618	1.613	1.624	1.621	1.621	1.621	1.621	1.621
2.2.*.*tiff* 1024×1024	2.054	1.980	2.017	2.042	2.042	2.042	2.043	2.042
4.1.*.*tiff* 256×256	2.108	2.120	2.167	2.107	2.107	2.107	2.106	2.107
4.2.*.*tiff* 512×512	1.883	1.915	1.938	1.887	1.887	1.887	1.887	1.886
All images	2.409	2.463	2.510	2.423	2.422	2.422	2.422	2.421

Table 4. Variance image compression ratio

Groups of images	Variance compression ratio							
	"Snake" bypass	5×5 {824}	6×6 {22144}	16×16 {16}	16×16 {32}	16×16 {64}	16×16 {128}	16×16 {256}
2.1.*.*tiff* 512×512	0.016	0.016	0.017	0.017	0.017	0.017	0.017	0.017
2.2.*.*tiff* 1024×1024	0.027	0.026	0.029	0.026	0.026	0.026	0.026	0.026
4.1.*.*tiff* 256×256	0.081	0.089	0.097	0.081	0.081	0.081	0.081	0.081
4.2.*.*tiff* 512×512	0.049	0.058	0.061	0.050	0.050	0.050	0.050	0.050
All images	0.049	0.053	0.057	0.050	0.050	0.050	0.050	0.050

Table 5. Average image compression time

Groups of images	Average compression time							
	"Snake" bypass	5×5 {824}	6×6 {22144}	16×16 {16}	16×16 {32}	16×16 {64}	16×16 {128}	16×16 {256}
2.1.*.*tiff* 512×512	0:01:36	0:02:30	0:18:41	0:01:30	0:01:30	0:01:31	0:01:36	0:01:41
2.2.*.*tiff* 1024×1024	0:05:56	0:09:31	1:20:36	0:05:59	0:05:55	0:06:04	0:06:15	0:06:44
4.1.*.*tiff* 256×256	0:00:23	0:00:35	0:04:33	0:00:23	0:00:22	0:00:23	0:00:23	0:00:24
4.2.*.*tiff* 512×512	0:02:14	0:02:51	0:19:55	0:02:07	0:02:06	0:02:10	0:02:07	0:02:21

Table 6. Minimum compression time

Groups of images	Minimum compression time							
	"Snake" bypass	5×5 {824}	6×6 {22144}	16×16 {16}	16×16 {32}	16×16 {64}	16×16 {128}	16×16 {256}
2.1.*.*tiff* 512×512	0:00:56	0:01:56	0:18:11	0:00:52	0:00:52	0:00:53	0:00:59	0:01:02
2.2.*.*tiff* 1024×1024	0:03:46	0:07:52	1:17:03	0:04:13	0:04:10	0:04:15	0:04:26	0:04:42
4.1.*.*tiff* 256×256	0:00:18	0:00:31	0:04:29	0:00:20	0:00:19	0:00:20	0:00:20	0:00:22
4.2.*. *tiff* 512×512	0:01:36	0:02:35	0:19:32	0:01:47	0:01:44	0:01:47	0:01:46	0:01:58

Table 7. Maximum compression time

Groups of images	Maximum compression time							
	"Snake" bypass	5×5 {824}	6×6 {22144}	16×16 {16}	16×16 {32}	16×16 {64}	16×16 {128}	16×16 {256}
2.1.*.*tiff* 512×512	0:02:33	0:03:04	0:19:07	0:02:19	0:02:17	0:02:17	0:02:26	0:02:28
2.2.*.*tiff* 1024×1024	0:08:19	0:12:33	1:23:32	0:08:21	0:08:14	0:08:26	0:08:48	0:09:07
4.1.*.*tiff* 256×256	0:00:30	0:00:42	0:04:43	0:00:29	0:00:29	0:00:30	0:00:29	0:00:31
4.2.*.*tiff* 512×512	0:02:49	0:03:02	0:20:14	0:02:25	0:02:24	0:02:26	0:02:24	0:02:37

Table 8. Variance compression time

Groups of images	Variance compression time							
	"Snake" bypass	**5×5 {824}**	**6×6 {22144}**	**16×16 {16}**	**16×16 {32}**	**16×16 {64}**	**16×16 {128}**	**16×16 {256}**
2.1.*.*tiff* 512×512	1.025E-07	6.9E-08	4E-08	8.57E-08	8.34E-08	8.39E-08	8.87E-08	8.89E-08
2.2.*.*tiff* 1024×1024	7.286E-07	7E-07	2E-06	5.46E-07	5.21E-07	5.36E-07	6.01E-07	5.93E-07
4.1.*.*tiff* 256×256	2.134E-09	1.5E-09	3E-09	1.01E-09	1.22E-09	1.24E-09	1.06E-09	1.26E-09
4.2.*.*tiff* 512×512	1.009E-07	1.3E-08	4E-08	2.45E-08	2.53E-08	2.51E-08	2.29E-08	2.55E-08

ACKNOWLEDGMENT

The work was performed as part of the grant GZ/TVG-14(01.10)

CONCLUSIONS

1. Let us consider test results by groups of images. According to average compression ratio the fragmentation and optimization method proves more efficient compared to the "snake" method: 1) in group «2.1.*.*tiff* 512x512» by 0.2%; 2) in group «2.2.*.*tiff* 1024x1024» the results do not differ considerably; 3) in group «4.1.*.*tiff* 256x256» by 4.7%; 4) in group «4.2.*.*tiff* 512x512» by 2%; 5) generally, throughout all groups by 0.3%.
2. If the difference in compression ratio at variable fragment sizes is examined, the larger the fragment, the higher the compression ratio. However, compression time along with expenses of storing the bypass number in the code book increase parallel to fragment size.
3. Provided the number of chosen bypasses is reduced and the size of fragments is big enough, it is possible to obtain higher compression ratio at compression time matching that of "snake" bypass. Hence, the proposed algorithm enables adjusting compression efficiency.
4. Besides higher compression ratio the cascade fragmentation has the following advantages: it enables displaying/downloading posterized images; displaying/downloading particular fragments with improved quality as required; editing pixels of particular fragments without re-coding the whole image.

REFERENCES

1. Vatolin, D., Ratushnyak, A., Smirnov, M., & Yukin, V. (2003). *Metody szhatiya dannyh. Ustroystvo arhivatorov, szhatie izobrazheniy i video [Data compression methods. The archivers internal structure, images and videos compression]*. Moscow, Russia: DIALOG-MIFI, 2003.
2. Sayood, K. (2012). Lossless image compression. In *Introduction to data compression* (4th ed.) (pp. 183–215). University of Nebraska. doi:10.1016/B978-0-12-415796-5.00007-7
3. Karam L. J. (2009). Lossless image compression. In A. Bovik (Ed.) *The essential guide to image processing* (2nd Ed.) (pp. 385–419). Academic Press, Elsevier Inc. doi:10.1016/B978-0-12-374457-9.00016-0
4. Li, Z.-N., Drew, Mark, S., & Liu, J. Lossless compression algorithms (2014). In *Fundamentals of multimedia* (pp. 185–224). Springer, Cham. doi:10.1007/978-3-319-05290-8_7
5. Pennebaker, W. B., & Mitchell, J. L. (1992). *JPEG: Still Image Data Compression Standard.* Springer Science & Business Media.
6. Taubman, D., & Marcellin, M. (2001). *JPEG2000 Image Compression Fundamentals, Standards and Practice.* Springer Science & Business Media.

7. Smirnov, V., & Korobeynikov, A. (2016). Ordering the numeric sequence of image pixels at lossless compression. In *Instrumentation Engineering, Electronics and Telecommunications – 2015: Paper book of the I International Forum IEET-2015 held within the framework of the XI International Scientific-Technical Conference "Instrumentation Engineering in the XXI Century Integration of Science, Education and Production"*. Izhevsk, Russia: Publishing House of Kalashnikov ISTU. 175–180. Retrieved from http://pribor21.istu.ru/proceedings/IEET-2015/IEET-2015_Smirnov.pdf
8. Smirnov V. S., & Korobeynikov A. V. (2012). Opredelenie optimal'nogo obhoda s ispol'zovaniem kodovoy knigi pri szhatii izobrazheniy bez poter' [Optimal Bypass Definition with Code Book Application at Images Lossless Compression]. *ISTU bulletin, 2012*(2). 143–144.
9. Korobeynikov A. V., & Smirnov, V. S. (2012). Kaskadnoe razbienie izobrazheniya na fragmenty pri szhatii bez poter' na osnove optimizacii obhoda [Cascade Image Splitting into Fragments at Lossless Compression on Basis of Image Bypass Optimization]. *ISTU bulletin, 2012*(3). 114–115.
10. The USC-SIPI Image Database. (n.a.). Los Angeles, USA: University of Southern California. Retrieved from http://sipi.usc.edu/database/database.php?volume=misc

Efficiency Increasing of Laser Technologies Application for Identification of Art and Industrial Products

A. V. Usoltseva

Kalashnikov Izhevsk State Technical University, Izhevsk, Russia
e-mail: ajieksa_oo@mail.ru

Received: 23.12.2016

Abstract. The relation between properties of industrial products and individual characteristics of the laser technology production was researched. The analytical expressions for calculating of the depth of penetration of laser radiation into the material are derived in this paper; these expressions allow to increase the efficiency of laser technologies application, to choose optimal laser parameters, and to consider microstructure, chemical composition and mechanical properties of the material. The solution of topical problem of technological modes establishing is proposed, considering multiple versions of technology and laser equipment choices and considering indeterminacy of thermal properties of material. The complex index is distinguished, that index greatly simplifies selection of laser radiation parameters and allows to make atlas of materials thermal diffusivities.

Keywords: laser technology, engraving, material, thermal properties, art and industrial products, thermal diffusivity

INTRODUCTION

Nowadays laser marking and engraving are literally applied in all branches industry production, in instrument engineering, in identification and protection coding of the industrial models, in labeling of instrument panels, measuring tools, keyboard fields, in manufacturing of plates and signboards and in artistic decoration products. Development of scientific progress has increased necessity for esthetic improvement of all industrial production. Technique is one of the most important component of spiritual wealth, an organic part of the subjective world, and of the artificial environment of human life, its penetration is deeper and more extensive into all spheres of human life. That's why understanding of importance of harmonization of the richest and most complex world of subject forms and their relationship between each other come to the level of social objectives of the society, it's acquiring educational, ideological nature, increasing the importance of creating a comfortable in use, complete in form, esthetically perfect industrial products that meet both high technical and economic requirements, with a high degree of artistic expression.

The individual characteristics of each industrial product, independence of the author's intention, artistic taste, art of execution, disclosure of the artistic properties of the material like as its color richness, softness, and plastic are determining the dependence of the shape of the

art and industrial products from its purpose, determining the relationship between function and design solution, between form and design, material, production technology [1].

Currently, the expansion of functional possibilities of the instrument and the complexity of forms of products are take place, the detailing of the terrain is increasing, the surface geometry is becoming more complex, the original color solutions are offering, so high artistic expression of the finished product is achieving. But hand-made production process is extremely time consuming and requires a considerable amount of time, that's why the cost of hand-made products is high enough. Mechanical manual processing was replaced by automated one as a result of the development and improvement of high technologies. In its turn, the mechanical processing was replaced by the laser one [2]. Laser processing is more precise and has already became more cheap, it allows to make organic combination of design and industrial production.

Widespread in industrial production laser technologies [3] are rarely applied for identification imaging (bar codes, pictograms, numbers, etc.) to identifies the author, place and time of production, material composition, etc., due to additional requirements for esthetic properties, such as shape, pattern, texture and color, and the lack of proven methodologies. A number of theoretical and practical issues remain as insufficiently studied. In particular, the relationship between technological modes of laser equipment and surface characteristics of industrial products in the laser engraving is not studied. As usual, technological modes are establishing under the finished product experimentally. Current regulations ignore procedural issues that are related to the organization and the realization of an objective assessment of surface quality in engraving. Different definitions of terms create additional confusion and lead to the serious consequences, that are limiting wide application of laser technologies for wood processing.

The aim of this work is to study possibility of efficiency increasing of laser technologies application for identification imaging of artistic and industrial products of glass, ceramics, organic glass, plastic, metal and other materials by establishing of correlation and regression relationship between technological modes of laser equipment and surface characteristics of industrial products.

INFORMATION THEORY

There is a thermal separation process under the laser radiation to all kinds of materials, like the burning process. The thermal effect under the laser radiation is defined by the laser radiation parameters and thermal properties of material that depend from its microstructure [4].

As a result of thermal effect by the laser radiation, material begins to heat up. For example, there is only moisture remove by evaporation or boiling for organic materials at the temperature of 100...105 °C. When material is heated to the temperature of 105...150 °C, the drying process ends with the release of gaseous decomposition products. Material acquires a yellow and yellowish-brown color. The temperature increase in this stage occurs only due to action of external thermal energy source. At the temperature of 150...275 °C release of gases is intensifying and vapors of resinous substances are starting to release. Individual flares of gases are appeared at the temperature of 225...235 °C. Material is becoming darker, and its decomposition mainly proceeds only due to action of external thermal energy source. Decomposition of material with heat release (exothermic reaction) begins at the ignition temperature (about 275...290 °C), so a lot of flammable vapors and gases, gaseous products of pyrolysis are produced. If heating to such temperature does not occur, so material stops to burn after removal of the heat source. The described process is also suitable for industrial products of

organic glass, cloth, leather, glass, ceramic, stone. The separation process is similarly at other temperatures.

Based on the above, using the expressions given in [5], in case of the laser beam has a Gaussian profile, and the absorbed laser radiant flux surface density is constant and equal to F_0, the temperature distribution in the solid material and its change in time is described by the expression:

$$T(r,z,t)=\frac{d^2\chi^{1/2}F_0}{K\pi^{1/2}}\int_0^t\frac{\exp\left(\frac{-z^2}{4\chi t}\right)\exp\left[\frac{-r^2}{4\chi t+d^2}\right]}{t^{1/2}\left(4\chi t+d^2\right)}dt, \quad (1)$$

where F_0 is the absorbed laser radiant flux surface density in the center of the spot of exposure, [W/m^2]; r is the distance from the center of the heated spot, [m]; z is the depth of heating that counted from the surface of material, [m]; T is the temperature, [K]; χ is the thermal diffusivity, [m^2/s]; K is the thermal conductivity, [W/(m·K)]; t is the time interval from start of exposure to laser radiation, [s]; d is the diameter of the laser spot on the surface of material, [m].

To determine the temperature in material under the fixed and the same distance from the center of the heated spot and the depth of heating, that counted from the surface, considering that calculation of the integral, which integrand includes the exponential function, use the integration by substitution, the expression (1) will be transformed to the following one:

$$T(t)=\frac{F_0 d}{K\pi^{1/2}}\cot\left(\frac{4\chi t}{d^2}\right)^{1/2}. \quad (2)$$

As a result of representation of trigonometric function cot(x) as a series and using of the first three terms of this series, that introduces an error less than 5 %, but greatly simplifies calculations, there is obtained:

$$T(t)=\frac{F_0 d}{K\pi^{1/2}}\left[\left(\frac{4\chi t}{d^2}\right)^{1/2}-\frac{\left(\frac{4\chi t}{d^2}\right)^{3/2}}{3}+\frac{\left(\frac{4\chi t}{d^2}\right)^{5/2}}{5}\right]. \quad (3)$$

After using of the ratio for describing the relationship between the main laser radiation parameters and material properties [6], the expression, that determine the depth of penetration of the radiation into material, is obtained:

$$h=\frac{4P}{C_p\rho T\pi d^2}, \quad (4)$$

where P is the power of radiation, [W]; C_P is the heat capacity of material, [J/K]; ρ is the density of material, [kg/m^3]; h is the depth of penetration of the radiation into material, [m]; d is the radius of the laser spot on the surface of material, [m]; $T(t)$ is the temperature change of the material during the heating, [K].

Considering that the thermal diffusivity of non-metallic materials is about 10^{-8} m^2/s, the expression (3) can be limited to the first term, after substituting (3) into the expression (4), there is obtained:

$$h = \frac{2PK}{C_p \rho F_0 d \pi^{1/2} \chi^{1/2} t^{1/2}} \tag{5}$$

denoting $\frac{2K}{C_p \rho F_0 d \pi^{1/2} t^{1/2}}$ as γ, the depth is given by:

$$h = \frac{\gamma P}{\chi^{1/2}}. \tag{6}$$

DESCRIPTION OF THE EXPERIMENT

Since the thermal properties of materials depend from temperature nonlinearly, the halftone gray scale, (GOST 24930-81. Facsimile equipment gray scale. Technical requirements) was reproduced from white to black areas by the laser engraving machine of Speedy series of the Trotec company (Austria), with using of the CorelDraw and JobControl software, when the laser output power was being changed from 2 W to 12 W, the speed of movement of the laser beam was being changed from 10 cm/s to 180 cm/s, resolution was being changed from 100 dpi to 1000 dpi, pulse frequency was being changed from 500 Hz to 1000 Hz, the diameter of the focused laser beam on the material surface was being changed from 0.05 mm to 1.0 mm, the angle of incidence of the laser beam was being changed from 0 to 45 ° and these modes was being combinated, to check the correctness using of the expression (6) for the experimental determination of the depth of penetration of laser radiation into material. The experiments were being made by the reproduction of the halftone gray scale on wood of tangential, radial and end cut, on natural and artificial leather, and by the reproduction of the light and dark tones on bone, organic glass, Fig. 1.

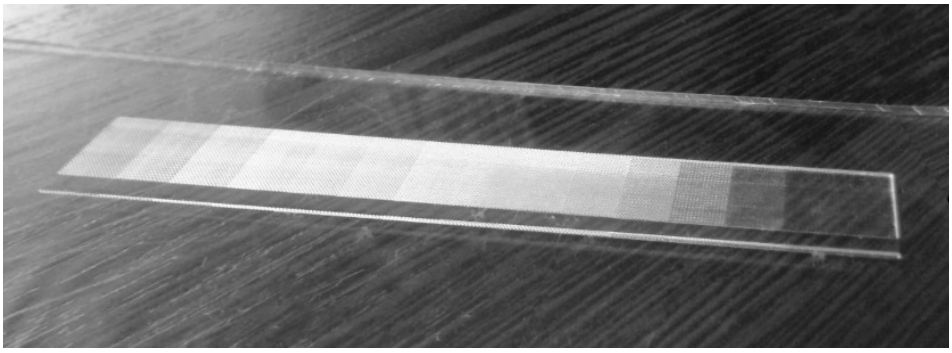

Figure 1. Reproduction of the halftone gray scale on organic glass

The depth of penetration of laser radiation into the material, obtained in the experiment and measured by the micro-interferometer MII 4, is presented as the function of the power of laser radiation in Fig. 2. Point curve presents the depth of penetration of the radiation into the material as the calculation result of expression (6).

Following that, the thermal diffusivity, as a physical quantity that characterizes the rate of temperature change of material in non-equilibrium thermal processes, allows to fully consider non-linear change of thermal properties of materials, that caused by changes of physical, mechanical, chemical, and esthetic properties of materials due to the heterogeneity of the microstructure, caused by volume uncertainty and multivariance of implementations of the characteristics of applied material.

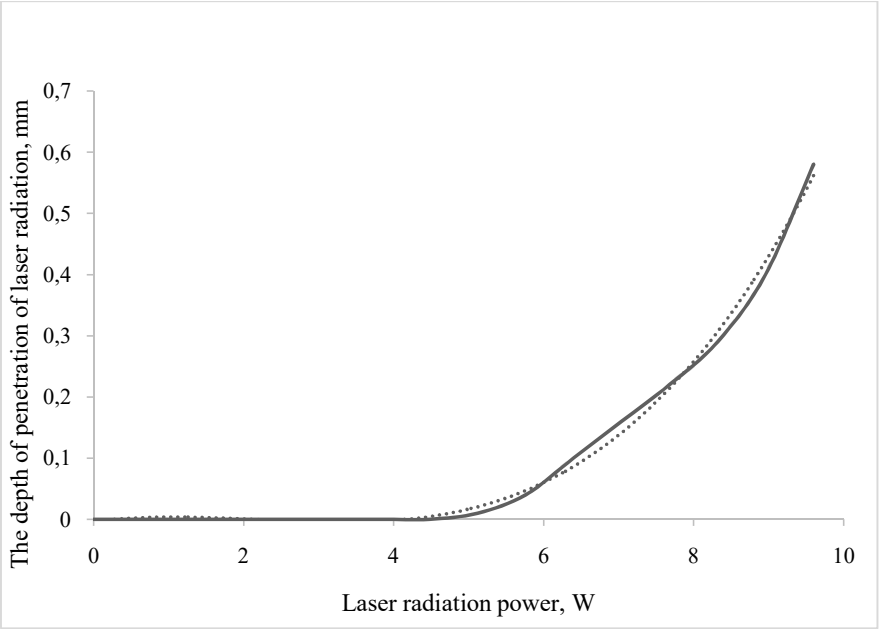

Figure 2. The estimated depth of penetration of laser radiation into the material (point curve) and obtained in the experiment one (solid curve)

RESULTS AND DISCUSSION

Highlighting of the complex index greatly simplifies the choice of laser radiation parameters, since it allows to create an Atlas of temperature diffusivities of materials as a set of rules for the location and naming of materials, that rules establish the order of arrangement of materials in accordance to temperature diffusivities of materials so the more similar material properties are, the closer materials should be located to each other, and establish method of indicating of the material location in the sequence of temperature diffusivities.

The using of the proposed Atlas will simplify the choice of numerical coefficients in the expression (6). As a result of mathematical calculations, analysis and expert survey it is obtained that the depth of penetration of laser radiation into the material of 0.3–0.5 mm is necessary for most sharp and clear image. This is enough to obtain a stable contour of cutting, high-contrast images and patterns, a necessary adhesion to stain the image. On the basis of the analytical function, there are next selected modes of laser system for imaging of the material [7]:

– the power of laser radiation of 8.32 W;
– the laser engraving speed of 18 cm/s;
– the resolution of 500 dpi;
– the pulse frequency of 1000 Hz;
– the diameter of the focused laser beam on the material surface of 0.1 mm;
– the angle of incidence of the laser beam 0°.

CONCLUSIONS

Thus, the theory and practice of laser material processing confirm the possibility of efficiency increasing of laser technologies application for identification imaging of artistic and industrial products of wood, natural and artificial leather, bone, glass, ceramics, organic glass, plastic, metal and other materials by considering of correlation and regression relationship between technological modes of laser equipment and surface characteristics of industrial products.

The practical significance of the work is determined by the developed proposals applicable to the solution of topical problems of establishing of individual modes of laser processing for the decorative processing of materials considering multiple versions of realization of technology modes and considering indeterminacy of specific properties of material. The proposed method allows to preserve the unique natural pattern, to successfully compensate the existing natural heterogeneity of material and to provide consistently high results in industrial production of high-artistic exclusive products.

REFERENCES

1. Norman, D. A. (1990). *The design of everyday things.* New York, USA: Doubleday/Currency.
2. Emmelmann, C. (1998). *Introduction to industrial laser materials processing.* Hamburg, Germany: Rofin-Sinar.
3. Panchenko, V.Ya. (Ed.) (2001). *Laser materials processing: User's handbook manual.* Plovdiv, Bulgaria.
4. Mazumder, J., & Steen, W.M. (1980). Heat transfer model for laser material processing. *J. Appl. Phys, 51*(2). 941–947. doi: 10.1063/1.327672
5. Gamaly, E. G., Rode, A. V., Luther-Davies, B., & Tikhonchuk, V. T. (2002). Ablation of solids by femtosecond lasers: Ablation mechanism and ablation thresholds for metal and dielectrics. *Physics of Plasmas, 9*(3). 949–957. doi:10.1063/1.1447555
6. Cain, S. R., Burns, F. C., Otis, C. E., & Braren, B. (1992). Photothermal description of polymer ablation: Absorption behavior and degradation time scale. *J. Appl. Phys., 72.* 5172–5178. doi:10.1063/1.351997
7. Zavestovskaya, I. N. (2012) Theoretical modeling of laser ablation of polymers. *32nd European Conference on Laser Interaction with Matter, September 10–14, 2012*, Warsaw, Poland: Institute of Optoelectronics, P-34.

Establishing of the Laser Engraving Modes for Decorative Processing of Glass Products

A. V. Usoltseva

Kalashnikov Izhevsk State Technical University, Izhevsk, Russia
e-mail: ajieksa_oo@mail.ru

Received: 23.12.2016

Abstract. The relationship between properties of industrial products and features of the laser processing technological modes are researched. The simulation model for execution of the laser engraving operating modes is developed. The analytical expressions, that show the relationship between the laser engraving modes and optical properties of glass and allow to increase the efficiency of laser technology application and to choose more suitable laser parameters considering microstructure, chemical composition and mechanical properties of material, are derived.

***Keywords*:** instrument engineering, glass, laser technology, engraving, optical properties, industrial products

INTRODUCTION

Glass is modern, functional and esthetic material that has a set of useful properties and natural beauty, so, thanks to that, the glass products are demanded in various spheres of human activity. Broad using of glass is caused by the unique and peculiar combination of physical and chemical properties, that combination is not typical to any other material. Glass is widely applied in industrial production, medicine, aircraft and astronautics, construction, holography, trading, advertising, decoration works, etc.

The application of glass is plural depending on its properties: in instrument engineering glass is applied in variable and constant capacitors, in self-induction coils, in vacuum devices, for the production of substrates for micro-modules of printed circuit boards, small capacitors, high-voltage and high-frequency insulators, devices with ultraviolet radiation, light cells , optical fibers of computers, glass fibers, optical filters, including variable transmission filters, films, for example, glass films that have thickness of 5–100 microns are applied for insulation of electric machines. Glass is applied for production of protective glasses for devices' protection from mud, mechanical damage, dust and liquids under the ambient temperatures of -60 till +60 °C.

Because of low mechanical durability, fragility, presence of internal tension and high requirements to a surface, drawing texts, images, barcodes, scales, limbs, etc., has certain difficulties. Laser processing including laser engraving and laser cutting gives to glass products high appeal. Thanks to creation of reliable and rather economic laser equipment in the 70–80th of 20th century, laser technology of materials processing had appeared as a new indus-

trial technology. That allows to change flexibly the images on a product surface with the maximum using of material without readjustment.

Laser engraving has a number of great advantages in comparison with other types of imaging such as cutting, grinding, cutting, abrasive-jet, chemical, ultrasonic, arc, electric arc and ion engraving.

Laser engraving doesn't require high qualification of personnel, it allows to perform contactless processing of billets, so that allows to minimize the internal thermal-mechanical tensions, to reach the smooth and stable contour of cutting, the high-artistic contrast dark look of images, the minimum rounding radius of angles of cutting (0.1–0.3 mm) and gives a chance of simultaneous engraving and cutting of material, so that decrease the positioning error and the additional processing. At the same time new design properties of an engraving which not to reach machining or other types of an engraving turn out, and completely digital chain of processes of production with high precision of repeating is created, thanks to virtual process of display, visual representation of structures is reached in three-dimensional space. Production of special templates of structures is performed by using of the graphical software. By scanning of the available samples and by its transferring to gradation of gray, the laser imaging and other types of imaging can be combined, the simplified application of combined materials to products and the direct imaging of complex three-dimensional structures are possible with high efficiency and high performance of production and minimum costs of time for starting of new production [2].

Widespread in industry production laser technologies are applied rarely for engraving of glass due to lack of approved methods of selecting of processing modes. The high investment costs for a robotic laser engraving machine require achieving of a higher consumer qualities of a new design of an art-industrial product to prove these investments. Since laser engraving is a rather new method with higher requirements to tolerances of machined surfaces, not all techniques of engraving are suitable, there are specific technologies that should be used.

Establishing of the processing modes for glass for reaching of desirable result has some features. The most widespread technique of action in that case is experimental operation of laser machine in all possible modes, using work material, that will be used for production of real products. Disadvantages of that technique are unreasonable using of a large number of work materials with spending service life of laser equipment and time for performing of such operations and making of test programs.

As a result of the performed operations, a proposition of establishing of laser engraving modes are developed for processing of glass products in a broad variation range of material characteristics in case of multiple variants of the choice of possible operating modes combinations. The apparatus of probability theory, mathematical statistics, mathematical modeling and the theory of stochastic functions is applied to solve that problem.

INFORMATION THEORY

Laser operation is based on thermal interaction between light and absorbing medium. The propagation of light in material medium can be divided into four interrelated processes.

1. The reflection of light.
2. The absorption of light depends on its initial intensity, on the thickness of medium that light is passing throw, on the wavelength of the absorbing light and on the coefficient of absorption. If light isn't being absorbed, there is no any interaction between light and material. When photon is being absorbed by a target-molecule, all its energy is being transferred to that molecule and is being spent for a heat and/or for a luminescence.

3. Scattering of light. The phenomenon of scattering is important because it quickly decrease the radiant flux density, impacting on a material. Scattering is decreased with increasing of wavelength, so longer waves of light are ideal way to deliver energy in deep structures of material.

4. Penetration of light. Light penetration depth in deep structures, as well as intensity of scattering, depends on wavelength. Short waves (300–400 nanometers) are intensively scattered and don't penetrate more than 100 microns. But long waves penetrate deeper because that waves are scattered less.

Interaction between laser radiation and material is adequately described by thermal model according to that model the quantity of energy for laser processing significantly depends on optical properties of materials. Key physical parameters of laser, that determine impact of quantum energy to one or the other target, are the generated wavelength, the radiant flux density, the time of impact, the angle of incidence and the quality of a laser beam [3].

Establishing of the laser engraving modes for processing of glass products in practice is performed on the grounds of results of performed experiments; it's low-effective and is accompanied by great costs. The execution of operating modes with simulation model is more progressive.

Relationship between laser engraving modes and optical properties of glass can be described generally by the following expression:

$$R_i\left(Y_i, Y_2, \ldots, Y_i\right) = f\left[R_j\left(Y_i, Y_2, \ldots, Y_j\right)\right],$$

where R – are the parameters of the laser engraving modes; R_i – are the changes of parameters of optical properties of glass; X_1, X_2, …, X_i – are the types of optical properties of glass; Y_1, Y_2, …, Y_j – are the levels of the laser engraving modes; i – is the quantity of optical properties of glass; j – is the quantity of levels of the laser engraving modes, f is the function of the physical parameters of the laser, such as the generated wavelength, the radiant flux density, the time of impact, the angle of incidence, that define interaction between quantum energy and material, and the properties of optical glass such as the microstructure, the chemical composition and the mechanical properties.

Often laser engraving needs to be applied on a finished product when the type of glass of product is unknown. Let's carry out the analysis factors that influence on optical properties. The thickness deviation in a batch of similar products (from 5 % to 30 %), the tendency to surface damages due to a hardness deviation (to 5 %), the emergence of internal tension during the forming operation that leads to the further emergence of microcracks, the high sensitivity to the cluster of tensions influence on the transmission of light. It determines deviations of density, hardness, thermal resistance, thermal conductivity, viscosity, thermal capacity, temperature of a softening, melting point, etc. These properties become a random variable in each case, that's why optical properties of glass become a stochastic function in each specific case of application. Existence of correlation relationships between optical properties of glass and microstructure, chemical composition and mechanical properties of glass can be provided by the expression

$$R_i\left(X_1, X_2, \ldots, X_i\right) = \gamma\left(Z_1, Z_2, \ldots, Z_k\right),$$

where R_i – are the changes of parameters of optical properties of glass; X_1, X_2, …, X_i – are the types of optical properties of glass; i – is the quantity of optical properties of glass; Z_1, Z_2, …, Z_k – are the characteristics of microstructure, chemical composition and mechanical properties of glass; k – is the quantity of the characteristics of microstructure, chemical composition and mechanical properties of glass.

Any stochastic function can be aligned, i.e.to reduce to form when its expected value is equal to zero. Therefore only the aligned elementary stochastic functions will be considered further.

Using the method of canonical representations, stochastic function will be presented as the sum of so-called elementary stochastic functions

$$W(x) = V \cdot \beta(x),$$

where $W(x)$ is the stochastic function, V is the regular random variable, $\beta(x)$ is the regular (non-stochastic) function.

Taking in mind that the deviations of density, hardness, thermal resistance, thermal conductivity, viscosity, thermal capacity, temperature of a softening, flame temperature have normal (or Gaussian) distribution, we'll perform modelling of normal random value on a ground of the central limit theorem:

$$V = \mu + \sigma \cdot \left(\sum_{i=1}^{12} P_i - \sigma \right),$$

where μ – is the average of the normal distribution; σ – is the standard deviation; P – is the random basic number that generated by the random number generator [4].

$\beta(X)$ will be described as regular (non-stochastic) function of coefficient of transmission (transparency, %) in ultra-violet, visible and near-infrared spectral ranges from wavelength of optical radiation.

The developed model is used for establishing of the laser engraving modes of glass with unknown characteristics.

To determine analytical expressions, the method of interpolation and extrapolation and the least-squares method of approximation are applied considering condition:

$$F = \sum_{i=1}^{n} \left(y_i - \beta(x_i) \right)^2 \to \min,$$

where F – is the minimized function; y_i – are the empirical points of statistical dependence; $\beta(x_i)$ – is the analytical functional dependence.

In case of the directed transmission, scattering can be neglected and the radiant flux on the sample is divided into three components: reflected, absorbed and transmitted one. Considering that the reflected flux is about 5–7 % for all types of glass, the transmitted flux can be calculated according to the obtained expressions. The difference between the energy of the incident flux, the energy of the reflected flux and the energy of the transmitted flux allows to calculate the absorbed energy, consumed for heating.

To choose the wavelength of a laser radiation, the function of transparency from wavelength is used. Determination of this functional dependence is performed on a ground of statistical data from the literature. In the Fig. 1 charts 1 and 2 of boundary cases of dependence of transparency on the wavelength of optical radiation of the main brands of glass are submitted.

Based on the conducted researches approximation is selected by polynomial function of the second order.

$$\beta(\lambda) = -194.57\ \lambda^2 + 296.97\ \lambda - 19.961,$$

$$\beta(\lambda) = -127.41\ \lambda^2 + 249.33\ \lambda - 25.76,$$

where $\beta(\lambda_i)$ – is the analytical functional dependence of the coefficient of transmission from the wavelength of optical radiation; λ – is the wavelength of optical radiation.

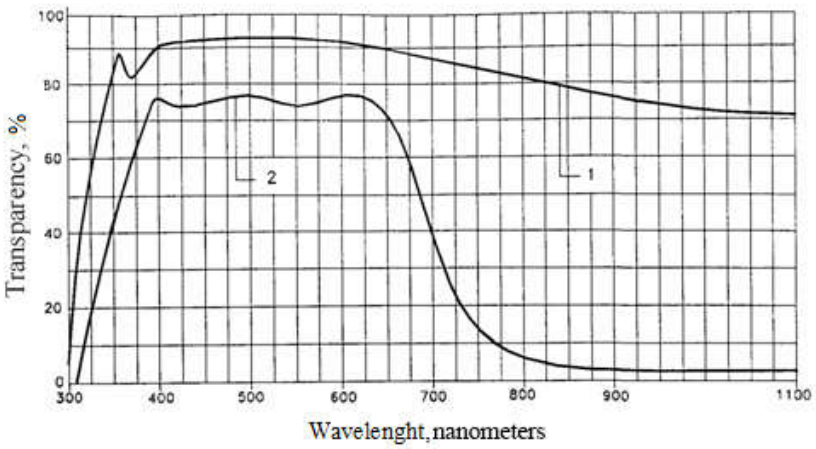

Figure 1. Spectral characteristic of transmission of various glasses:
1 is for a usual windowpane, 2 is for glass with a low-emission coating [5]

Description of an Experiment

The obtained expression describes the boundary values of the changes of light transmission of glass, while changing the wavelength of the laser radiation. The most optimal for the case in question is a CO_2 laser, the emission wavelength of 10.6 μm, controlled by the computer.

For engraving the laser engraver of the Speedy series of Trotec (Austria) with use of Corel Draw, JobControl software product is chosen.

Results and Discussion

Analysis and expert survey showed that to obtain the most clear and high-contrast images to obtain a depth of penetration of laser radiation in an glass of 0.3–0.5 mm. is enough to obtain a stable contour cutting, highly contrasting dark view of paintings and patterns, the necessary adhesion during filling of the image dye.

Given the functional relations between the modes of operation of the laser system, the maximum absorption of light energy glass, optimum performance, set the modes of laser

Given the functional relations between the modes of operation of the laser system, the maximum absorption of light energy of glass, optimum performance, set the modes of laser engraving:

– Laser output power of 11.4 watts.
– Laser engraving speed of 27.0 cm/h.
– Resolution of 500 dpi.
– Pulse frequency 1000 Hz.
– The diameter of the focused laser beam on the material is 0.1 mm.
–The angle of incidence of the laser beam 0°

To check the correctness of application of the developed methodology for setting the modes of interaction of laser radiation with a glass reproduce halftone gray scale [GOST 24930-81. Facsimile equipment gray scale. Technical requirements] from white to black, when changing the laser output power from 2 to 12 W, the laser engraving speed from 10 to 180 cm/sec., resolution from 100 to 1000 dpi., the frequency of pulses from 500 to 1000 Hz, the diameter of the focused laser beam on the material from 0.05 to 1.0 mm. the angle of incidence of the laser beam from 45° to 90°, and combinations of these modes.

CONCLUSIONS

Successful methods of compensation available natural heterogeneities of the material and technological possibilities that provide consistently good results in the case of industrial production of highly exclusive products that help to outline the directions of continued research to improve the quality of the products high quality consumer products.

Methods of successful compensation of the available natural heterogeneities of material and technological capabilities of ensuring steadily good results are found in case of industrial production of highly artistic exclusive products, the directions of continuation of researches are planned.

REFERENCES

1. Emmelmann, C. (1998). *Introduction to industrial laser materials processing.* Hamburg, Germany: Rofin-Sinar.
2. Panchenko, V. Ya. (Ed.) (2001). *Laser materials processing: User's handbook manual.* Plovdiv, Bulgaria.
3. Nishimura, N., Schaffer, C. B., & Kleinfeld, D. (2006). In vivo manipulation of biological system with femtosecond laser pulses. Proceedings of SPIE 6261, High-Power Laser Ablation VI, 62611J. doi:10.1117/12.668886
4. Press, W. H., Teukolsky, S. A., Vetterling, W. T., & Flannery, B. P. (1992). *Numerical recipes in C: The art of scientific computing* (2nd ed.). Cambridge University Press.
5. Shelby, J. E. (2005). *Introduction to Glass Science and Technology* (2nd ed.). Cambridge, UK: The Royal Society of Chemistry.
6. Gamaly, E. G., Rode, A. V., Luther-Davies, B., & Tikhonchuk, V. T. (2002). Ablation of solids by femtosecond lasers: Ablation mechanism and ablation thresholds for metal and dielectrics. *Physics of Plasmas, 9*(3). 949–957. doi:10.1063/1.1447555
7. Momma, C., Chichkov, B. N., Nolte, S., Von Alvesleben, F., Tunnerman, A., & Welling, H. (1996). Short-pulse laser ablation of solid targets. *Optics Communications, 129*(1–2). 134–142. doi:10.1016/0030-4018(96)00250-7
8. Zavestovskaya, I. N. (2012). Laser materials ablation. *32nd European Conference on Laser Interaction with Matter, September 10–14, 2012*, Warsaw, Poland: Institute of Optoelectronics. O-l1.
9. Guillet, J. (1985). *Polymer photophysics and photochemistry*. Cambridge, UK: Cambridge University Press.

Научное электронное издание

«ПРИБОРОСТРОЕНИЕ, ЭЛЕКТРОНИКА И ТЕЛЕКОММУНИКАЦИИ – 2016»

Сборник статей Международного форума

(Ижевск, Россия, 23–25 ноября 2016 года)

Технический редактор *С. В. Звягинцова*
Корректор *Н. К. Швиндт*
Верстка *Н. В. Паклина*
Дизайн обложки *С. А. Мурашов*

Подписано к использованию 26.12.2017. Объем 16,1 МБ. Заказ № 449
Издательство Ижевского государственного технического университета
имени М. Т. Калашникова. 426069, Ижевск, Студенческая, 7

Scientific electronic edition

"INSTRUMENTATION ENGINEERING, ELECTRONICS AND TELECOMMUNICATIONS – 2016"

Proceedings of the International Forum

(Izhevsk, Russia, November 23–25, 2016)

Technical editor *S. V. Zvyagintsova*
Proofreader *N. K. Shvindt*
Layout by *N. V. Paklina*
Cover design by *S. A. Murashov*

Signed to use on December 26, 2017. Size: 16.1 MB. Order No. 449
Publishing House of Kalashnikov Izhevsk State Technical University
Studencheskaya St. 7, 426069 Izhevsk, Russia